PERFORMANCE COMPARISONS OF DOUBLY-FED MACHINES

HAO WU

A thesis submitted in partial fulfilment
of the requirements of the
University of Northumbria at Newcastle
for the degree of
Doctor of Philosophy

Research undertaken in the
School of Computing, Engineering and
Information Sciences

June 2013

Abstract

This research project aims at evaluating a conversion system based on the emerging Brushless Doubly Fed Reluctance Machine (BDFRM) through a comparative experimental study with a traditional and well established slip-ring counterpart, the Doubly Fed Induction Machine (DFIM). One of the main objectives is to establish whether this alternative machine is worthy of industrial consideration in variable speed applications with limited speed ranges (e.g. wind turbines, pump-like drives etc.) in terms of control, reliability, efficiency and power factor performance as major criteria. Such kind of work has not been reported in the open-literature to date and represents the main contribution of the project being undertaken.

A conventional and widely used parameter-independent vector control (VC) scheme has been selected for the operation of both the machines using a shaft-position sensor. The VC algorithm has been simulated and implemented in real-time on state-of-the-art eZdsp development platform based on the TMS320F28335 Digital Signal Controller (DSC). The control code has been derived from a programme written in C++ using the corresponding compiler, the Code Composer Studio (CCS). Comprehensive computer simulations have been done in Matlab/Simulink using the parameters obtained by off-line testing of the DFIM and BDFRM prototypes, which have been built in the same stator frame for comparison purposes. The simulation results have been experimentally verified on two identical test rigs where a commercial 4-quadrant cage induction machine V/f drive has been used as a prime mover or load for either the DFIM or the BDFRM subject to their operating mode.

The preliminary experimental results on two small-scale prototypes have shown that the BDFRM can achieve competitive performance to the similarly rated DFIM and as such should warrant further investigation and increasing interests of both academic and industrial communities as a potential large-scale wind generator or a pump drive.

Acknowledgements

First of all, I am grateful to my parents and my wife for their patience, understanding and encouragement.

I would like to express my sincere gratitude to my supervisor Dr. Milutin Jovanovic for his guidance, invaluable support, excellent cooperation and extensive knowledge in electrical drives area which have allowed the project to be completed on time.

Furthermore, special acknowledgements are due to the former School of Computing, Engineering and Information Sciences for providing such a stimulating and pleasant research environment, and for offering financial support for the DFIG test rig.

Last but definitely not least, I wish to extend my thankfulness to all those who helped me at Northumbria University or elsewhere during the entire PhD period.

Declaration

I declare that the work contained in this thesis has not been submitted for any other award and that it is all my own work. I also confirm that this work fully acknowledges options, ideas and contributions from the work of others.

Any ethical clearance for the research presented in this thesis has been approved. Approval has been sought and granted by the School Ethics Sub-Committee, School of Computing, Engineering and Information Sciences on 1/5/2010.

Name: HAO WU

Signature:

Date:

Contents

Abbreviations

Machine Parameters and Variables

i_{gd}, i_{gq}	Grid side direct and quadrature current components [A]
$\mathbf{i_l}$	Line side current vector [A]
i_{ld}^*, i_{lq}^*	Reference values of line side direct and quadrature current components [A]
i_{ld}, i_{lq}	Line side direct and quadrature current components [A]
I_p, I_r	Primary (BDFRM) side and rotor (DFIM) side current [A]
$\mathbf{i_p}$, $\mathbf{i_r}$	Primary (BDFRM) side and rotor (DFIM) side current vectors [A]
i_{pd}, i_{pq}	Primary side direct and quadrature current components [A]
i_{rd}, i_{rq}	Rotor side direct and quadrature current components [A]
$\mathbf{i_r'}$, $\mathbf{i_s'}$	Rotor (DFIM) side and secondary (BDFRM) side current vectors referring to stator side and primary side respectively [A]
I_s	Stator (DFIM) side or secondary (BDFRM) side current [A]
$\mathbf{i_s}$	Stator (DFIM) side or secondary (BDFRM) side current vector [A]
i_{sd}, i_{sq}	Stator (DFIM) side or secondary (BDFRM) side direct and quadrature current components [A]
i_{sd}^*, i_{sq}^*	Referenced values of secondary side direct and quadrature current components [A]
k_p, k_i	Proportional and integral gains of certain PI controller
L_{lp}, L_{lr}	Primary (BDFRM) side and rotor (DFIM) side leakage inductance [H]
L_{ls}	Stator (DFIM) side or secondary (BDFRM) side leakage inductance [H]
L_{lr}'	Rotor (DFIM) side leakage inductance referred to stator side [H]

L_m	Magnetizing inductance [H]
$L_p,\ L_r$	Primary (BDFRM) side and rotor (DFIM) side self-inductance [H]
$L_{ps},\ L_{sp}$	Mutual inductance in the BDFRM [H]
L_s	Stator (DFIM) side or secondary (BDFRM) side self-inductance [H]
$N_r,\ N_s$	Turns of rotor and stator winding
N	Turns Ratio
$P_g,\ Q_g$	Grid side active and reactive power [W]
$P_p,\ P_s$	Primary (BDFRM) side and stator (DFIM) side active power [W]
$P_p^*,\ Q_p^*$	Referenced values of primary side active and reactive power [W]
p_p	Pole pairs in the DFIM
p_r	Rotor poles in the BDFRM
P_{rotor}	Active power on rotor winding [W]
P_{stator}	Active power on stator winding [W]
P_{grid}	Active power on grid side [W]
P_{mech}	Mechanical power [W]
$Q_p,\ Q_s$	Primary (BDFRM) side and stator (DFIM) side reactive power (VAr)
$R_p,\ R_r$	Primary (BDFRM) side and rotor (DFIM) side resistance [Ω]
R_s	Stator (DFIM) side or secondary (BDFRM) side resistance [Ω]
R_r'	Rotor side resistance referred to stator side [Ω]
s	Degree of slip
$S_g,\ S_p$	Grid side and primary side apparent power [VA]
T_e	Electromagnetic torque [Nm]
$U_{dc},\ U_{dc}^*$	Real and referenced value of DC link voltage [V]
$\mathbf{u_p}$	Primary side voltage vector [V]
$\mathbf{v_c}$	GSC grid side phase voltage vector [V]

v_{cd}^{*}, v_{cq}^{*}	Referenced values of GSC grid side direct and quadrature voltage components [V]
V_p, V_r	Primary (BDFRM) side and rotor (DFIM) side phase voltage [V]
$\mathbf{v_p}$, $\mathbf{v_r}$	Primary (BDFRM) side and rotor (DFIM) side phase voltage vectors [V]
v_{pd}, v_{pq}	Primary side direct and quadrature voltage components [V]
v_{rd}, v_{rq}	Rotor side direct and quadrature voltage components [V]
V_{p0}, V_{p0l}	Primary side open circuit phase and line voltage [V]
V_{pl}, V_{sl}	Primary side and secondary side line voltage [V]
V_s	Stator (DFIM) side or secondary (BDFRM) side supply voltage [V]
$\mathbf{v_s}$	Stator (DFIM) side or secondary (BDFRM) side voltage vector [V]
v_{sd}, v_{sq}	Stator (DFIM) side or secondary (BDFRM) side direct and quadrature voltage components [V]
v_{sd}^{*}, v_{sq}^{*}	Referenced values of secondary side direct and quadrature voltage components [V]
V_{s0}, V_{s0l}	Secondary side open circuit phase and line voltage [V]
X_{lr}, X_{ls}	Stator side and rotor side leakage reactance [Ω]
X'_{lr}	Rotor side leakage reactance referred to stator side [Ω]
X_m	Magnetizing reactance [Ω]
Z_s	Stator winding impedance [Ω]
Z_{total}	Total impedance of stator and rotor windings [Ω]
$\theta_{r,p,s}$	Angular positions of the rotating reference frames [rad]
$\mathbf{\Psi_m}$	Magnetizing flux linkage vector [Wb]
$\mathbf{\Psi_p}$, $\mathbf{\Psi_r}$	Primary (BDFRM) side and rotor (DFIM) side flux linkage vectors [Wb]
Ψ_p	Primary side flux linkage magnitude [Wb]
Ψ_{pd}, Ψ_{pq}	Primary side direct and quadrature flux components [Wb]

$\boldsymbol{\Psi_{ps}}$	Mutual flux linkage vector in the BDFRM [Wb]
Ψ_{ps}	Mutual flux linkage magnitude in the BDFRM [Wb]
$\Psi_{rd},\ \Psi_{rq}$	Rotor side direct and quadrature flux components [Wb]
$\boldsymbol{\Psi_s}$	Stator (DFIM) side or secondary (BDFRM) side flux linkage vectors [Wb]
Ψ_s	Stator side flux linkage magnitude [Wb]
$\Psi_{sd},\ \Psi_{sq}$	Stator (DFIM) side or secondary (BDFRM) side direct and quadrature flux components [Wb]
$\omega_p,\ \omega_r$	Primary and rotor electrical angular velocity [rad/s]
ω_{rm}	Rotor mechanical angular velocity [rad/s]
ω_s	Stator or secondary electrical angular velocity [rad/s]

Acronyms

BDFRG	Brushless Doubly Fed Reluctance Generator
BDFRM	Brushless Doubly Fed Reluctance Machine
CCS	Code Composer Studio
DAC	Digital to Analogue Converter
DFIG	Doubly Fed Induction Generator
DFIM	Doubly Fed Induction Machine
DFM	Doubly Fed Machine
DPC	Direct Power Control
DSC	Digital Signal Controller
DTC	Direct Torque Control
EMI	Electro-Magnetic Interference
FRT	Fault Ride Through
GSC	Grid Side Converter
IGBT	Insulated Gate Bipolar Transistor

IM	Induction Machine
LPF	Low Pass Filter
MPPT	Maximum Power Point Tracking
MRAS	Model Reference Adaptive System
MSC	Machine Side Converter
PCB	Printed Circuit Board
PLL	Phase Locked Loop
PMSG	Permanent Magnet Synchronous Generator
PWM	Pulse Width Modulation
SCIM	Squirrel Cage Induction Machine
SVM	Space Vector Modulation
VCO	Voltage Controlled Oscillator
VSCF	Variable Speed Constant Frequency
WECS	Wind Energy Conversion Systems
WRIG	Wound Rotor Induction Generator

1. Introduction

In July 2011, the Department of Energy and Climate Change (DECC) published 'The 2020 UK Renewable Energy Roadmap' about the UK commitment to fulfil its obligation to the European Union of producing 15% of its energy demands from renewable sources by 2020. Some notable changes have been made in terms of the wind energy deployment scenarios following the Renewable Energy Strategy of 2009 and the 2010 update. The current target for offshore wind has been set to increase from the predicted 13 GW in 2009 to 18 GW by 2020. The current central scenario for onshore wind, however, has been reduced from 15 GW to 13 GW by 2020 [1].

It is obvious that offshore wind turbines are becoming a driving force within the wind energy generation nowadays. But when employing the conventional Doubly-Fed Induction Generator (DFIG) it appears that its shortcomings in onshore wind farms have been further amplified in offshore applications (for instance, a short maintenance cycle for brushes and/or slip-rings, control and reliability issues, higher operation and maintenance costs, inferior low-voltage-fault-ride-through capabilities etc.). For this reason, alternative generator topologies have been proposed to overcome the DFIG limitations, including the well-established solutions like a classical wound rotor or Permanent Magnet Synchronous Generator (PMSG), or novel emerging brushless technologies such as, the Brushless Doubly-Fed Reluctance Generator (BDFRG) or its closely related counterpart, the Brushless Doubly-Fed Induction Generator (BDFIG).

This thesis is primarily concerned with assessing an energy conversion system based on the Brushless Doubly-Fed Reluctance Machine (BDFRM) through a comparative performance study with a conventional and widely-used counterpart, the Doubly-Fed Induction Machine (DFIM). Vector control approach has been adopted to achieve variable speed operation of both the machines for comparison purposes.

1.1 Motivation

The main motivations for making performance comparisons of the DFIM and the BDFRM could be summarised as follows.

(1) The BDFRM is more reliable than the DFIM as there is no brush gear on the cage-less reluctance rotor.
(2) The BDFRM retains all of the cost benefits of the DFIM associated with using a partially-rated power electronics, and especially in applications with limited variable speed ranges (such as wind turbines) where the converter rating, size and cost can be further reduced.
(3) The BDFRM has inherent rotor saliency and as such is more amenable to sensorless operation than the DFIM. The absence of a shaft encoder would decrease the cost and increase the robustness of the system [2].
(4) The BDFRM may operate as a fixed/adjustable speed synchronous machine which should make it more efficient than the DFIM in low speed applications [3]. Thus, it could deliver more power at higher torque for the same losses this being an advantage over the DFIM in small drives.
(5) Similarly to its induction rotor relative, the BDFIM, the BDFRM should offer superior fault-ride-through performance to the DFIM owing to the higher leakage reactance and lower transient currents [4-9].

1.2 Aim and Objectives

The proposed research aims at developing a vector control solution for a commercial variable speed doubly-fed induction machine technology (DFIM), and an emerging brushless design alternative (BDFRM), as well as making their performance comparison under the same (normal) operating conditions. Such a generic approach is possible due to modelling and control similarities of the two closely related machines

despite their fundamentally different operating principles. The work will be based on simulation studies using Matlab/Simulink, followed by the experimental verification on DFIM/BDFRM test rigs available in the power laboratory. The theoretical part of the DFIM research will focus on a most widely used system for computer studies.

The above aim has been divided into the following manageable objectives/tasks:

(1) Perform a comprehensive literature review on the subject to identify the most appropriate controller designs for the considered target application and performance comparisons.

(2) Develop simulation models for speed control of grid connected DFIM and BDFRM in Matlab/Simulink, and investigate their performance under normal operating conditions of the machines using parameters of the existing prototypes.

(3) Set up the DFIM and the BDFRM test rigs having identical commercial 4-quadrant V/f induction machine drives for load/prime mover emulation, and TMS320F28335 DSP development platform for DFIM/BDFRM control implementation in real-time.

(4) Develop (in C language) control codes for either machine on the dedicated test rigs; operate the rigs to examine the controller response to desired variations of rotating speed and/or rotor/secondary side current levels (e.g. torque/power control) as well as to generate the necessary experimental results for machine performance comparison.

(5) Compare the vector control capabilities of the test machines from the results obtained in generating mode using both the controllable machine side converter (MSC) and the grid side converter (GSC) i.e. for bi-directional power flow.

(6) Operate the DFIM and the BDFRM as motors to check the speed control performance and then make a comparative analysis.

1.3 Contributions

The main contributions of this thesis are:

(1) The development and evaluation of computer based simulation programmes for the DFIM and the BDFRM using a vector control algorithm and the measured machines parameters obtained by off-line testing.
(2) The real-time implementation of the developed control algorithms on the DFIM and BDFRM replica test rigs using the same eZdsp TMS320F28335 DSP development platform and the same power electronics hardware.
(3) The experimental verification and performance comparison of the two machines under different operating conditions.

1.4 Thesis Outline

The remainder of the thesis is organised as follows,

Chapter 2 gives a critical review of the key papers published on the DFIM and BDFRM. A particular attention is being paid to the work concerned with control and performance analysis.

Chapter 3 presents the equivalent circuit and dynamic modelling aspects of the DFIM and the BDFRM, and considers various control methods, such as, scalar control, vector control (VC), direct torque control (DTC) and direct power control (DPC) which have been applied to the BDFRM in particular.

Chapter 4 describes in detail the vector control strategies for the DFIM and the BDFRM.

Chapter 5 shows the computer simulation results of the DFIM and the BDFRM operation with VC.

Chapter 6 develops the experimental digital controller for the DFIM and the BDFRM test rigs. Experimental results of dynamic response of the VC algorithm, power output and power factor analysis for different rotor/secondary side current set points and speed control performance are shown and compared for the both machines.

Chapter 7 is a summary of the relevant conclusions and possible extensions that can be drawn from the work presented in this thesis.

Appendices A and B show details on the DFIM and BDFRM test rigs, respectively, with parameter testing results.

Appendix C demonstrates some main codes written in CCS for experimental usage.

2. Literature Review

2.1 Introduction

Control aspects of both of the DFIM and the BDFRM are critically reviewed in this chapter before making a comparative study.

First of all, the DFIM will be briefly introduced followed by the review of the corresponding control methods including pitch control (for wind turbines), vector and field oriented control, active and reactive power control, DTC, DPC, sliding mode control and sensorless control.

Secondly, after a short introduction of the BDFRM, a revision of the associated control strategies will be made. The control approaches reported in the literature for this machine will be addressed, such as scalar control, vector control, DTC and DPC.

2.2 DFIM Control Methods

The aim of grid-connected wind energy conversion systems (WECS) is to generate output voltage of constant frequency from a variable speed operation of the drive shaft. Thus, the wind turbine generator should work under variable speed constant frequency (VSCF) conditions. The DFIG could supply power at constant voltage and frequency while the rotational speed varies [10-12]. This allows the maximum power point tracking (MPPT), higher turbine efficiency, smooth operation at unity power factor and superior power quality of DFIG or any other variable speed WECS. Similar performance advantages cannot be achieved with fixed-speed WECS based on cage induction generators.

The DFIG is a wound rotor induction generator (WRIG) with the rotor windings connected to the supply grid through a back-to-back partially rated (20% - 30% of the DFIG's rating) [13-16] power converter. The stator windings are connected to the same grid through a step-up transformer as shown in Fig. 2.1.

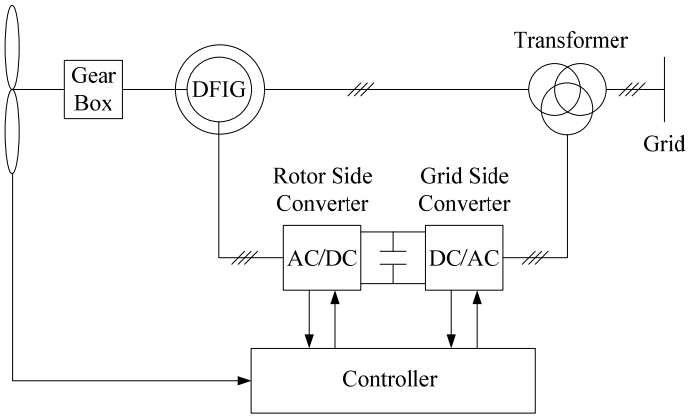

Figure 2.1: DFIG Wind Turbine System

The back-to-back converter allows a bi-directional power flow and consists of two conventional pulse-width-modulated (PWM) voltage source converters with a common DC link. The size of the power converters depends on both the DFIG's rating and the desired speed range [17, 18]. Such converters have been widely used and discussed in [10, 19, 20]. The DFIG could operate as a generator or a motor in both sub-synchronous mode (0<slip<1) and super-synchronous (slip<0) mode due to the bi-directional power flow ability of the power converters. Ignoring losses, the rotor, stator and mechanical power can be represented in terms of slip (s) as [11, 21]:

$$P_{rotor} = -sP_{stator} \tag{2.1}$$

$$P_{stator} = \frac{P_{grid}}{1-s} \tag{2.2}$$

$$P_{mech} = P_{rotor} + P_{stator} = -P_{rotor}\frac{(1-s)}{s} \tag{2.3}$$

The above well-known relationships imply that the bigger the slip, the larger electrical power is being absorbed or generated through the rotor. The operating modes and power signs of the DFIM using generator convention are given in Table 2.1. [11].

Table 2.1: Operational Speed Modes and Power Signs of the DFIM [11]

Slip	Operating Mode	P_{mech}	P_{stator}	P_{rotor}
0<s<1 (sub-synchronous)	Motor	<0	<0	>0
	Generator	>0	>0	<0
s<0 (super-synchronous)	Motor	<0	<0	<0
	Generator	>0	>0	>0

Therefore, the DFIG has the following advantages over other types of generators used in wind energy conversion systems [22, 23]:

(1) The power electronics converters and associated hardware are typically rated at only 0.25 p.u. while the speed range is around $\pm$33% of the synchronous speed. This means that their cost is much less than with the synchronous generator.

(2) Power factor control could be implemented at lower cost. The DFIG with a 4-quadrant converter on the rotor side enables inherently decoupled control of active and reactive power.

The use of the DFIG not only improves the efficiency of energy conversion of a wind turbine but also provides a significant network support with respect to voltage control, transient performance and/or damping capability [24, 25]. This makes the DFIG very popular and an attractive choice for variable speed WECS. For this reason, various DFIG control systems have been reported in the literature for this and similar applications [13, 15, 26-36].

2.2.1 Pitch Control

Pitch control methods allow control of mechanical power by altering the blade angle (i.e. blade twisting) of a wind turbine. The mechanical power output of the wind turbine in steady state is given by the well-known empirical relationship [37]:

$$P_{mech} = \frac{1}{2}\rho\pi R^2 u^3 C_p(\theta, \lambda) \qquad (2.4)$$

where ρ is the air density (kg/m^3), R is the blade radius (m), u is the upstream wind speed (m/s) and $C_p(\theta,\lambda)$ is the aerodynamic (power) coefficient (i.e. the turbine efficiency), which depends on the pitch angle (θ) and the tip speed ratio ($\lambda = R\omega/u$). The aim of the wind turbine at lower wind speeds (i.e. in the base speed region) is to adjust the rotor angular velocity (ω) so that $C_p(\theta,\lambda)$ is maintained at its peak value to achieve the maximum wind power extraction and the highest efficiency of wind energy conversion [24, 38, 39]. For wind speeds beyond the rated point up to the cut-out speed, efficiency must be sacrificed by reducing C_p to prevent the generator overloading. In this higher speed region, power is controlled at its rated value through θ variations. At gusty winds, the turbine should be cut-out (locked) to avoid structural damages. A typical pitch control scheme is shown in Fig. 2.2,

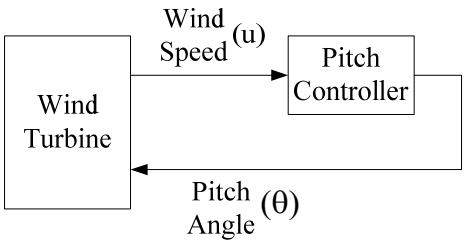

Figure 2.2: Typical Pitch Control Scheme

2.2.2 Vector Control

As opposed to scalar control [40, 41], which requires steady-state model equations of the machine to predict the magnitude and frequency (angular speed) of voltage, current and/or flux linkage space vectors for control purposes, vector control (VC) uses relationships valid for dynamic states i.e. instantaneous values of these quantities usually in a d-q synchronously rotating reference frame [42]. In the DFIG case, VC of the active (*P*) and reactive (*Q*) power is inherently decoupled if the flux-producing (*d*) axis is aligned with the stator flux vector. This approach is known as the field-oriented control (FOC) in the literature. In classical VC algorithms, however,

where the torque-producing (q) axis is usually aligned with the stator voltage vector and where, unlike the FOC scenario, the flux magnitude/angle estimation is therefore not needed, there are coupling effects largely caused by the back-emf components in the respective axes. This VC limitation means that special decoupling terms need to be introduced as compensation to achieve the same FOC performance in this sense. Research work carried out in [10, 19, 43-45] have shown the suitability of such VC or FOC schemes for both the grid and stand-alone DFIG applications.

Another advantage of vector control (VC) based DFIG is its oscillation damping capability. In [46], decoupled VC algorithms have been developed to effectively damp inter-area oscillations in a power system. Further DFIG related control work of practical interest is the sensitivity analysis of noise effects to accuracy of PLLs and incremental position encoders being carried out in [47]. Also, a direct current VC method has been proposed for Q and grid voltage control in [48, 49]. Finally, a different approach has been presented in [50], in which the vector controlled DFIG has been used for speed regulation of centrifugal loads in a high-speed region.

2.2.3 Active and Reactive Power (PQ) Control

PQ control of the DFIG has been discussed widely in [14, 51-53]. Although active power (P) is usually considered to be more important from a consumer point of view, reactive power (Q) is equally responsible for proper operation of an electrical system [54]. The DFIG requires Q for magnetisation and/or power factor improvement. In grid-connected applications, the DFIG could absorb Q from the grid. However, in isolated stand-alone systems or in weak networks, Q should be supplied by an external source such as a 3-phase capacitor bank (which has been traditionally used for this purpose [55]), an over-excited diesel synchronous generator or any other Q compensator based on power electronics devices (e.g. FACTS). In recent work [56-61], various Q control strategies have been considered.

2.2.4 Direct Torque Control (DTC)

The main principle of DTC is to control the rotor flux linkage magnitude and generator torque directly by proper selection of the inverter switching states [42, 62-65]. The flux and torque errors within the pre-set hysteresis bands are restricted by the switching patterns. Torque and flux feedbacks are required for this type of control. The rotor flux is calculated from the rotor side and stator side current vectors, while the final torque is estimated using the calculated rotor flux and the measured rotor side current. Recent research on DFIGs with DTC has mainly focused on the grid-connected applications and unbalanced fault ride through (FRT) issues [66, 67].

2.2.5 Direct Power Control (DPC)

DPC is a method for fast power control of a grid-connected DFIG fed by a conventional back-to-back voltage source converter on the rotor side. Measurements of active and reactive power on the grid side are essential to track desired reference signals using hysteresis controllers. This kind of control eliminates the need for rotor position sensing and gives excellent dynamic performance. Thus, this is an attractive sensor-less control algorithm for variable speed drive and generator systems [13, 68-74]. Similar to DTC, DPC applied on the DFIG with imbalanced network or FRT solutions is a trendy topic these days and has been thoroughly investigated in [75-78].

2.2.6 Sensorless Control

Sensor-less control implies the absence of a shaft position encoder which makes its clearly distinctive and more complex (as the speed and/or position have to be estimated from voltage/current measurements) compared to sensor-based control [79]. The most popular sensor-less algorithms, DTC and DPC, have been looked at in the

previous sections, so other sensor-less methods reported in the literature will be reviewed here.

A model reference adaptive system (MRAS) observer is commonly used in sensor-less methods where the rotor position and speed estimates have been derived from the measured rotor currents. It has been initially proposed for DFIG in [80-82], and further developed for this particular machine in [83-86]. In the meantime, other sensor-less schemes have also been researched based on rotor phase-lock-loop (PLL) [87, 88], reduced order speed adaptive observers [89], air-gap power factor [90], high frequency signal injection [91] or rotor position computation techniques [92]. A typical MRAS observer is shown in Fig. 2.3, where v_s and i_s are stator voltage and stator current respectively, i_r is rotor current and ω_r^* is the referenced rotating speed.

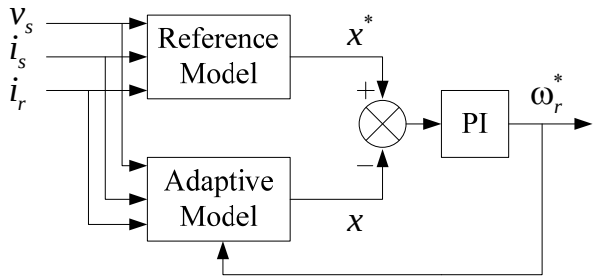

Figure 2.3: Typical MRAS Observer

2.3 Control of BDFRM

Although the inverter-fed BDFRM has not been used in industry yet, it is still an attractive choice as a possible alternative to DFIM in variable speed applications with limited speed ranges due to high reliability of brushless structure, maintenance-free operation and low cost of a partially-rated power electronic converter. The BDFRM possesses all the advantages of doubly fed machines (DFM) over singly-fed cousins in terms of the flexibility of the operation mode, the wider speed range and the greater control freedom, as the BDFRM (similar to DFIM) could operate at sub-synchronous

and super-synchronous speeds in both motoring and generating modes [93]. As with the DFIM, the main economic benefits of potentially using this machine come from its slip power recovery property that allows the use of a smaller (relative to the machine rating) back-to-back converter, and especially if the operating speed range required is relatively narrow (for example, with wind turbines or pump-like drives) when the converter size and cost could be further reduced [94-97].

The BDFRM has two standard, sinusoidally distributed stator windings of different applied frequencies and pole numbers as illustrated in Fig. 2.4. In order to provide rotor position dependant magnetic coupling between the windings and torque production from the machine [98, 99], the cage-less reluctance rotor should have half the total number of stator poles. Such an unconventional design and unusual operating principle [100] make it bigger, and thus more expensive, compared to an equivalent synchronous reluctance or a cage induction machine in the torque producing aspect [93, 101, 102].

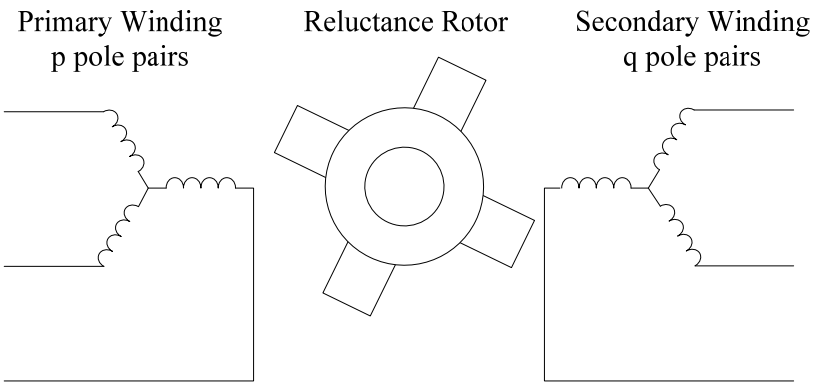

Figure 2.4: A Structural Diagram of the BDFRM

The BDFRM could operate as a conventional IM or as a fixed/adjustable speed synchronous machine [103] for high speed field weakening applications [104]. From a control point of view, the BDFRM allows not only control of torque but also the power factor (a larger inverter would be required in this case) [96, 105-108] or efficiency [95].

When compared to machines of similar properties, the BDFRM is superior in many respects. The absence of brushes and slip rings is an obvious advantage over the conventional DFIM in applications with high reliability and low operation and maintenance (O&M) cost requirements (e.g. offshore wind farms in particular). The BDFRM has higher efficiency [109], more robust rotor construction and easier control than the closely related brushless doubly fed induction machine (BDFIM) having the same stator configuration as the BDFRM but a special squirrel caged rotor of nested structure [4-9]. If optimally designed (with a higher rotor saliency ratio as modern synchronous reluctance machines), the overall performance of the BDFRM can be improved to a level competitive with the IM of similar rating [93, 110].

Since all the control algorithms have been briefly introduced in the DFIM's section, a survey of the main control methodologies reported in the BDFRM literature will be presented.

Both scalar control and DTC algorithms have already been proposed in [111] and evaluated by simulations [95, 112] and experimentally [113, 114]. Scalar control has been further improved and optimised in [115]. A vector control scheme has been simulated in [94] and then successfully practically implemented for both motoring and generating modes in [116]. However, all these control approaches are sensor based and as such rely on using encoder measurements for either rotor position and/or speed detection. Thus, by eliminating the encoder, sensor-less vector or direct torque control would not only reduce the system cost but, more importantly, would improve its reliability [117, 118]. Further performance improvement can be achieved by applying sliding mode observer in a DTC scheme as demonstrated in [119, 120]. DPC has been applied to the DFIM over the last decade [69], but is still a relatively new control topic in the BDFRM case. It has been only recently evaluated by simulations [121, 122] and experiments [123-125] for decoupled control of torque/real power and reactive power.

2.4 Conclusions

The above literature review on both the traditional DFIM and the emerging BDFRM technologies clearly shows that there is continuous interest in the academic and industrial communities in machine types. Although the machines have clear design and operational differences, they interestingly have dynamic modelling and control similarities, which facilitates their performance comparison as will be shown in the remainder of this thesis. All of the commonly used control algorithms, such as scalar control, vector control, DTC and DPC, which have only been outlined above, will be described and discussed in more detail in the following chapters.

3. Control Methods

3.1 Introduction

Since all of the four commonly used control algorithms e.g. scalar control, vector control, DTC and DPC, have been only briefly reviewed above, they will be further discussed in detail in this chapter. Then an appropriate control method will be chosen for simulation studies and practical implementation to allow performance comparisons of the experimental machines. Firstly, the equivalent circuit and dynamic modelling aspects of the DFIM and the BDFRM will be presented followed by the control methods analysis. The following usual modelling assumptions will be made:

(1) The iron of the machine is infinitely permeable (i.e. iron losses will be neglected).
(2) The machine windings have sinusoidal space distribution.
(3) The magnetic saturation effects have been ignored.

When comparing the dynamic models between these two machines, it turns out that they are quite similar (the primary winding and the secondary winding of the BDFRM are analogous to the stator winding and the rotor winding of the DFIM, respectively) although the respective parameters are rather different in values (e.g. the BDFRM should have much higher leakage reactances) due to the conceptually distinct operating principles of the machines. Thus, the model-based control algorithms will be structurally similar for both machines and only those specifically related to the BDFRM will be consequently considered in the remainder of this chapter.

It is important to note that the equations of a 3-phase AC machine are normally represented in direct and quadrature (d-q) axis form in order to develop high order models for particular applications. Also, such a transformation into 2-phase components in a rotating reference frame increases the controllability of the machine

as the control variables appear as DC quantities which are easier to control than the AC counterparts.

3.2 Equivalent Circuit and Dynamic Modelling

3.2.1 Doubly-Fed Induction Machine (DFIM)

The dynamic equations of the DFIM using standard notation for motoring convention in arbitrary reference frame can be written as:

$$\mathbf{v_s} = R_s\mathbf{i_s} + \frac{d\mathbf{\Psi_s}}{dt} + j\omega\mathbf{\Psi_s} \tag{3.1}$$

$$\mathbf{v_r} = R_r\mathbf{i_r} + \frac{d\mathbf{\Psi_r}}{dt} + j(\omega - \omega_r)\mathbf{\Psi_r} \tag{3.2}$$

where the flux linkages and 3-phase self-inductances are given by expressions:

$$\mathbf{\Psi_s} = L_s\mathbf{i_s} + L_m\mathbf{i_r} \tag{3.3}$$

$$\mathbf{\Psi_r} = L_r\mathbf{i_r} + L_m\mathbf{i_s} \tag{3.4}$$

$$L_s = L_{ls} + L_m \tag{3.5}$$

$$L_r = L_{lr} + L_m \tag{3.6}$$

Resolving (3.1) and (3.2) into the respective d-q components in steady state, one gets:

$$v_{sd} = R_s i_{sd} - \omega\Psi_{sq} \tag{3.7}$$

$$v_{sq} = R_s i_{sq} + \omega\Psi_{sd} \tag{3.8}$$

$$v_{rd} = R_r i_{rd} - (\omega - \omega_r)\Psi_{rq} \tag{3.9}$$

$$v_{rq} = R_r i_{rq} + (\omega - \omega_r)\Psi_{rd} \tag{3.10}$$

where

$$\Psi_{sd} = L_s i_{sd} + L_m i_{rd} \tag{3.11}$$

$$\Psi_{sq} = L_s i_{sq} + L_m i_{rq} \tag{3.12}$$

$$\Psi_{rd} = L_r i_{rd} + L_m i_{sd} \tag{3.13}$$

$$\Psi_{rq} = L_r i_{rq} + L_m i_{sq} \tag{3.14}$$

The subscripts 's' and 'r' in the above equations denote the stator and rotor winding quantities respectively, '*' represents the complex conjugate, and L_{ls}, L_{lr} and L_m are the stator leakage inductance, rotor leakage inductance and magnetising inductance respectively.

A generic variable **F** inside the DFIM with space vector form in different reference frames: stator (d_sq_s), stationary ($\alpha\beta$), or rotor (d_rq_r) shown in Fig. 3.1, can be represented by the following well-known frame conversion relationships:

$$\mathbf{F}_{d_sq_s} = \mathbf{F}_{\alpha\beta} * e^{-j\theta_s} \tag{3.15}$$

$$\mathbf{F}_{\alpha\beta} = \mathbf{F}_{d_rq_r} * e^{j\theta_r} \tag{3.16}$$

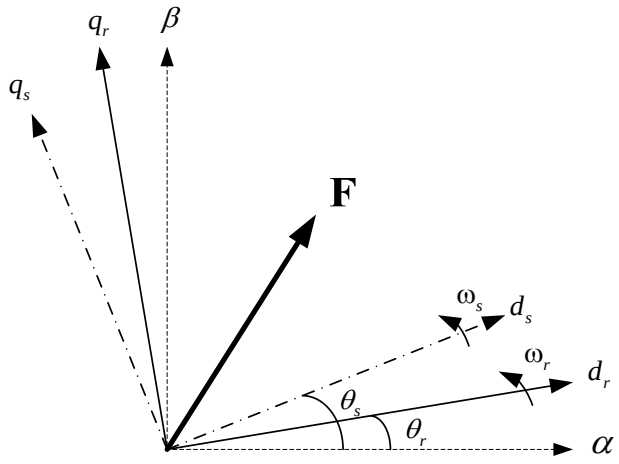

Figure 3.1: Phasor Diagram of the DFIM

When ignoring the power loss on stator resistance, and resolving (3.1) and (3.3) to get $\mathbf{v_s}$ and $\mathbf{i_s}$, the stator active and reactive power in steady state can be calculated as follows in stator flux orientation frame:

$$\begin{aligned} P_s + jQ_s &= \frac{3}{2}\mathbf{v_s} * \mathbf{i_s^*} \\ &\approx \frac{3}{2} j\omega_s \Psi_s * \frac{1}{L_s}(\Psi_s - L_m \mathbf{i_r}) \\ &= \frac{3}{2}\omega_s(j\Psi_s) * \frac{1}{L_s}\left[(\Psi_s - L_m i_{rd}) - jL_m i_{rq}\right] \\ &= \frac{3\omega_s}{2L_s}[\Psi_s L_m i_{rq} + j\Psi_s(\Psi_s - L_m i_{rd})] \end{aligned} \tag{3.17}$$

So,

$$P_s = \frac{3\omega_s}{2L_s}\Psi_s L_m i_{rq} \tag{3.18}$$

$$Q_s = \frac{3\omega_s}{2L_s}\Psi_s(\Psi_s - L_m i_{rd}) \tag{3.19}$$

3.2.2 Brushless Doubly-Fed Reluctance Machine (BDFRM)

The dynamic equations of the BDFRM using standard notation for motoring convention in arbitrary reference frame can be expressed as:

$$\mathbf{v_p} = R_p\mathbf{i_p} + \frac{d\mathbf{\Psi_p}}{dt} + j\omega\mathbf{\Psi_p} \tag{3.20}$$

$$\mathbf{v_s} = R_s\mathbf{i_s} + \frac{d\mathbf{\Psi_s}}{dt} + j(\omega_r - \omega)\mathbf{\Psi_s} \tag{3.21}$$

where the relationships for the flux linkages are given by:

$$\mathbf{\Psi_p} = L_p\mathbf{i_p} + L_m\mathbf{i_s^*} \tag{3.22}$$

$$\mathbf{\Psi_s} = L_s\mathbf{i_s} + L_m\mathbf{i_p^*} \tag{3.23}$$

$$L_p = L_{lp} + L_m \tag{3.24}$$

$$L_s = L_{ls} + L_m \tag{3.25}$$

The d-q form of (4.20) and (4.21) in steady-state becomes:

$$v_{pd} = R_p i_{pd} - \omega\Psi_{pq} \tag{3.26}$$

$$v_{pq} = R_p i_{pq} + \omega\Psi_{pd} \tag{3.27}$$

$$v_{sd} = R_s i_{sd} - (\omega_r - \omega)\Psi_{sq} \tag{3.28}$$

$$v_{sq} = R_s i_{sq} + (\omega_r - \omega)\Psi_{sd} \tag{3.29}$$

with

$$\Psi_{pd} = L_p i_{pd} + L_m i_{sd} \tag{3.30}$$

$$\Psi_{pq} = L_p i_{pq} - L_m i_{sq} \tag{3.31}$$

$$\Psi_{sd} = L_s i_{sd} + L_m i_{pd} \tag{3.32}$$

$$\Psi_{sq} = L_s i_{sq} - L_m i_{pq} \tag{3.33}$$

The subscripts 'p' and 's' denote the primary and secondary winding quantities respectively, '*' represents the complex conjugate, and L_{lp}, L_{ls} and L_m are primary leakage inductance, secondary leakage inductance and magnetising inductance respectively.

A random variable **F** and typical reference frames e.g. primary ($d_p q_p$), stationary ($\alpha\beta$), secondary ($d_s q_s$), are shown in Fig. 3.2. Similarly to the DFIM case, the reference frame transformations are given by:

$$\mathbf{F}_{d_p q_p} = \mathbf{F}_{\alpha\beta} * e^{-j\theta_p} \tag{3.34}$$

$$\mathbf{F}_{\alpha\beta} = \mathbf{F}_{d_s q_s} * e^{j\theta_s} \tag{3.35}$$

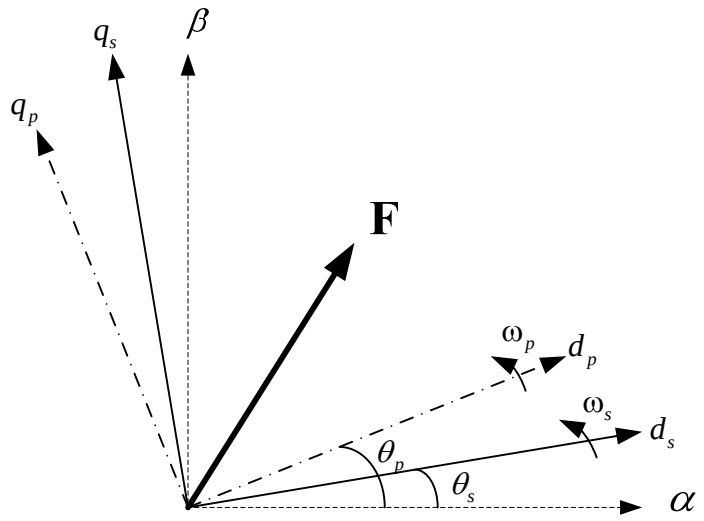

Figure 3.2: Phasor Diagram of the BDFRM

When ignoring the power loss on primary resistance, and resolving (3.20) and (3.22) to get $\mathbf{v_p}$ and $\mathbf{i_p}$, the primary active and reactive power in steady state can be calculated as follows in primary flux orientation frame:

$$P_p + jQ_p = \frac{3}{2}\mathbf{v_p} * \mathbf{i_p^*}$$
$$\approx \frac{3}{2}j\omega_p\Psi_p * \frac{1}{L_p}\left(\Psi_p - L_m\mathbf{i_s}\right)$$
$$= \frac{3}{2}\omega_p\left(j\Psi_p\right) * \frac{1}{L_p}\left[\left(\Psi_p - L_m i_{sd}\right) - jL_m i_{sq}\right]$$
$$= \frac{3\omega_p}{2L_p}\left[\Psi_p L_m i_{sq} + j\Psi_p(\Psi_p - L_m i_{sd})\right] \quad (3.36)$$

Thus, the primary active and reactive powers are given by:

$$P_p = \frac{3\omega_p}{2L_p}\Psi_p L_m i_{sq} \quad (3.37)$$

$$Q_p = \frac{3\omega_p}{2L_p}\Psi_p(\Psi_p - L_m i_{sd}) \quad (3.38)$$

Applying the fundamental BDFRM theory [98], one can establish the following condition for the machine torque production:

$$\omega_r = p_r\omega_{rm} = \omega_p + \omega_s \quad (3.39)$$

$$\theta_r = p_r\theta_{rm} = \theta_p + \theta_s \quad (3.40)$$

where $\omega_{rm} = \frac{d\theta_{rm}}{dt}$ is the rotor mechanical angular velocity (rad/s), p_r is the number of rotor poles, $\omega_{p,s} = \frac{d\theta_{p,s}}{dt}$ are the applied angular frequencies (rad/s) to the windings and $\theta_{r,p,s}$ are the angular positions of the respective reference frames.

3.3 Scalar Control

Scalar control, often referred to as V/f control, is the simplest control algorithm in which the machine air-gap flux is kept approximately at its maximum value for the best possible torque production out of the machine. The speed and frequency variation should be limited (usually effected in a ramp fashion e.g. using a discrete rate limiter) as the machine transient response to sudden step changes may lead to instability of operation. Thus, it is a suitable solution for general purpose applications (such as fans,

pumps, compressors, blowers and similar loads) where steady-state, rather than dynamic, performance is of main concern.

In an open loop mode (e.g. without speed feedback), the algorithm is entirely independent of the machine parameters and is purely sensor-less in nature replying exclusively on the machine response to desired frequency and voltage references. Stability issues are therefore much more pronounced in this case, and especially with larger variations of the set points which should therefore be kept in a relatively narrow range to avoid stability problems (if at all possible). By closing the speed loop using a shaft position sensor for speed detection, the performance is generally improved but stability problems still persist in case of larger speed variations despite the existence of a PI speed controller, which has been traditionally used as the simplest and yet a reasonably robust solution (however, load scheduling of the PI gains may be required).

When applying the scalar control to the BDFRM, the machine is usually started as a slip ring induction machine (IM) with a shorted secondary winding (by-passing though a partially-rated inverter). Once the machine has reached its no-load speed (determined by its losses as with classical IMs) close to the synchronous speed, the inverter is connected and the control enabled. Note that an auxiliary contactor is normally used for this purpose. Such a starting procedure is required to prevent the current overloading of the inverter during start up. The schematic diagram of the open loop and the closed loop scalar control algorithms for the BDFRM are shown in Fig. 3.3 and Fig. 3.4 respectively.

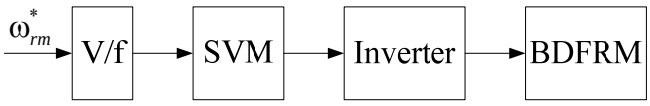

Figure 3.3: Schematic Diagram of the Open Loop Scalar Control Algorithm

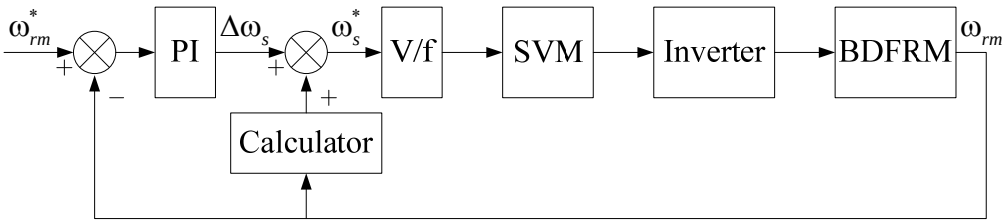

Figure 3.4: Schematic Diagram of the Close Loop Scalar Control Algorithm

As can be from Fig. 3.3, in the open-loop configuration, variable speed operation is obtained by varying the frequency of the 3-phase inverter according to Fig. 3.5. The closed-loop design in Fig. 3.4 consists of a conventional PI controller, a V/f block corresponding to Fig. 3.5, and a space vector modulation (SVM) block that converts the desired voltage and frequency signals into the corresponding switching patterns for the inverter to input the desired voltages to the BDFRM secondary winding terminals. Note that since the BDFRM is usually operating in a limited variable speed range around the synchronous speed (in order to use a smaller inverter and achieve associated cost benefits) where the secondary frequencies are small, the voltage boost in Fig. 3.5 is absolutely essential to compensate for the secondary winding resistive voltage drops (and particularly with smaller machines having larger resistances) and allow stable operation of the machine.

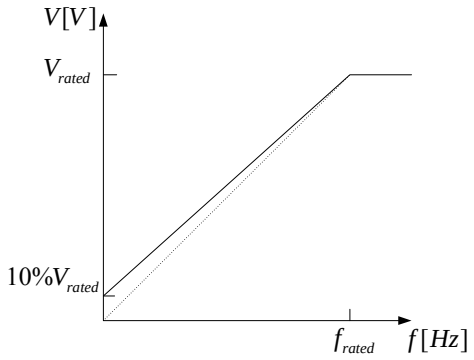

Figure 3.5: Constant V/f Control

3.4 Vector Control

Vector control allows much faster transient response and higher performance compared to the scalar control. Since the control is being executed in each of the two axes in a synchronously rotating d-q reference frame (to emulate the inherent control simplicity of classical DC machines as much as possible), a conversion of stationary frame measurements (e.g. voltages and currents) is required and algorithms themselves are eminently more complicated than scalar control counterparts. For this reason, a vector control scheme is computationally more intensive and needs DSP implementation on fast micro-processors (which are fairly standardised, mass produced and reasonably cost-effective these days) to achieve high control rates necessary for good dynamic performance. A typical structure of torque vector control is shown in Fig. 3.6.

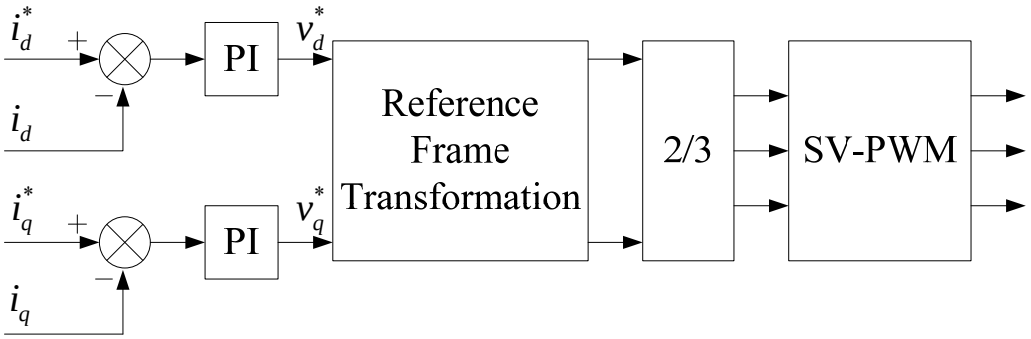

Figure 3.6: Schematic Diagram of Vector Control Algorithm

As can be seen from the figure above, referenced voltage signals (v_d^*, v_q^*) come as outputs of the respective seemingly independent (if it was not for magnetic coupling that may exist in some circumstances as discussed) current control loops (one for each axis) in a properly chosen synchronously rotating reference frame. The measured phase currents (by current transducers in two phases for machines designed with an isolated neutral point) are firstly converted to their stationary frame d-q components and further to the corresponding rotating frame counterparts (i_d, i_q) in Fig. 3.6 using

the measured (in sensor based systems) or estimated (in sensor-less systems) reference frame position. The reference current signals (i_d^*, i_q^*) are dictated by the desired torque/power (not shown in the figure above). The reference voltages are fed to the Space Vector PWM to generate appropriate switching patterns for the IGBTs for the desired voltages to be applied to the machine terminals.

When the synchronous reference frame d-axis is aligned with the primary flux (this is known as the field-oriented control or FOC), Ψ_p is virtually constant (and especially with larger machines having lower resistances). Hence, T_e is controlled by the secondary q-axis current (i_{sq}) and Q_p is controlled by the secondary d-axis current (i_{sd}). In this case, the current control in Fig. 3.6 is inherently decoupled (for either DFIM or BDFRM) which is the principal advantage of the FOC over classical voltage orientated vector control. The magnitude and angle of Ψ_p in a stationary frame can be calculated from:

$$\boldsymbol{\Psi_p} = \Psi_p e^{j\theta_p} = \int(\mathbf{u_p} - R_p \mathbf{i_p})dt \simeq \int \mathbf{u_p} dt \qquad (3.41)$$

where $\mathbf{u_p}$ and $\mathbf{i_p}$ could be easily determined from the measured phase quantities. Using (3.40), one can now find the secondary frame position (θ_s) from encoder measurement of rotor angle (θ_{rm}). Therefore, some performance optimisation of the BDFRM may be achieved, such as, maximum torque per secondary ampere when $i_{sd} = 0$ (in which case all of the secondary current would be torque producing) and maximum primary side power factor when $\Psi_p = L_m i_{sd}$ (providing the machine is appropriately rated and it has a sufficiently large converter to accommodate the necessary Q requirement from the secondary side) etc.

Another frequently used vector control method is primary voltage orientation in which case the synchronous reference frame q-axis should be aligned with the

primary voltage vector (Fig. 3.7). Obviously, with larger machines having negligible resistances, this approach would be very close to the FOC as the primary flux would then be virtually aligned with the d-axis. However, generally speaking, this is not quite the case and the primary flux would slightly lead the d-axis depending on the primary winding resistance value. A phase locked loop (PLL) is commonly used to identify the supply frequency (angular velocity) from the input voltage waveforms filtering out noise and DC offset in the process. However, the down side of this filtering is that phase delays can be introduced so using PLL for detecting the stationary frame voltage angle is not recommended. A better approach here is to simply identify this angle directly from the respective d-q voltage components in a stationary frame that can be easily calculated from the phase voltage measurements.

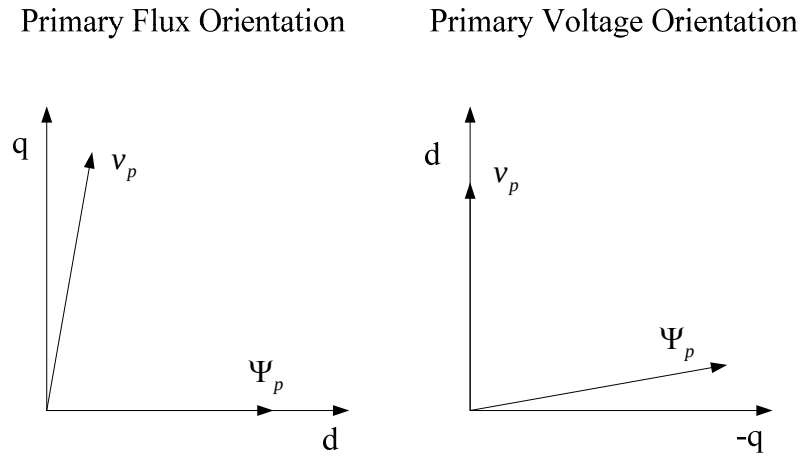

Figure 3.7: Reference Frame Orientation

3.5 Direct Torque Control (DTC)

DTC of the BDFRM is used to control the secondary flux and electromagnetic torque directly in a ‘bang-bang’ fashion. Compared to the other advanced control techniques such as VC, the DTC eliminates the current control loops but needs higher and variable switching rates for hysteresis type of control. Also, DTC has low frequency stability problems because of flux estimation inaccuracies caused by resistance

variations at lower supply voltages. Under these operating conditions, DTC is clearly inferior to VC.

To achieve direct torque control, a form of secondary flux and electromagnetic torque could be found in:

$$\boldsymbol{\Psi_s} = \Psi_{sd} + j\Psi_{sq} = \sigma L_s i_{sd} + \Psi_{ps} + j\sigma L_s i_{sq} \tag{3.42}$$

$$T_e = -\frac{3p_r}{2\sigma L_s}\left|\boldsymbol{\Psi_{ps}} \times \boldsymbol{\Psi_s}\right| = -\frac{3p_r}{2\sigma L_s}\frac{L_m}{L_p}\Psi_p \Psi_s \sin\delta \tag{3.43}$$

where $\sigma = 1 - \frac{L_m^2}{L_p L_s}$ is the leakage factor, δ is the angle between mutual flux and secondary flux, and Ψ_{ps} is the primary flux linking the secondary winding, which is fact the mutual flux, $\Psi_{ps} = \frac{L_m}{L_p}\Psi_p$. From (3.42), one can see that Ψ_{sq} is a torque producing secondary flux component since it is directly proportional to i_{sq}. In order to alter instantaneous torque for certain Ψ_s magnitude, appropriate voltage vectors are to be applied to the secondary winding to instantly change δ, and therefore $\delta + \theta_s$, accordingly, since θ_s variations are negligible, and especially at low ω_s, over a short DTC sampling interval. Thus, there is no need to know the secondary reference frame position and DTC can be implemented in a stationary reference frame (Fig. 3.8).

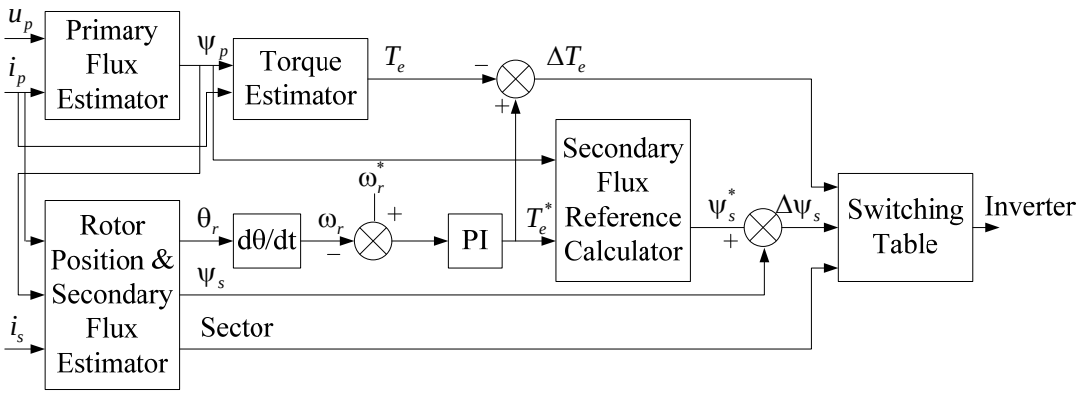

Figure 3.8: Schematic Diagram of DTC Algorithm

In the above DTC scheme, $\Delta\Psi_s$ and ΔT_e are defined as:

$$\Delta\Psi_s = \begin{cases} 1, & \Psi_s^* - \Psi_s \geq \Delta\Psi \\ 0, & \Psi_s^* - \Psi_s \leq -\Delta\Psi \end{cases} \quad (3.44)$$

$$\Delta T_e = \begin{cases} 1, & T_e^* - T_e \geq \Delta T \\ 0, & T_e^* - T_e \leq 0, \omega_s \geq 0; T_e^* - T_e \geq 0, \omega_s \leq 0 \\ -1, & T_e^* - T_e \leq -\Delta T \end{cases} \quad (3.45)$$

where $\Delta\Psi$ and ΔT indicate a half width of the corresponding hysteresis bands.

Table 3.1: Optimum Switching Look-up Table in DTC

Comparator		Sector					
$\Delta\Psi_s$	ΔT_e	1	2	3	4	5	6
1	1	$\underline{U}_2$	$\underline{U}_3$	$\underline{U}_4$	$\underline{U}_5$	$\underline{U}_6$	$\underline{U}_1$
	0	$\underline{U}_7$	$\underline{U}_0$	$\underline{U}_7$	$\underline{U}_0$	$\underline{U}_7$	$\underline{U}_0$
	-1	$\underline{U}_6$	$\underline{U}_1$	$\underline{U}_2$	$\underline{U}_3$	$\underline{U}_4$	$\underline{U}_5$
0	1	$\underline{U}_3$	$\underline{U}_4$	$\underline{U}_5$	$\underline{U}_6$	$\underline{U}_1$	$\underline{U}_2$
	0	$\underline{U}_0$	$\underline{U}_7$	$\underline{U}_0$	$\underline{U}_7$	$\underline{U}_0$	$\underline{U}_7$
	-1	$\underline{U}_5$	$\underline{U}_6$	$\underline{U}_1$	$\underline{U}_2$	$\underline{U}_3$	$\underline{U}_4$

Table 3.2: Effects of Voltage Vectors on BDFRM Torque in DTC

ω_s	ΔT_e	Torque Changes	
		$\omega_{rm} > 0$	$\omega_{rm} < 0$
>0	1	↑	↑
	0	↓	↑
	-1	↓	↓
<0	1	↑	↑
	0	↑	↓
	-1	↓	↓

The secondary side voltage vectors generated by the inverter to achieve a desired control action with the minimum number of switching are given in Table 3.1. The

binary codes, indicating the switching status of individual inverter legs ('1' representing the top of a leg ON and the bottom OFF, and '0' vice versa) and angular positions of these vectors in a stationary reference frame are presented in Fig. 3.9.

The main task of the controller is to ensure that the secondary flux and machine torque are within the user specified hysteresis bands under all operating conditions of the machine. According to (3.44), Ψ_s should be in the range of $[\Psi_s^* - \Delta\Psi,\ \Psi_s^* + \Delta\Psi]$ with $\Delta\Psi_s = 1$ voltage vectors increasing, and $\Delta\Psi_s = 0$ vectors decreasing the Ψ_s magnitude (Table 3.1). Similarly in (3.45), $\Delta T_e = 1$ means an increase, and $\Delta T_e = -1$ means a decrease of the actual torque. However, the influence of zero voltage vectors ($\underline{U}_0 = 000$ and $\underline{U}_7 = 111$) on torque is opposite at super- and sub-synchronous speed mode of the BDFRM; at super-synchronous speeds the torque will be decreased and at sub-synchronous speed the torque will be increased in Table 3.2. As a result, in the super-synchronous speed region, the torque is controlled in the bottom half-band $[T_e^* - \Delta T,\ T_e^*]$, and in sub-synchronous speed region, it is in the top half-band $[T_e^*,\ T_e^* + \Delta T]$.

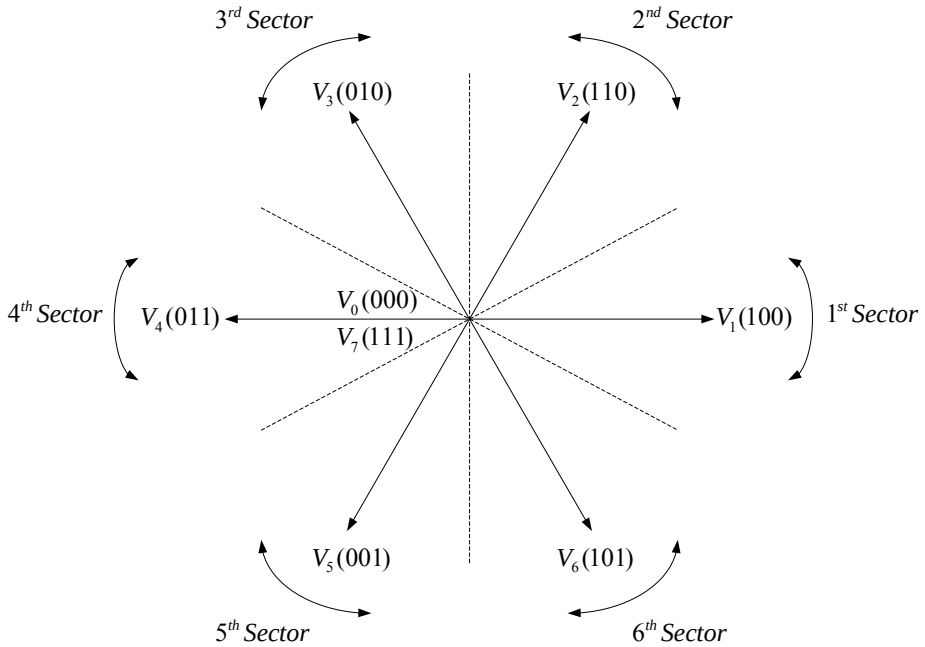

Figure 3.9: Voltage Vectors ($\underline{U}_0 = 000,\ \underline{U}_1 = 100,\ \underline{U}_2 = 110,\ \underline{U}_3 = 010,\ \underline{U}_4 = 011,\ \underline{U}_5 = 001,\ \underline{U}_6 = 101,\ \underline{U}_7 = 111$)

3.6 Direct Power Control (DPC)

DPC of the BDFRM is a method to control the primary active and reactive power directly. There are quite a lot of commonalities between DPC and DTC, such as elimination of current control loops, requirement of high and variable switching rates, higher switching losses in the inverter and consequently lower converter efficiency compare to VC etc. A schematic diagram of DPC is shown in Fig. 3.10. The actual power inputs to the hysteresis comparators have been computed using the primary side current and voltage. The outputs of the hysteresis comparators, giving errors between the desired and measured power, make it possible to find the relevant look-up tables in the control software and choose an appropriate voltage vector to be applied to the secondary terminals. The optimal switching vectors are shown in Table 3.3 whilst the corresponding binary patterns, showing the switching status of inverter legs, are the same as with DTC in Fig. 3.9. Implementing the switching logic in Table 3.3 ensures the control of $\mathrm{P_p}$ and $\mathrm{Q_p}$ is affected within a narrow and user-specified band around the reference values with $\mathrm{P_p} \in [\mathrm{P_p^*} - \Delta\mathrm{P}, \mathrm{P_p^*} + \Delta\mathrm{P}]$ and $\mathrm{Q_p} \in [\mathrm{Q_p^*} - \Delta\mathrm{Q}, \mathrm{Q_p^*} + \Delta\mathrm{Q}]$. $\Delta\mathrm{P}$ and $\Delta\mathrm{Q}$ indicate a half width of the corresponding hysteresis bands. Similarly to DTC that is using Ψ_s for sector selection, in the DPC scheme the secondary flux estimation is not required and instead this is controlled indirectly through monitoring $\Delta\mathrm{Q_p}$ under particular voltage conditions 9 [125].

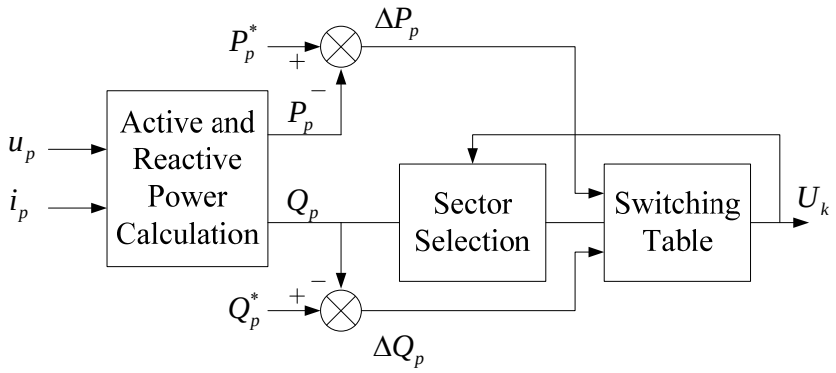

Figure 3.10: Schematic Diagram of DPC Algorithm

Table 3.3: Optimum Switching Vectors in DPC

Error		Sector					
$P_p^* - P_p$	$Q_p^* - Q_p$	1	2	3	4	5	6
$> \Delta P$	$> \Delta Q$	$\underline{U}_3$	$\underline{U}_4$	$\underline{U}_5$	$\underline{U}_6$	$\underline{U}_1$	$\underline{U}_2$
$> \Delta P$	$\leq -\Delta Q$	$\underline{U}_2$	$\underline{U}_3$	$\underline{U}_4$	$\underline{U}_5$	$\underline{U}_6$	$\underline{U}_1$
$\leq \Delta P$	$> \Delta Q$	$\underline{U}_5$	$\underline{U}_6$	$\underline{U}_1$	$\underline{U}_2$	$\underline{U}_3$	$\underline{U}_4$
$\leq \Delta P$	$\leq -\Delta Q$	$\underline{U}_6$	$\underline{U}_1$	$\underline{U}_2$	$\underline{U}_3$	$\underline{U}_4$	$\underline{U}_5$

3.7 Conclusions

In this chapter, the fundamental theory of both the DFIM and the BDFRM has been introduced. The dynamic models of these two machines are similar (the primary winding and the secondary winding of the BDFRM play the roles of the stator winding and the rotor winding of the DFIM respectively). For this reason, the control algorithms for the BDFRM will be only considered in the following sections.

The main control algorithms e.g. scalar control, VC, DTC and DPC, have been discussed in detail, stating their advantages and/or limitations. Scalar control has the simplest structure but has poor dynamic performance and is only suitable for general-purpose applications. Vector control generally offers high performance, trading off parameter dependence with decoupling compensation schemes, and requires DSP implementation on fast micro-processors to achieve high control rates. DTC & DPC eliminate current control loops, they are more robust but at the expense of parameter dependence (DTC) and inevitable inaccuracies in flux estimation caused by resistance variations at lower supply voltages and back-emf values. Based on the above, it has been decided to use parameter-independent VC as the most appropriate solution for simulation studies and practical implementation on the DFIM/BDFRM test rigs in the power laboratory for subsequent performance comparisons.

4. Vector Control Algorithm

4.1 Introduction

A VC algorithm has been introduced, reviewed and discussed in the previous chapters. Since the DFIM and the BDFRM have similar dynamic modelling, in this chapter, a stator/primary voltage oriented vector control scheme will be implemented for the machine side converter (MSC) and the grid side converter (GSC), both of conventional design, to allow bi-directional power flow of the BDFRM through the secondary winding side in either motoring or generating mode. The controllers for both the converters have an inner-loop for current control and an outer-loop for power control (MSC) or voltage control (GSC). Further design details of the entire VC for the machine will be presented in the following sections.

4.2 Vector Control of the Machine Side Converter (MSC)

A typical stator/primary voltage oriented vector control of the MSC for the BDFRM is shown in Fig. 4.1.

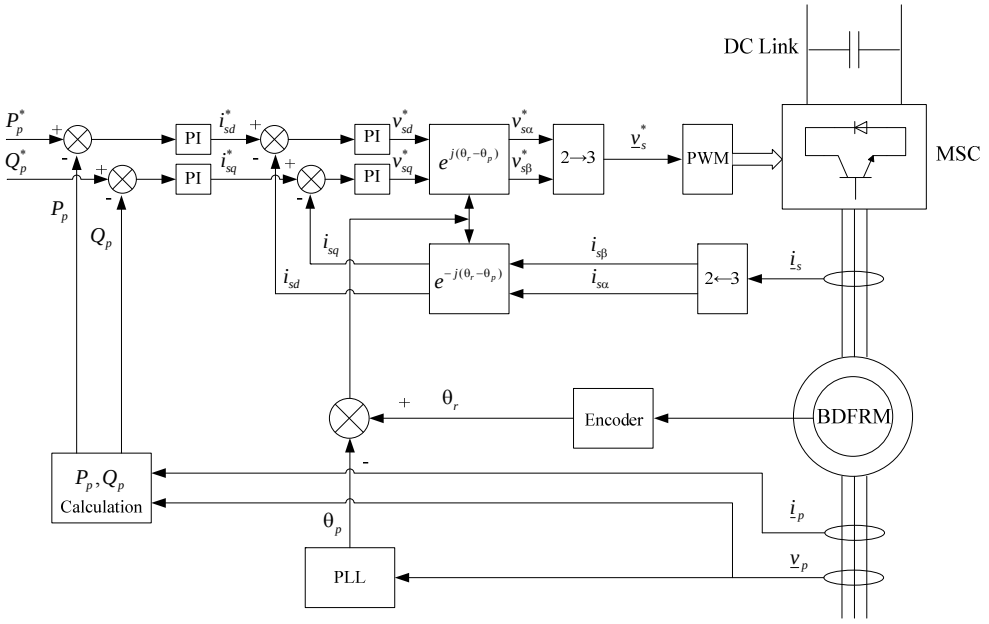

Figure 4.1: Vector Control on MSC of the BDFRM

The VC here requires the measurements of the primary and secondary currents, primary voltage and rotor shaft position in order to control primary active and reactive power.

4.2.1 Inner Loop Derivation

The control form expressions can be derived from the generic space-vector BDFRM model in an arbitrary reference frame by setting $\omega = \omega_p$ in (3.20) and (3.21). In this case, the secondary voltage and flux equations become:

$$\mathbf{v_s} = R_s\mathbf{i_s} + \frac{d\mathbf{\Psi_s}}{dt} + j(\omega_r - \omega_p)\mathbf{\Psi_s} \tag{4.1}$$

$$\mathbf{\Psi_s} = L_s\mathbf{i_s} + L_m\mathbf{i_p^*} \tag{4.2}$$

Using (3.22), the secondary flux equation above can be rearranged as follows:

$$\mathbf{\Psi_s} = \sigma L_s\mathbf{i_s} + \frac{L_m}{L_p}\mathbf{\Psi_p^*} \tag{4.3}$$

or further into:

$$\mathbf{\Psi_s} = \sigma L_s\mathbf{i_s} + \mathbf{\Psi_m} \tag{4.4}$$

where $\sigma = 1 - \frac{L_m^2}{L_p L_s}$ is the leakage factor defined as with induction machines, and Ψ_m is the primary flux linking the secondary winding (i.e. the mutual or magnetising flux). Substituting (4.4) into (4.1) gives:

$$\mathbf{v_s} = R_s\mathbf{i_s} + \sigma L_s\frac{d\mathbf{i_s}}{dt} + \frac{d\mathbf{\Psi_m}}{dt} + j\omega_s\sigma L_s\mathbf{i_s} + j\omega_s\mathbf{\Psi_m} \tag{4.5}$$

which in steady-state becomes:

$$\mathbf{v_s} = R_s\mathbf{i_s} + j\omega_s\sigma L_s\mathbf{i_s} + j\omega_s\mathbf{\Psi_m} \tag{4.6}$$

or

$$\mathbf{v_s} = (R_s + j\omega_s\sigma L_s)\mathbf{i_s} + j\omega_s\mathbf{\Psi_m} \tag{4.7}$$

where $\omega_s = \omega_r - \omega_p$ is the secondary winding angular frequency (rad/s). Equation (4.7) shows a proportional relationship between the secondary side voltage and the

secondary side current with a constant flux linkage offset component. It could be written in d-q form as

$$\begin{cases} v_{sd} = R_s i_{sd} - (\omega_s \sigma L_s i_{sq} + \omega_s \Psi_{mq}) \\ v_{sq} = R_s i_{sq} + (\omega_s \sigma L_s i_{sd} + \omega_s \Psi_{md}) \end{cases} \tag{4.8}$$

The terms in brackets constitute voltage-compensation terms to ensure fast tracking of the currents. But during simulations and real experiments, these compensation terms are not essential and could be avoided. Thus, a control scheme using a feedback PI controller could be simply formulated as:

$$\begin{cases} v_{sd}^* = (k_{p_1} + \frac{k_{i_1}}{s})(i_{sd}^* - i_{sd}) \\ v_{sq}^* = (k_{p_1} + \frac{k_{i_1}}{s})(i_{sq}^* - i_{sq}) \end{cases} \tag{4.9}$$

4.2.2 Outer Loop Derivation

The relationships between the primary real and reactive power and the secondary d-q currents can be derived starting from a conventional expression for apparent power:

$$S_p = P_p + jQ_p = \frac{3}{2}\mathbf{v_p}\mathbf{i_p^*} \tag{4.10}$$

Since:

$$\mathbf{\Psi_p} = L_p \mathbf{i_p} + L_m \mathbf{i_s^*} \tag{4.11}$$

it follows that:

$$\mathbf{i_p} = \frac{1}{L_p}\mathbf{\Psi_p} - \frac{L_m}{L_p}\mathbf{i_s^*} \tag{4.12}$$

Substituting for (4.12) into (4.10), one obtains:

$$S_p = P_p + jQ_p = \frac{3}{2}\mathbf{v_p}(\frac{1}{L_p}\mathbf{\Psi_p} - \frac{L_m}{L_p}\mathbf{i_s^*})^* \tag{4.13}$$

or:

$$S_p = P_p + jQ_p = \frac{3}{2}\mathbf{v_p}(\frac{1}{L_p}\mathbf{\Psi_p^*} - \frac{L_m}{L_p}\mathbf{i_s}) \tag{4.14}$$

By neglecting the primary resistance for convenience, the primary flux vector is known to be lagging the primary voltage vector ($\mathbf{v_p}$) by $\frac{\pi}{2}$ rad, while its conjugate $\mathbf{\Psi_p^*}$ is ahead of $\mathbf{v_p}$ by $\frac{\pi}{2}$ rad. Thus, $\mathbf{v_p} * \mathbf{\Psi_p^*} = 0$. In a primary voltage oriented form (i.e. $v_{pq} = 0$) of (4.14), the real and reactive power expressions become:

$$\begin{cases} P_p = -\frac{3L_m}{2L_p} v_{pd} i_{sd} \\ Q_p = -\frac{3L_m}{2L_p} v_{pd} i_{sq} \end{cases} \tag{4.15}$$

The above relationships imply that P_p,Q_p are proportional to i_{sd}, i_{sq} respectively, which justifies the implementation of the following simple PI control law,

$$\begin{cases} i_{sd}^* = (k_{p_2} + \frac{k_{i_2}}{s})(P_p^* - P_p) \\ i_{sq}^* = (k_{p_2} + \frac{k_{i_2}}{s})(Q_p^* - Q_p) \end{cases} \tag{4.16}$$

4.3 Vector Control of the Grid Side Converter (GSC)

A typical primary voltage oriented vector control of the GSC for the BDFRM is shown in Fig. 4.2.

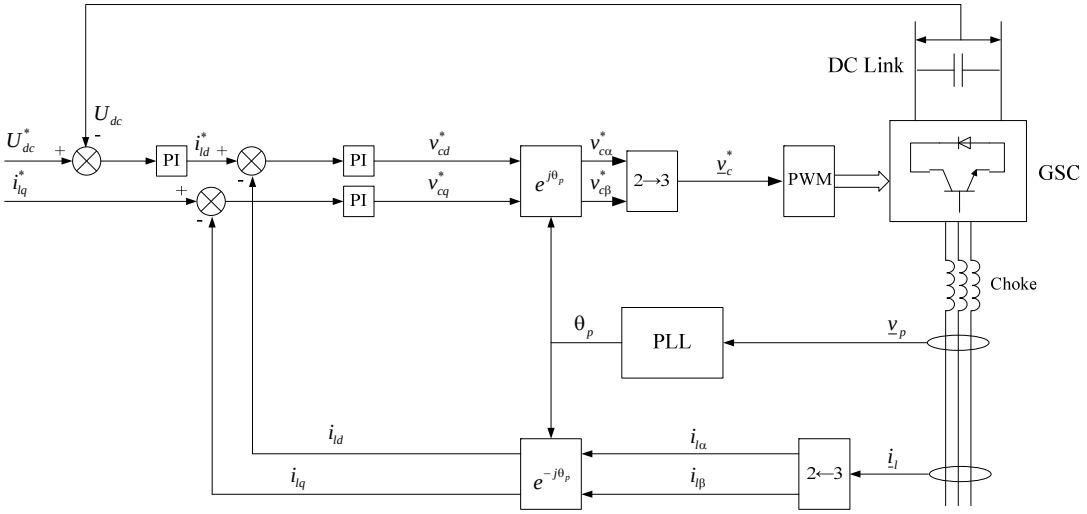

Figure 4.2: Vector Control on GSC of the BDFRM

The VC here requires the measurements of the grid side currents, primary voltages and DC link voltage in order to control the DC link voltage and q components of the line side current.

4.3.1 Inner Loop Derivation

By taking the power flow from the grid to the GSC as reference (positive) direction, the relationship between the choke impedance (Z), the grid side current ($\mathbf{i_l}$), the grid and inverter voltage vectors ($\mathbf{v_p}, \mathbf{v_c}$) is:

$$\mathbf{i_l} = \frac{1}{Z}(\mathbf{v_p} - \mathbf{v_c}) \tag{4.17}$$

Assuming the primary voltage orientation of the reference frame here:

$$\mathbf{v_c} = v_p - Z\mathbf{i_l} \tag{4.18}$$

Equation (4.18) indicates a proportional relationship between the inverter voltage ($\mathbf{v_c}$) and the line side current ($\mathbf{i_l}$), which suggests a current control law:

$$\begin{cases} v_{cd}^* = (k_{p_3} + \frac{k_{i_3}}{s})(i_{ld}^* - i_{ld}) \\ v_{cq}^* = (k_{p_3} + \frac{k_{i_3}}{s})(i_{lq}^* - i_{lq}) \end{cases} \tag{4.19}$$

4.3.2 Outer Loop Derivation

The relationship between the grid side apparent power ($\mathbf{S}_g$), the grid side current ($\mathbf{i_l}$) and primary side voltage ($\mathbf{v_p}$) is,

$$\mathbf{S}_g = P_g + jQ_g = \frac{3}{2}\mathbf{v_p}\mathbf{i_l^*} \tag{4.20}$$

which in primary voltage oriented terms (i.e. $v_{pq} = 0$, $v_{pd} = v_p$) can be written as:

$$S_g = P_g + jQ_g = \frac{3}{2}v_p\mathbf{i_l^*} \tag{4.21}$$

Thus,

$$\begin{cases} P_g = \frac{3}{2} v_p i_{ld} \\ Q_g = -\frac{3}{2} v_p i_{lq} \end{cases} \tag{4.22}$$

P_g is known to be directly proportional to the DC link voltage (U_{dc})[126], hence i_{ld} is proportional to U_{dc}, and Q_g is proportional to i_{lq}. Normally, in VC, i_{lq} reference is set to 0 to achieve the unity power factor on the grid side. Therefore, a control law could be formulated as follows:

$$i_{ld}^* = (k_{p_4} + \frac{k_{i_4}}{s})(U_{dc}^* - U_{dc}) \tag{4.23}$$

4.4 Conclusions

The primary voltage oriented vector control of the MSC and the GSC of the BDFRM has been presented and basic principles explained using schematic diagrams. The important control form relationships have been derived and justifications for adopting simple PI control approaches have been provided. Due to the machine parameter independence, the primary voltage oriented control has an advantage over the primary flux oriented vector control and will be applied to the machine for both the simulations and experiments, the results of which will be shown in the following chapters.

5. Simulation Study

5.1 Introduction

In order to examine the performance of the DFIM and the BDFRM when being operated under the vector control strategies outlined in Chapter 4, a computer simulation programme has been developed in Simulink® using the machine parameters obtained by off-line testing on the two existing test rigs (see Appendices A and B for details). Its overall structure and the functions of the major components are described in the following section. In order to make the simulation as realistic as possible, it consists of components used for real-time implementation such as the PLL (to obtain the angular velocity and/or angular position of the supply voltage vector), the PWM generator, a pipelined control evaluation procedure to prevent computational delays from altering the control output times, and a machine d-q model neglecting core losses.

Due to the problem issued in Chapter 6, the line supply voltage during the entire experiment has been changed to 190 V (line-to-line) from 415 V (shown on the machines' nameplate in Appendix A), the voltage rating in the simulation models has also been adjusted accordingly to adequately reflect the actual voltage conditions in the lab environment. The space vector PWM carrier frequency has been set to 5 kHz, with a DC link referenced voltage to 300V. When the rotor (DFIM) or the secondary (BDFRM) windings are short circuited, both the machines can be started by connecting the stator (DFIM) or the primary winding (BDFRM) to the grid, which is the same starting procedure as that used for a Squirrel Cage Induction Machine (SCIM). Figs. 5.1 and 5.2 show the starting transients of the stator current, short-circuited rotor current, rotating speed and electromagnetic torque under variable loading conditions (-40 Nm to 40 Nm) of the DFIM. Figs. 5.3 and 5.4 depict similar operating characteristics but for the BDFRM.

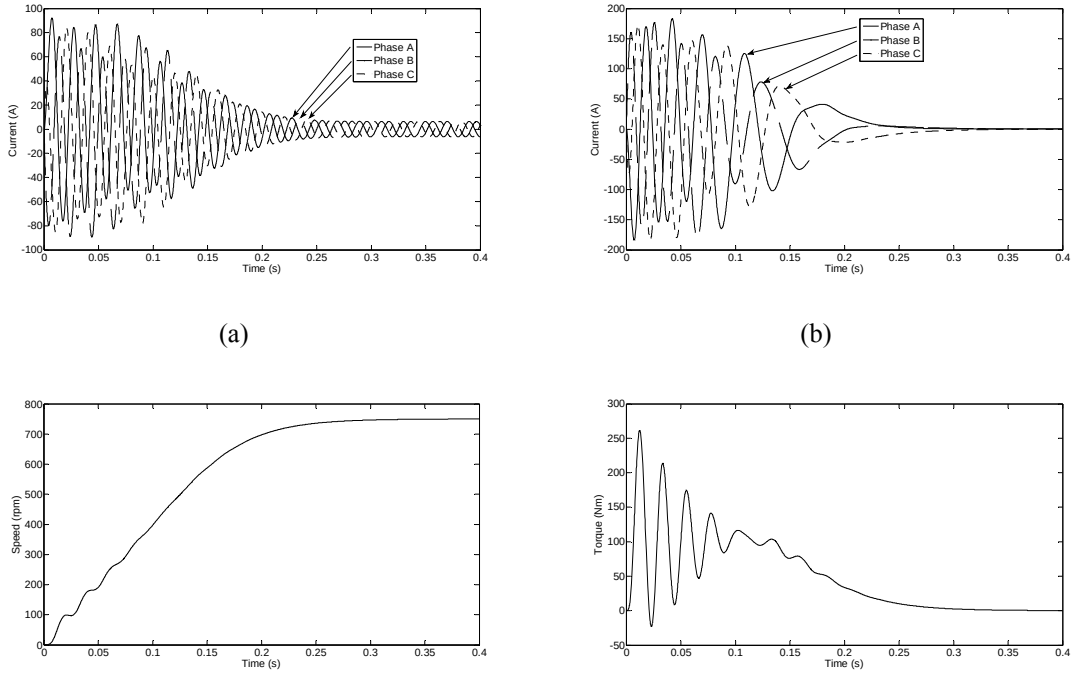

(a) (b)

(c) (d)

Figure 5.1: Start-up of the unloaded DFIM with Short Circuited Rotor Windings. (a) 3-phase Stator Current; (b) 3-phase Rotor Current; (c) Rotating Speed; (d) Electromagnetic Torque

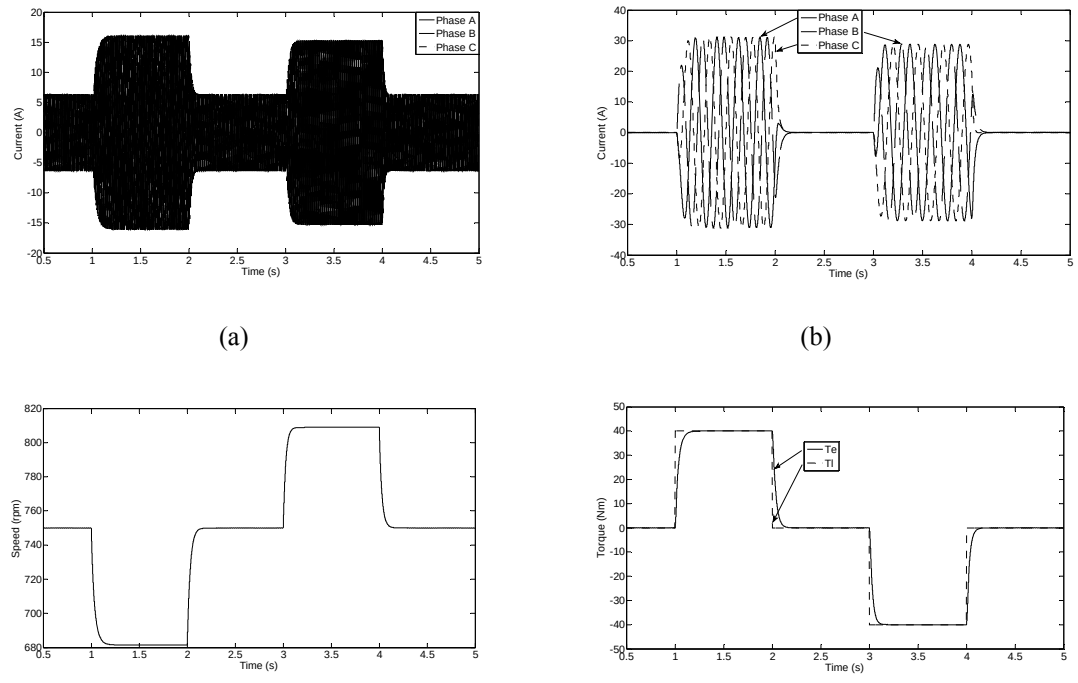

(a) (b)

(c) (d)

Figure 5.2: Variable Loading Conditions of the DFIM. (a) 3-phase Stator Current; (b) 3-phase Rotor Current; (c) Rotating Speed; (d) Electromagnetic Torque and Load Torque

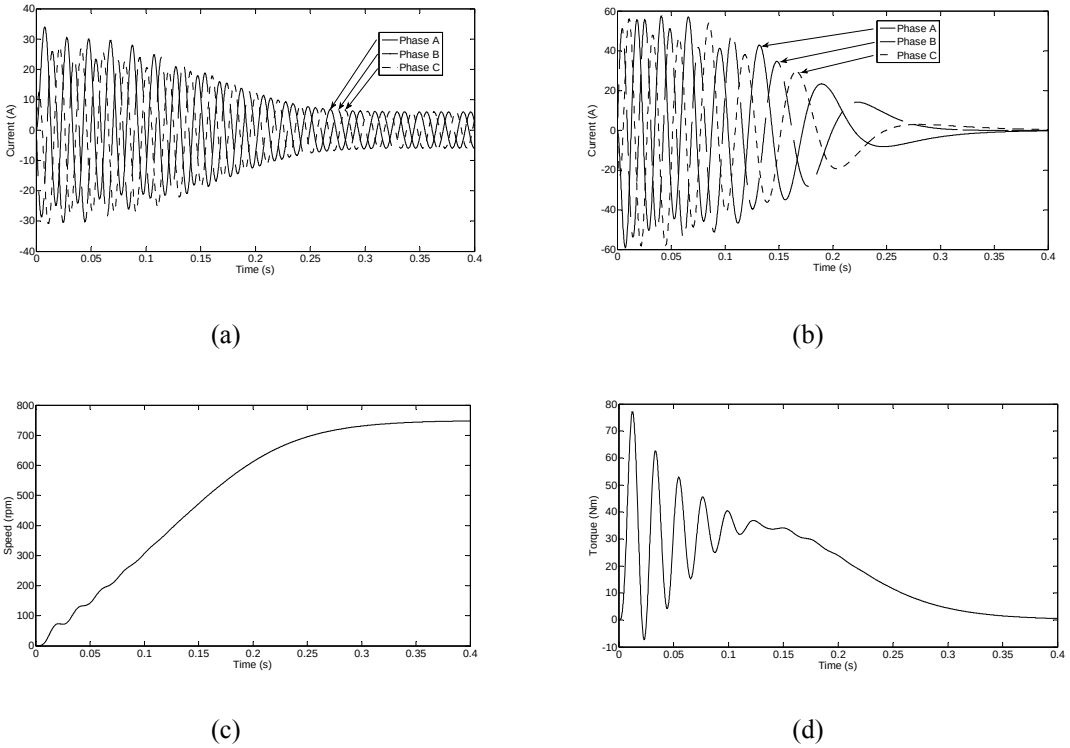

(a) (b)

(c) (d)

Figure 5.3: Starting of the unloaded BDFRM with Short Circuited Secondary Windings. (a) 3-phase Primary Current; (b) 3-phase Secondary Current; (c) Rotating Speed; (d) Electromagnetic Torque

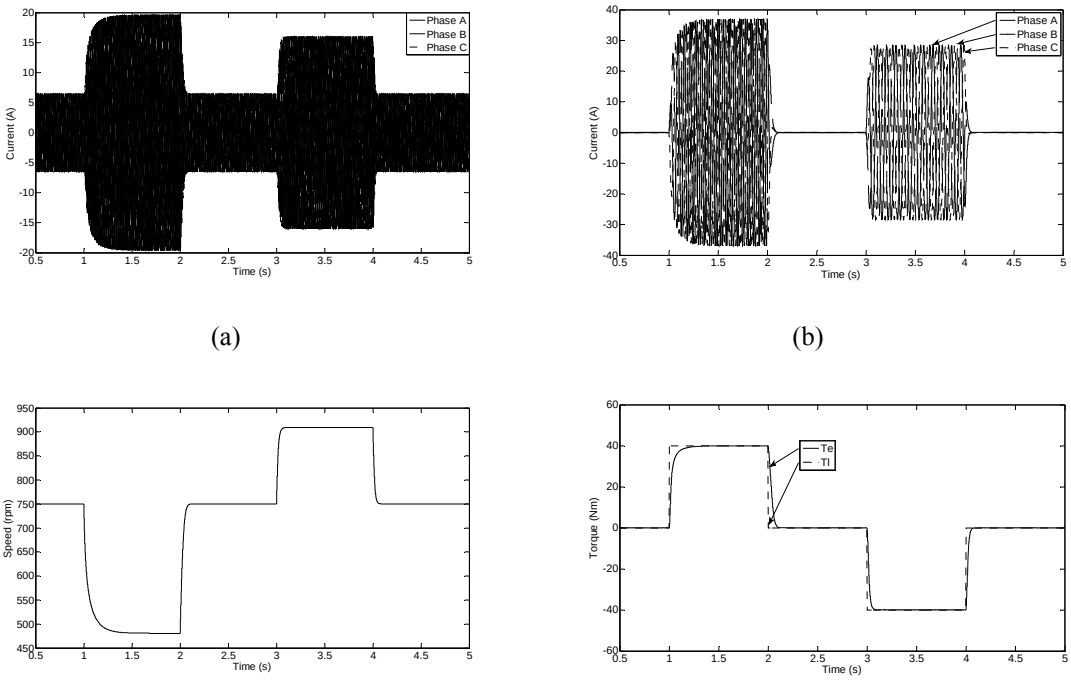

(a) (b)

(c) (d)

Figure 5.4: Variable Loading Conditions of the BDFRM. (a) 3-phase Primary Current; (b) 3-phase Secondary Current; (b) Rotating Speed; (c) Electromagnetic Torque and Load Torque

As may be seen from Figs. 5.1 and 5.3, largely because of the smaller inertia than the equivalent DFIM, the unloaded BDFRM requires lower starting torque and current to reach the same synchronous speed (750 rpm) for the same stator/primary voltage. For this reason, the BDFRM should have inherently lower fault current levels and thus superior low voltage fault ride through capabilities compared to the DFIM counterpart in wind power or similar applications [4-9]. From the same figures, one can also observe that due to the smaller reactance, the start-up period of the DFIM to accelerate to 750 rpm is slightly shorter (≈0.3s) than the BDFRM's (≈0.4s).

According on Figs. 5.2 and 5.4, since the load torque varies from motoring (40 Nm) to generating (-40 Nm), the shaft speed alters from sub-synchronous to super-synchronous respectively, and the phase sequence of the rotor/secondary side current shifts from ABC to ACB as expected. Note that the rotor/secondary winding (slip) frequencies are not the same for these two speed modes (in absolute sense with different sign resulting from the opposite phase sequence of the rotor/secondary winding to the stator/primary winding as indicated above) and correspond to the slip values dictated by the loading conditions at fixed supply voltage.

In the following sections, vector controlled GSC will be operated without machine parameters, while vector controlled MSC will be simulated on both the DFIM and the BDFRM at torque mode (fixed speed) and speed mode (close-loop speed control with variable speed operation).

5.2 Controller Simulator

This section describes the control simulation programme for the BDFRM. It is divided into two subsections; the first outlines the controller simulator in general, and the second looks in detail at the major components and their functions.

5.2.1 Programme Overview

A functional block diagram of the algorithmic structure of the BDFRM simulation programme is shown in Fig. 5.5. As can be seen, the vector controller is primary voltage oriented and performs its calculations in the synchronously rotating d-q frame. It consists of the hierarchically arranged speed and current (torque) loops with anti-windup conventional PI regulators.

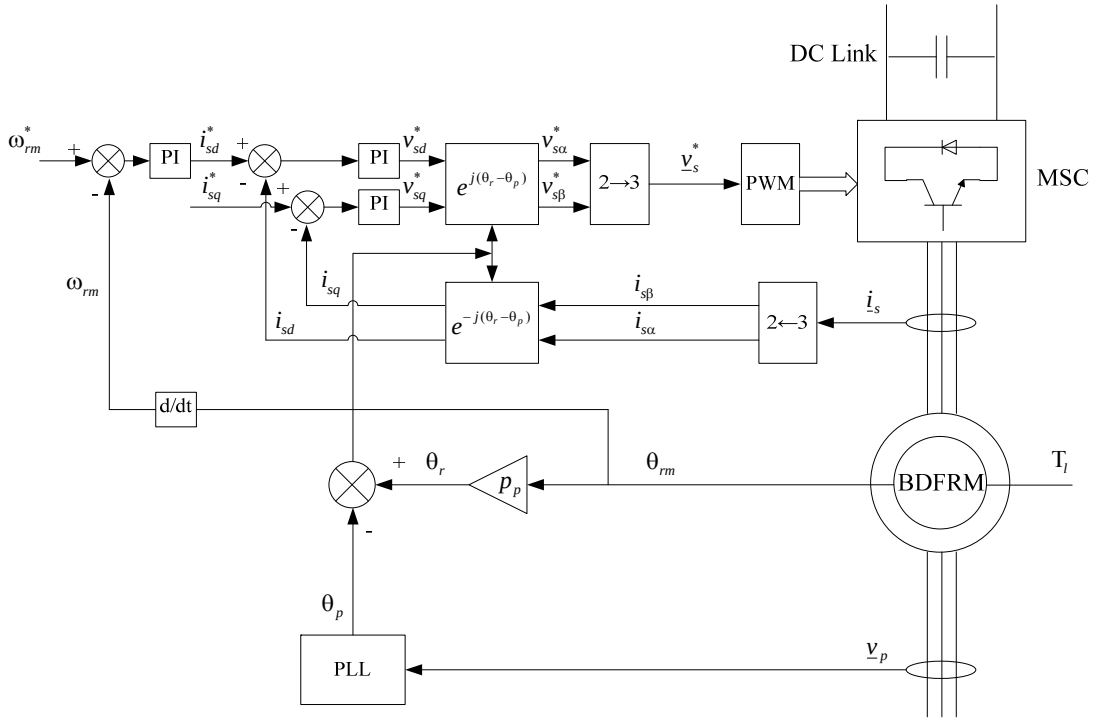

Figure 5.5: Schematic Diagram of the Vector Controlled BDFRM Simulation Programme

The inner loop is the current loop (one for each axis). The desired d-q components of the secondary current are fed as references (i^*_{sd} and i^*_{sq}) to these loops. The outer, angular velocity, loop generates the necessary d component of the secondary current i^*_{sd} to produce the required torque. The desired d-q secondary voltages to be applied to the BDFRM (v^*_{sd} and v^*_{sq}) are outputs of the current loops. After the inverse Park transformation, the signals are passed into the space-vector PWM generator which

then converts them into an appropriate switching pattern for the inverter legs. The resultant PWM waveforms drive the BDFRM model. The main reason for choosing the space-vector based PWM algorithm is that the pulse width can be evaluated on-line. This eliminates the need for the look-up tables of stored values which are necessary with the sinusoidal PWM algorithms. A conventional d-q model for the BDFRM has been used having 3-phase primary voltage ($\underline{v}_p$) and load torque (T_l) as inputs, and outputs including 3-phase secondary currents ($\underline{i}_s$), angular speed (ω_{rm}) and rotor position (θ_{rm}) in arrays containing a number of values sampled over the control interval. In real-time implementation, $\underline{v}_p$ and $\underline{i}_s$ are measured by transducers, while ω_{rm} and θ_{rm} are acquired by a shaft position encoder.

The functionality of the control blocks in Fig. 5.5 will now be described in detail. They are mainly presented in the order they are executed in the control flow through the main module of the simulation code.

5.2.2 Current Calculator

The block's task is to determine the control currents (i_{sd} and i_{sq}) from the measured 3-phase current ($\underline{i}_s$). It is based on the conventional Park's transformation which, for a machine with no neutral connection (no zero sequence current component), can be written in a matrix form as:

$$\begin{bmatrix} i_{sd} \\ i_{sq} \end{bmatrix} = \frac{2}{3} \begin{bmatrix} \cos(\theta_r - \theta_p) & \cos\left(\theta_r - \theta_p - \frac{2}{3}\pi\right) & \cos\left(\theta_r - \theta_p + \frac{2}{3}\pi\right) \\ -\sin(\theta_r - \theta_p) & -\sin\left(\theta_r - \theta_p - \frac{2}{3}\pi\right) & -\sin\left(\theta_r - \theta_p + \frac{2}{3}\pi\right) \end{bmatrix} \begin{bmatrix} i_{sa} \\ i_{sb} \\ i_{sc} \end{bmatrix} \quad (5.1)$$

The angle $\theta_r - \theta_p$ in (5.1) corresponds to the middle of the previous control interval in order to take into account the movement of the d-q frame, particularly at higher speeds. This is calculated as the mean value of the angles at the current and previous control sampling instants which are passed into the calculator from the model simulator.

5.2.3 Phase Lock Loop (PLL)

The PLL (Fig. 5.6) is composed of a low pass filter (LPF), a gain and a voltage controlled oscillator (VCO). The 3-phase voltages (v_{pa}, v_{pb}, v_{pc}) are first transformed into the stationary frame d-q components, and then, by applying a reference frame transformation, into the corresponding rotating frame counterparts, v_{pd} and v_{pq}. The latter appear as DC quantities in the respective frame and as such are easier to control. The reference frame transformation block receives the voltage phase angle from the 'VCO'. For a reference frame whose d-axis is aligned with the primary voltage, v_{pq} will be zero when the PLL is phase locked. Therefore, v_{pq} is used as a phase error signal. The error signal is low pass filtered and multiplied by a 'Gain'. The output from the 'Gain' is used to adjust the frequency of the 'VCO'. The 'VCO' is locked to the frequency of the incoming voltage when v_{pq}= 0. The frequency input to the 'VCO' is given a pre-set value of 50 Hz as this is the nominal frequency of the supply inputs. As the supply voltages are unlikely to deviate much from 50 Hz, a limiter is put on the frequency adjustment signal to limit its range. This adds to the stability of the PLL operation. The performance of the PLL can be tuned by changing the gain and the cut-off frequency of the 'LPF'. A 20 Hz cut-off frequency has been chosen for initial tests.

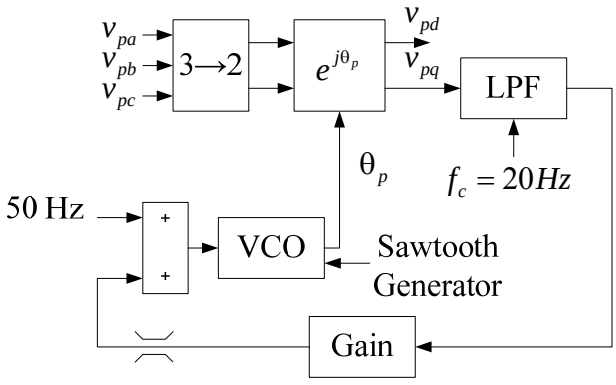

Figure 5.6: The PLL Diagram

5.2.4 Speed PI Controller

A simple speed (angular velocity) PI control algorithm is executed next in the main loop. It calculates the desired d component of the secondary current in the following control interval. A block diagram of the algorithm in discrete form is shown in Fig. 5.7. The PI controller is implemented with integrator anti-windup. The resultant unconstrained current is passed through a limiter to make sure that the machine is physically capable of developing the desired value. In addition to the current limiting function, the limiter also serves to avoid the integral windup by preventing the update of the integrator when saturation occurs. The difference equations that mathematically describe the algorithm in Fig. 5.7 are,

$$\begin{cases} x(n+1) = x(n) + G_i \Delta e(n+1) \\ i_{sd}^*(n) = G_p e(n) + x(n) \end{cases} \tag{5.2}$$

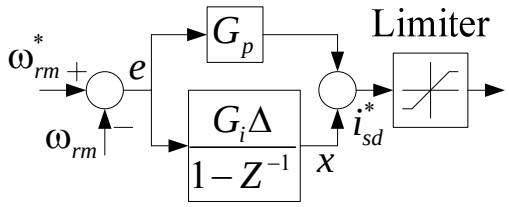

Figure 5.7: Angular Velocity PI Controller

5.2.5 Current PI Controller

The structure of the current controller consisting of two identical PI regulators with anti-windup (one for each reference frame axis) is presented in Fig. 5.8. The implemented PI algorithms are essentially the same as that in Fig. 5.7 for the speed control. The controller predicts the d-q components of the secondary voltage (v_{sd}^* and v_{sq}^*) on the BDFRM in the next control interval. These are then fed into a PWM generator after the inverse Park transformation. As can be seen from Fig. 5.8, the difference equations used to compute the unconstrained control voltages are:

$$\begin{cases} v_{sd}^*(n) = G_{d_p} e_d(n) + x_d(n) \\ v_{sq}^*(n) = G_{q_p} e_q(n) + x_q(n) \end{cases} \tag{5.3}$$

where G_{d_p} and G_{q_p} are constant proportional gains of the d-q regulators and $x_{d,q}$ represent the current status of the corresponding error integrators.

To ensure the resultant output voltage (v_{sd}^* and v_{sq}^*) to be applied to the BDFRM are physically realisable for a given inverter DC link voltage, v_{sd}^* and v_{sq}^* are passed through the limiters. The integrators are updated only if the voltages are within the range specified by the limits to prevent windup problems. Thus, their new values are:

$$\begin{cases} x_d(n+1) = x_d(n) + G_{d_i}\Delta e_d(n+1) \\ x_q(n+1) = x_q(n) + G_{q_i}\Delta e_q(n) \end{cases} \tag{5.4}$$

The integral gains G_{d_i} and G_{q_i} are also constant as are the proportional ones.

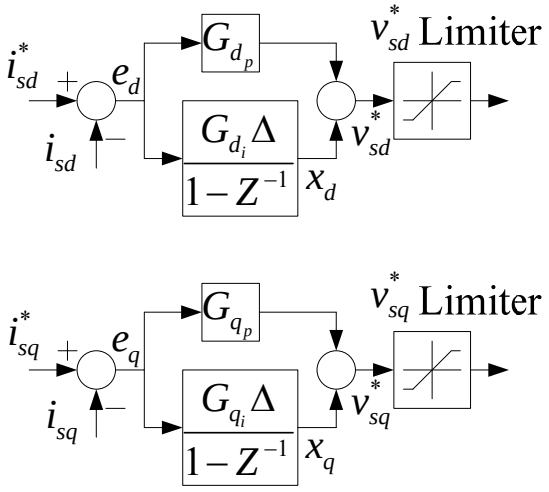

Figure 5.8: Block Diagram of a Current PI Controller in d-q Frame

5.2.6 Space Vector PWM Generator

The PWM generator implements a conventional PWM algorithm based on approximating a reference voltage space vector with the actual inverter voltage phasors shown in Fig. 5.9. Therefore, it accepts the required voltage inputs ($\underline{v}_s^*$) from the current controller and then works out the switching pattern of the inverter legs and

the times they have to be switched at so that the average voltage vector to be applied to the machine over the next control interval is the desired. In real-time, the values of the switching times would be programmed into timers that control the firing of inverter insulated gate bipolar transistors (IGBTs). [127]

There are several reasons that the space vector PWM technique is preferable to the traditional sinusoidal PWM. The main advantage is certainly the absence of the look-up tables with pre-stored firing patterns. The firing times of the inverter IGBTs are calculated on-line for each control interval, allowing changes to the output voltage to be simply implemented at the switching rate. It is thus more suitable for DSP implementation and requires less computational effort compared to the sinusoidal PWM. In addition, it offers higher maximum reference voltage and has lower harmonic content.

The states of the inverter legs that correspond to the vector positions in Fig. 5.9 are represented by binary bit patterns consisting of three bits (one for each phase) shown in the same figure. The order of the bits is that the most significant is for the phase-a leg, the middle one is for the phase-b leg and the least significant bit is for the phase-c leg. If the top device of the leg is on and the bottom one off, the relevant bit location is ‘1’. Otherwise i.e. for the opposite leg-state it is ‘0’. Obviously, there are six non-zero and two zero voltage vectors. The latter correspond to all the top switches on and bottom ones off (‘111’) and vice-versa (‘000’).

As can be seen from Fig. 5.9, the non-zero voltage vectors are displaced by 60^{o} and hence form six space sectors numbered from 0 to 5 in the counter-clockwise direction. It is assumed that the a-phase is aligned with the α-axis of the stationary α-β frame. Hence, the voltage vector ‘100’ has a zero angular position.

The basic layout of the overall PWM algorithm implemented is as follows [127]:

(1) Work out which sector the desired reference voltage vector lies in;

(2) Compute the application times for the voltage vectors bounding the sector to obtain the required average voltage vector;

(3) Determine the optimal sequence of the states of the inverter legs based on the switching times.

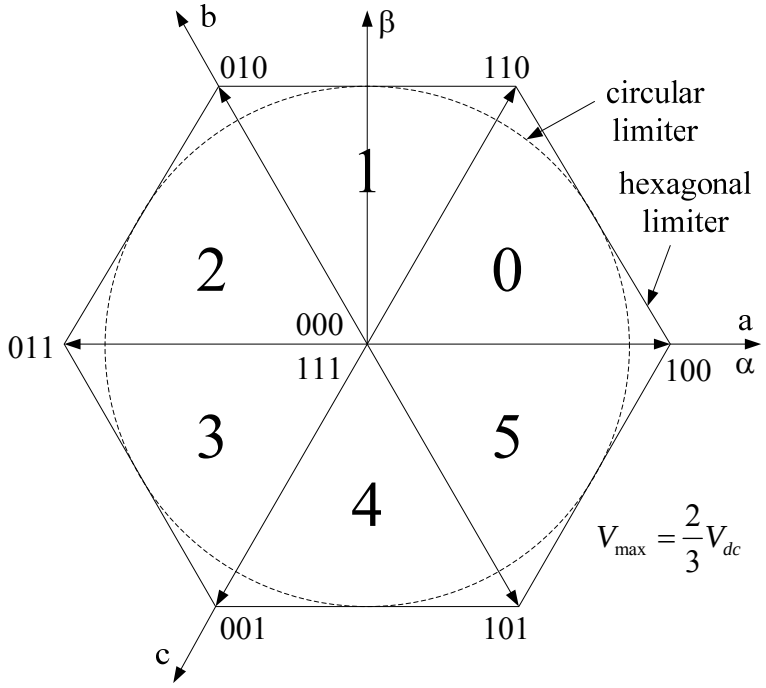

Figure 5.9: Inverter Voltage Vectors and Reference Voltage Limits

5.3 Vector Control of the Grid Side Converter (GSC)

The purpose of the Vector controlled GSC is to keep the DC link voltage fixed at a desired value and to maintain the q component of the line side current at zero to achieve the unity power factor on the line side. The simulation model has been built based on Fig. 4.2 using the parameters from Appendices A and B.

Fig. 5.10 shows the dynamic response of the torque controller (e.g. involving only the d-q current control loops) to a varying current reference from 0A to 2A. The d-q currents accurately follow the respective reference signals and there is no apparent

coupling between the two current components. Fig. 5.11 depicts the transient response with the outer loop V_{dc} control included. When a boost step change on V_{dc_ref} (from 250 V to 300 V) occurs at 0.05 s, the DC link voltage starts to track the desired trajectory within 0.01s due to a delayed action between the inner and outer vector control loops. Also, this transient depends on the size of the capacitor being deployed. Fig. 5.11 also includes the responding of I_{gd} and I_{gq} when the outer loop V_{dc} control applied. A huge transient of $I_{gd} - ref$ occurs between 0.05s until 0.06s that reflects the boosting up of V_{dc}. I_{gd} is attempting to achieve the desired value but influenced by the controller, so that it coincides to $I_{gd} - ref$ after 0.01s. $I_{gq} - ref$ is always set as 0 while I_{gq} also has a transient from 0.05s until 0.06s that shows the coupling effect between I_{gd} and I_{gq} when applying voltage oriented control. Since V_{dc_ref} is always set to a constant value during normal operation, the tracking performance of V_{dc} control is acceptable after tuning.

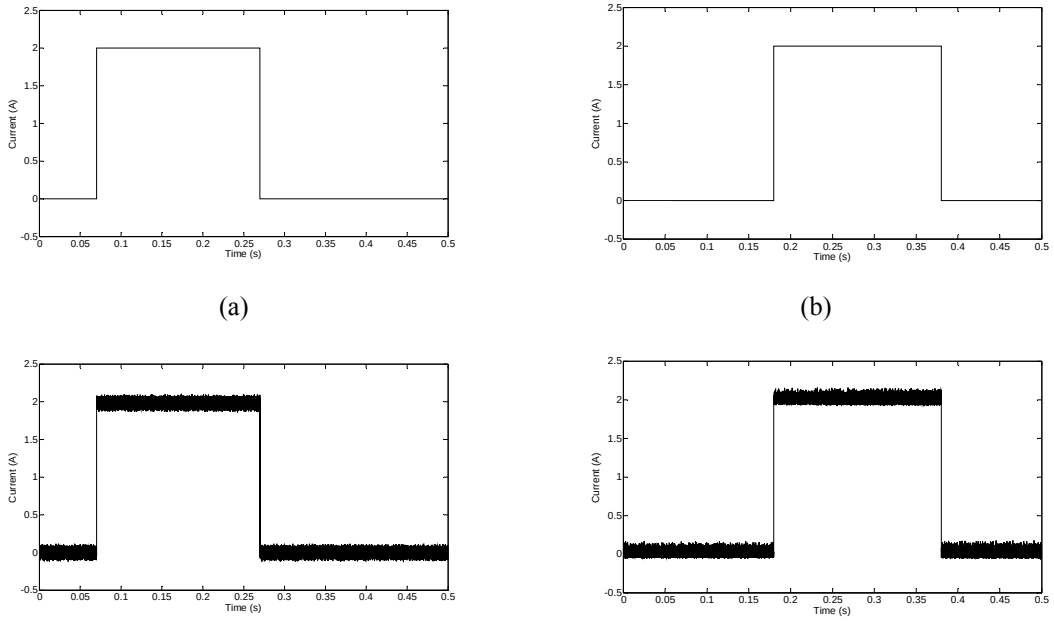

Figure 5.10: Current Control Performance of the GSC:

(a) $I_{gd} - ref$; (b) $I_{gq} - ref$; (c) I_{gd}; (d) I_{gq}

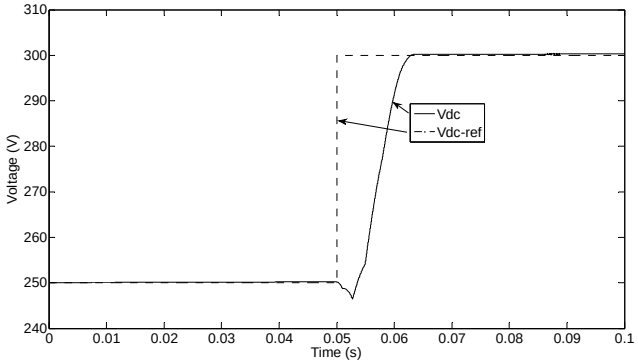

(a)

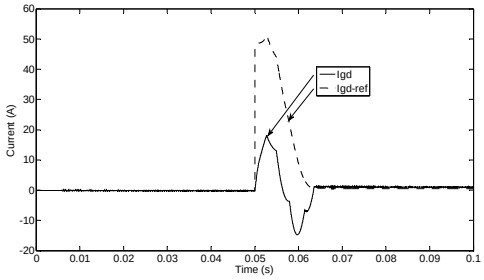

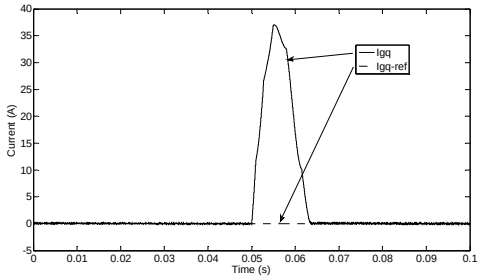

(b) (c)

Figure 5.11: V_{dc} Control Performance of the GSC:

(a) V_{dc} and $V_{dc}-\text{ref}$; (b) I_{gd} and $I_{gd}-\text{ref}$; (c) I_{gq} and $I_{gq}-\text{ref}$.

5.4 Vector Control of the MSC in Torque Mode

The MSC is controlled properly if good tracking performance of the d-q components of the rotor (DFIM) or secondary (BDFRM) current is achieved for the machine(s) operating with open-loop speed control in torque mode. Contrary to Fig. 5.5 conditions, there is no speed control but only current (inner loop) control. One of the input signals (T_l) has been consequently changed to an external speed signal to make sure the target machine is rotating at a constant speed. In reality, this would be equivalent to the speed control being the role of the prime-mover (e.g. a cage induction machine drive in our experimental systems) and not the test machine (DFIM or BDFRM).

The reference values of the d-q rotor/secondary side currents have been set as step changes to observe the dynamic response of the respective current control loops. The stator/primary power and current variations will also be monitored. The Figs. 5.12 and 5.13 demonstrate the dynamic performance of both the DFIM and the BDFRM running at super-synchronous speed (840 rpm).

Since the DFIM and the BDFRM are quite similar in modelling, let us choose the BDFRM as a case study to establish the relationships relevant for power calculations. Equation (3.36) can be rewritten as:

$$\begin{aligned} P_p + jQ_p &= \frac{3}{2}\mathbf{v_p i_p^*} \\ &= \frac{3}{2}\left(v_{pd} + jv_{pq}\right)\left(i_{pd} - ji_{pq}\right) \\ &= \frac{3}{2}\left[\left(v_{pd}i_{pd} + v_{pq}i_{pq}\right) + j(i_{pd}v_{pq} - i_{pq}v_{pd})\right] \end{aligned} \tag{5.5}$$

For the primary voltage oriented control frame, $v_{pq} = 0$ and $v_{pd} = v_p$. Hence, (5.5) could be simplified as:

$$P_p = \frac{3}{2}v_{pd}i_{pd} \tag{5.6}$$

$$Q_p = -\frac{3}{2}v_{pd}i_{pq} \tag{5.7}$$

where negative sign means generating while positive sign means absorbing. From (3.26) and (3.27), it can be derived that:

$$v_{pd} = R_p i_{pd} - \omega_p(L_p i_{pq} + L_m i_{sq}) \tag{5.8}$$

$$0 = R_p i_{pq} + \omega_p(L_p i_{pd} + L_m i_{sd}) \tag{5.9}$$

Assuming a large machine and neglecting R_p for convenience of the following qualitative analysis, (5.8) and (5.9) can be further simplified as:

$$v_{pd} \approx -\omega_p(L_p i_{pq} + L_m i_{sq}) \tag{5.10}$$

$$0 \approx \omega_p(L_p i_{pd} + L_m i_{sd}) \tag{5.11}$$

Therefore, given (5.6) and (5.7), P_p and Q_p are proportional to i_{pd} and $-i_{pq}$ respectively, while i_{pd} and i_{pq} are proportional to $-i_{sd}$ and $-i_{sq}$ respectively according to (5.10) and (5.11).

As can be seen from Fig. 5.12 (a) and (c), a step change (from 0 to 3 A) occurs on i_{rd_ref} at 0.65s and lasts for 0.2s with i_{rd} following the demand without any overshoot. Based on the previously established relationships between i_{rd}, i_{sd} and P_s, when i_{rd} is increasing, both i_{sd} and P_s are decreasing. Fig. 5.13 (e) and (f) plots the i_{rq} responses to a step change (from 0 to 3A) of i_{rq_ref} at 0.65s and sustained for 0.2s. The relationships between i_{rq}, i_{sq} and Q_s can also be verified from the same figure since when i_{sq} is increased, Q_s is decreased because of the decreasing i_{rq}.

i_{sd} and i_{sq} of the BDFRM also have good tracking performance as shown in Figs. 5.14 and 5.15 with the same changing tendency of i_{pd}, i_{pq}, P_p and Q_p compared with the DFIM. It can be observed that there is a good tracking of the desired current which demonstrates the effectiveness of the vector controller. The variations of the controlled current from the reference values can be reduced by alternating the PI gains of the current controllers. And both machines need certain reactive power to support the operation despite the motion conditions (sub-synchronous or super-synchronous, motoring or generating) if there are no control loops for the power. Some differences between Figs. 5.12 and 5.13 to Figs. 5.14 and 5.15 in magnitude aspect exist due to the differences between two machines. The coupling effects of presence of the back-EMF components also appear in Figs. 5.12 - 5.15.

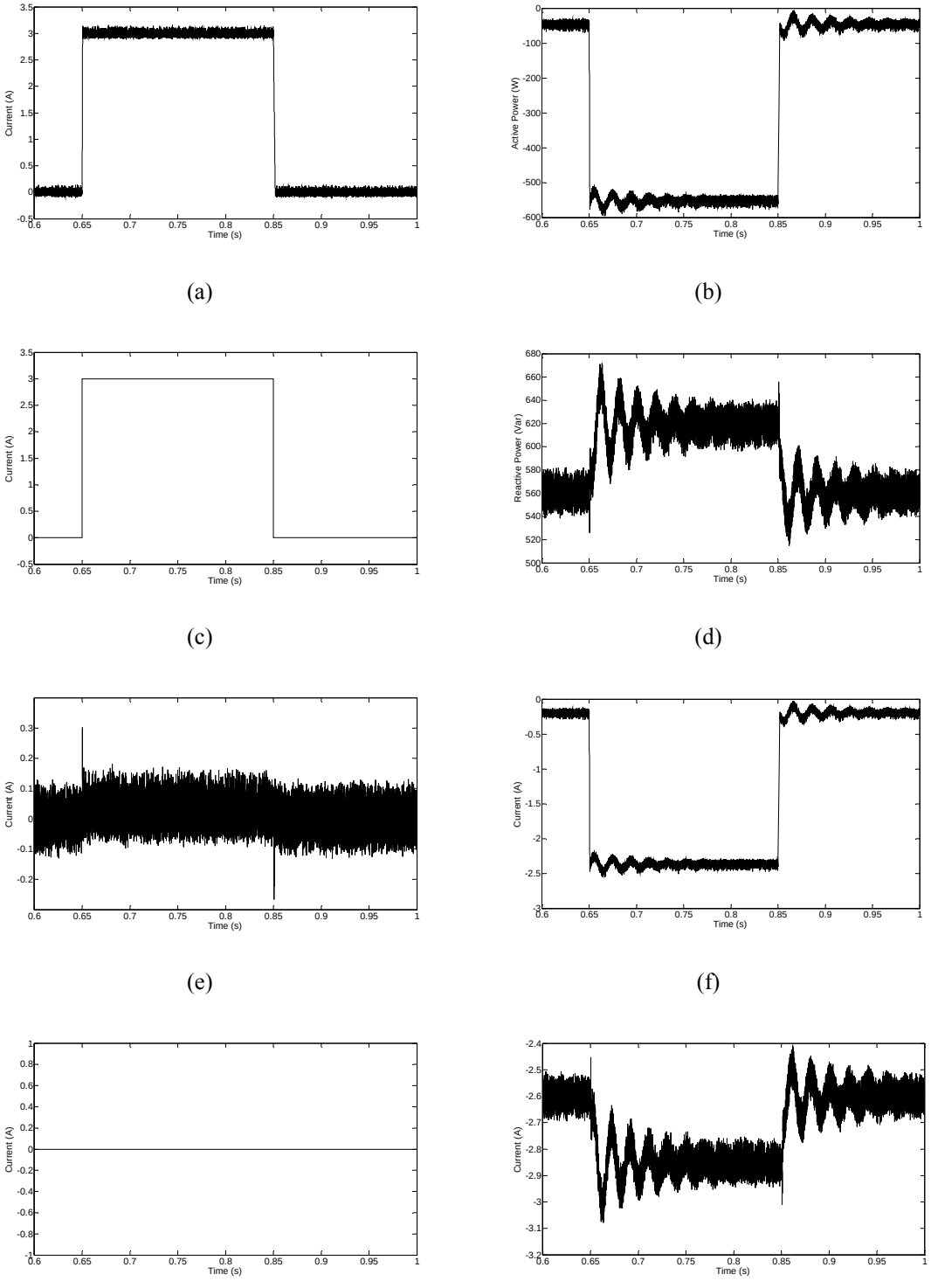

Figure 5.12: DFIM Vector Control Performance in Torque Mode of the MSC with Variation on i_{rd}: d-q Rotor Currents with Referenced Values, Stator Active and Reactive Power, d-q Stator Currents. (a) i_{rd}; (b) P_s; (c) $i_{rd} - ref$; (d) Q_s; (e) i_{rq}; (f) i_{sd}; (g) $i_{rq} - ref$; (h) i_{sq}.

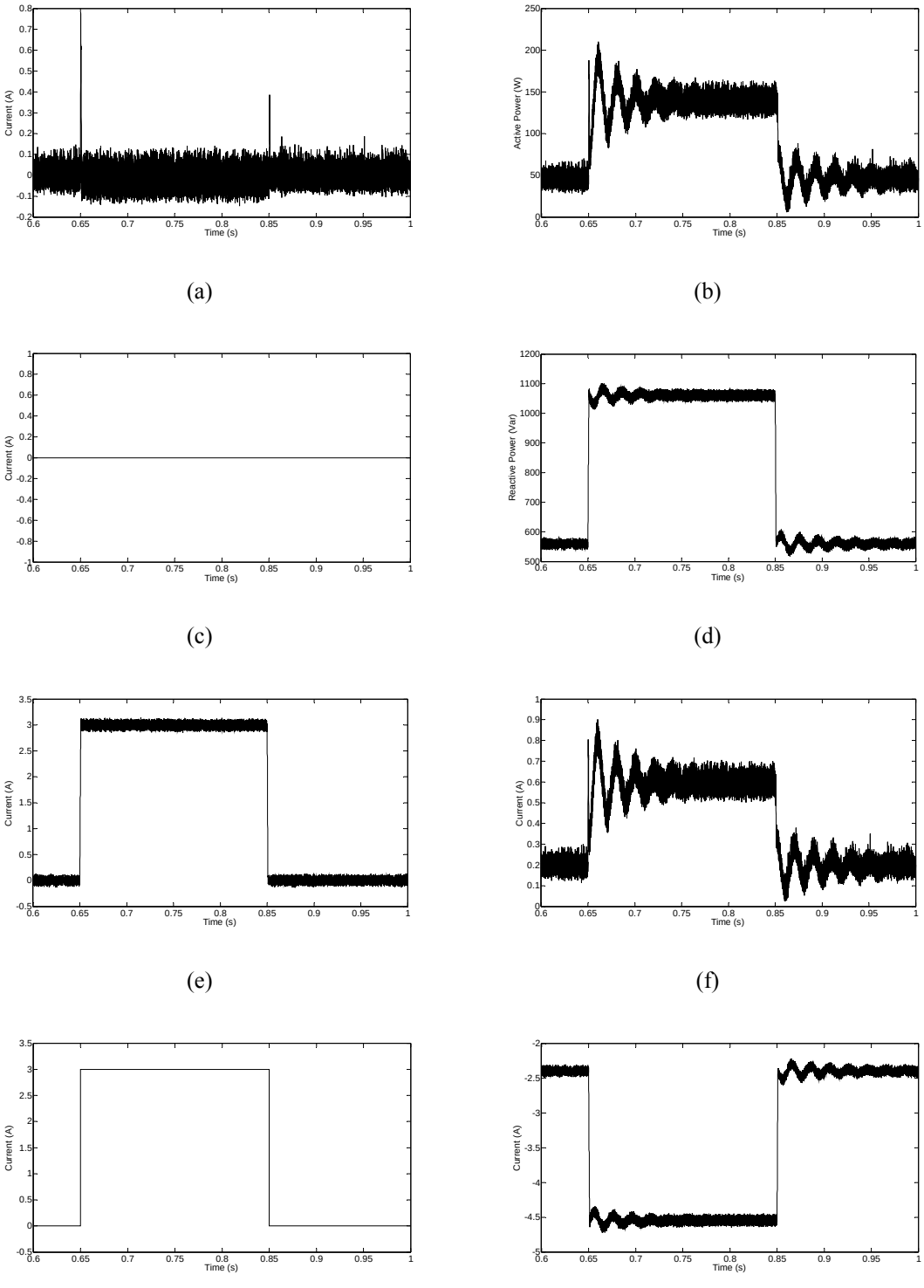

(a) (b)

(c) (d)

(e) (f)

(g) (h)

Figure 5.13: DFIM Vector Control Performance in Torque Mode of the MSC with Variation on i_{rq}: d-q Rotor Currents with Referenced Values, Stator Active and Reactive Power, d-q Stator Currents. (a) i_{rd}; (b) P_s; (c) $i_{rd} - ref$; (d) Q_s; (e) i_{rq}; (f) i_{sd}; (g) $i_{rq} - ref$; (h) i_{sq}.

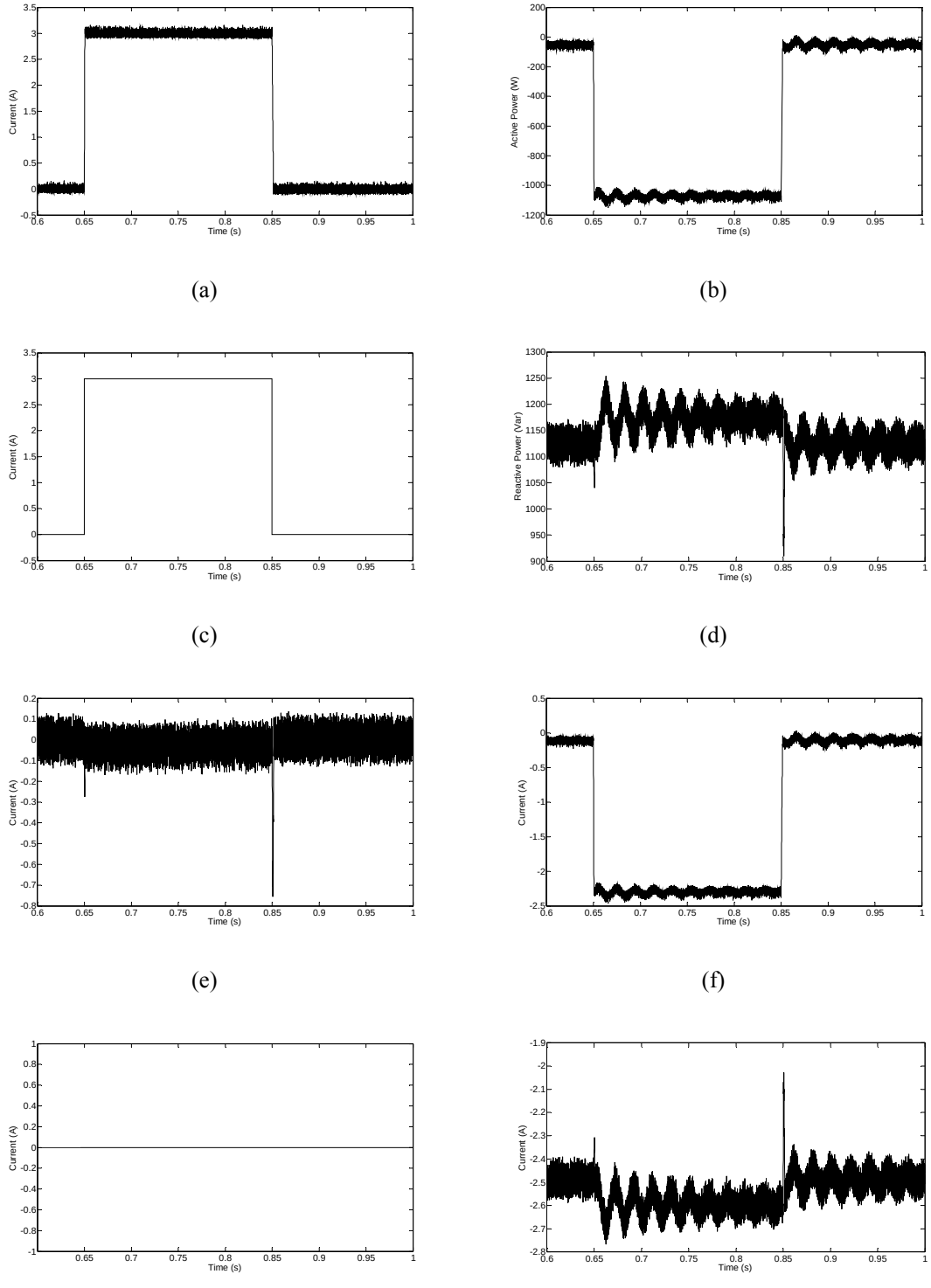

Figure 5.14: BDFRM Vector Control Performance in Torque Mode of the MSC with Variation on i_{sd}: d-q Secondary Currents with Referenced Values, Primary Active and Reactive Power, d-q Primary Currents. (a) i_{sd}; (b) P_p; (c) $i_{sd} - ref$; (d) Q_p; (e) i_{sq}; (f) i_{pd}; (g) $i_{sq} - ref$; (h) i_{pq}.

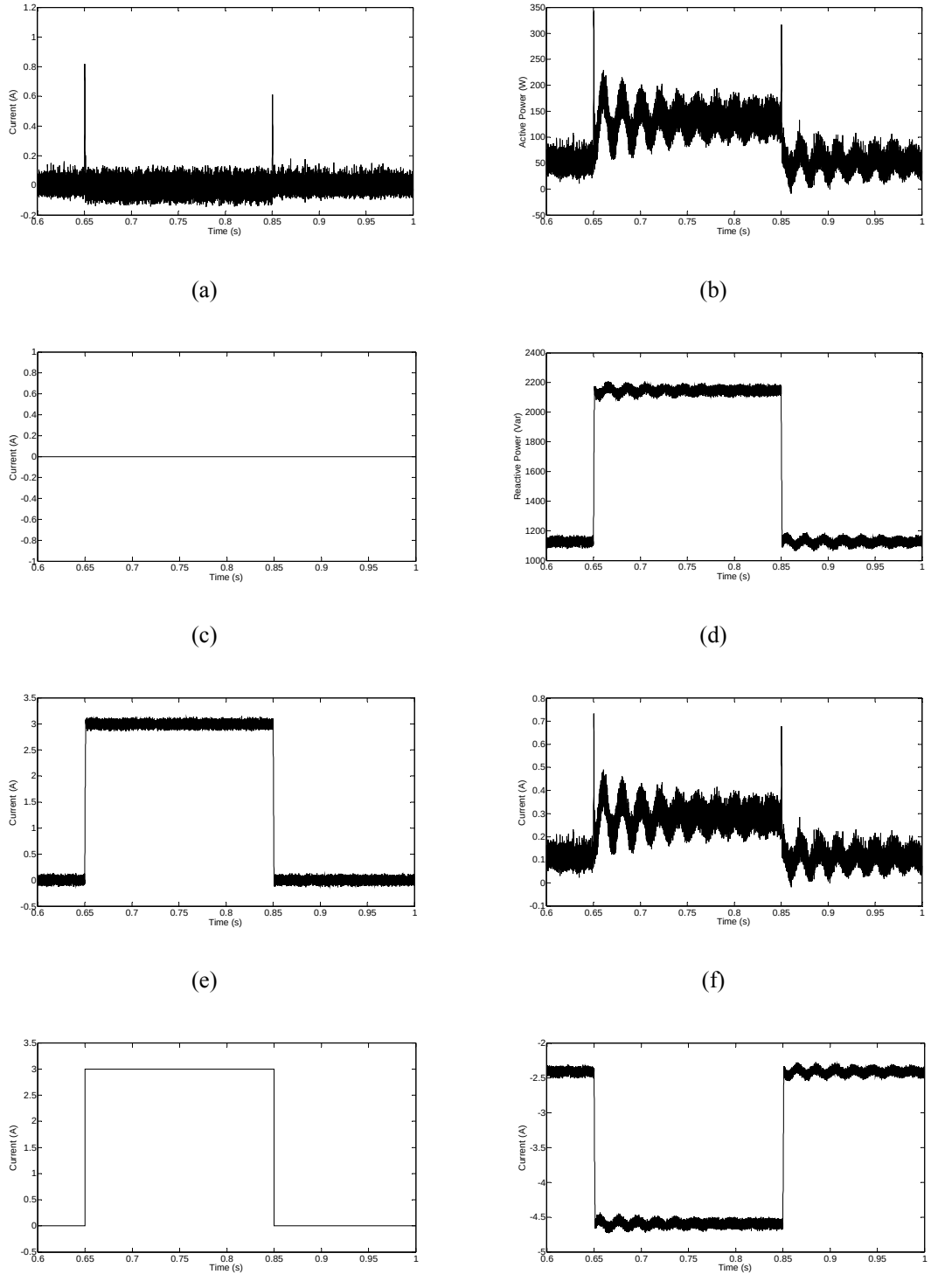

Figure 5.15: BDFRM Vector Control Performance in Torque Mode of the MSC with Variation on i_{sq}: d-q Secondary Currents with Referenced Values, Primary Active and Reactive Power, d-q Primary Currents. (a) i_{sd}; (b) P_p; (c) $i_{sd} - ref$; (d) Q_p; (e) i_{sq}; (f) i_{pd}; (g) $i_{sq} - ref$; (h) i_{pq}.

5.5 Vector Control of the MSC in Speed Mode

The simulation results are generated using the VC scheme in Fig. 5.5 (both the speed and q-axis rotor/secondary current control), including the power electronics models, for variable speed operation of the DFIM and/or the BDFRM. The reference speed profile consists of synchronous (750 rpm), super-synchronous (840 rpm) and sub-synchronous mode (660 rpm) with the load torque suddenly varying between 0, 10 Nm and -10 Nm to examine both the motoring and generating regimes of the machine(s) in a typical speed range for the target applications and under different loading conditions. Various performance indicators under the closed-loop speed control of the DFIM and the BDFRM are shown in Figs. 5.16 and 5.17 respectively.

Figs. 5.16 and 5.17 show the speed tracking performance of the DFIM and the BDFRM with small speed difference when sudden load disturbance at sub-synchronous, synchronous and super-synchronous speeds. Current limiter (-30A to 30A) has been applied to protect transducers and all the other instruments away from over current rating issues. The torque being negative means that the machine is effectively in the generating mode as confirmed by the primary active power waveforms.

Since the relationships between the stator/primary side power, stator/primary side current and rotor/secondary side current have been discussed in the previous section, the same conclusions made there can be carried over in the situations considered here. Inside the results of the DFIM, reactive power keeps constant in due to perfect decoupled control of i_{rd} which also makes i_{sq} invariant in consequence. But when in the BDFRM, transient conditions occurred on Q_p and i_{pq} inside Fig. 5.17 (b) and (d) because of slightly coupling effect between i_{sd} and i_{sq}.

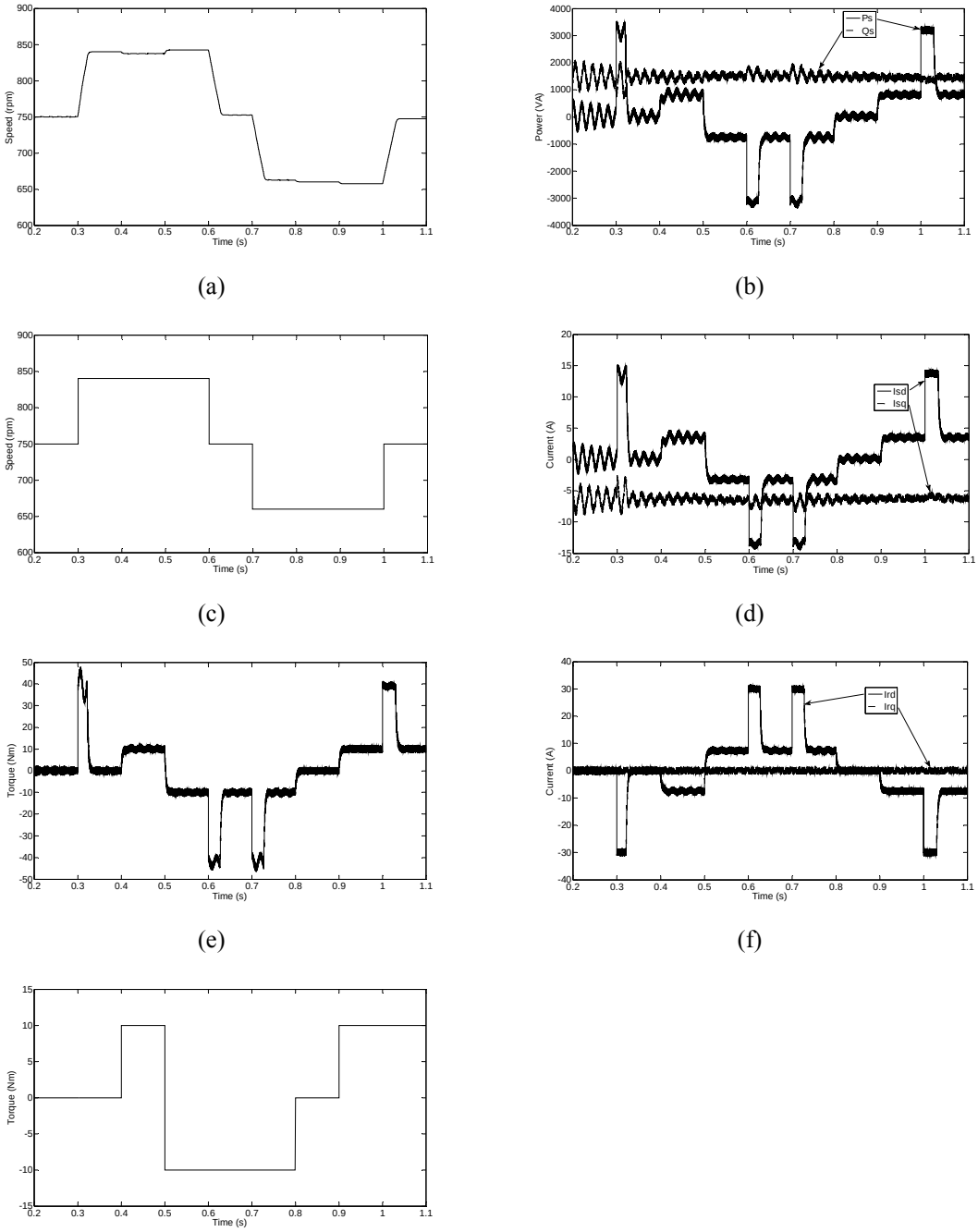

Figure 5.16: DFIM Vector Control Performance in Speed Mode of the MSC for: Rotating Speed with Referenced Values, Electromagnetic Torque and Load Torque, Stator Active and Reactive Power, d-q Stator Currents, d-q Rotor Currents. (a) n_{rm}; (b) P_s and Q_s; (c) $n_{rm} - ref$; (d) I_{sd} and I_{sq}; (e) T_e; (f) I_{rd} and I_{rq}; (g) T_l

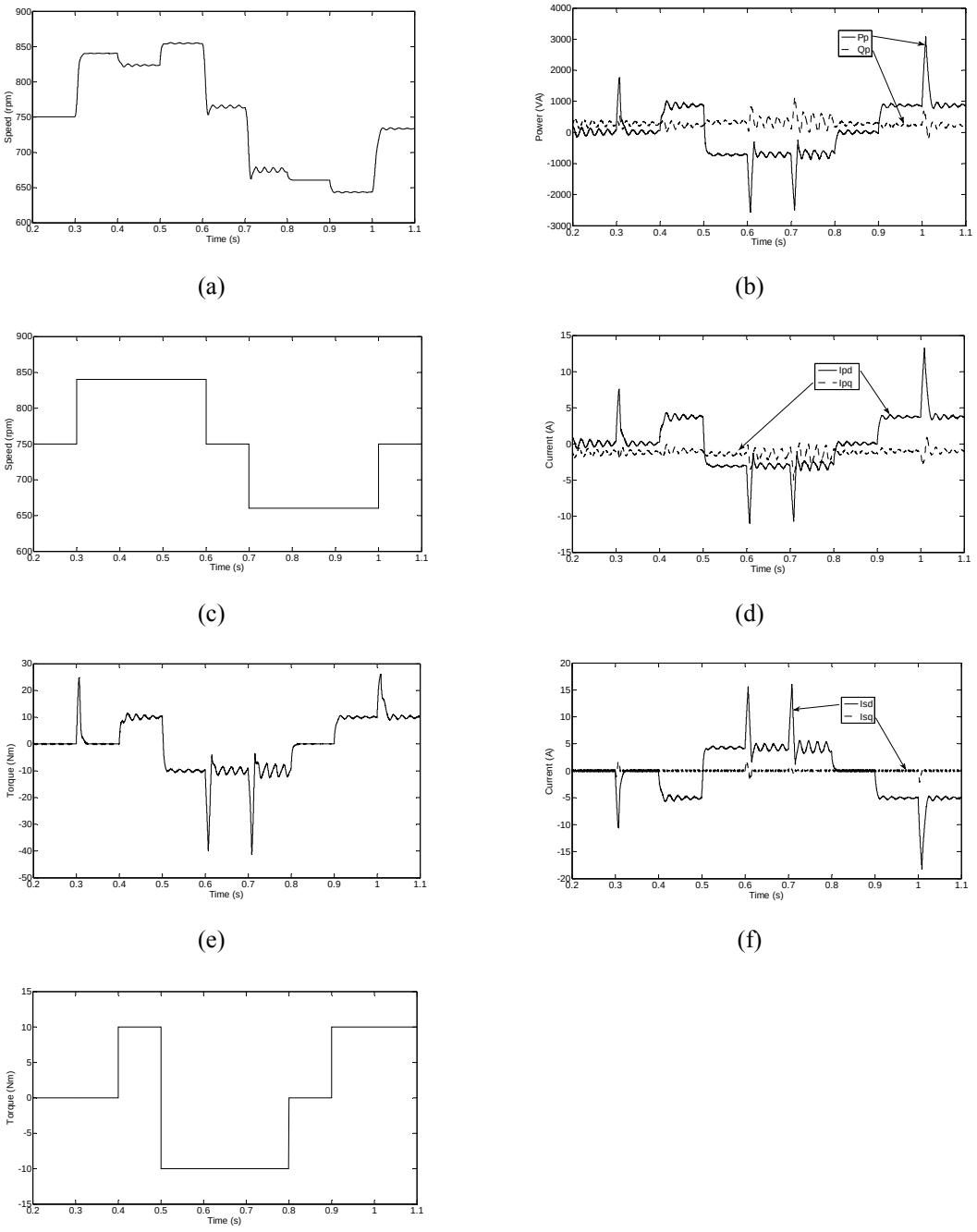

Figure 5.17: BDFRM Vector Control Performance in Speed Mode of the MSC for: Rotating Speed with Referenced Values, Electromagnetic Torque and Load Torque, Primary Active and Reactive Power, d-q Primary Currents, d-q Secondary Currents. (a) n_{rm}; (b) P_p and Q_p; (c) $n_{rm} - ref$; (d) I_{pd} and I_{pq}; (e) T_e; (f) I_{sd} and I_{sq}; (g) T_l

5.6 Conclusions

A comprehensive set of computer simulation studies have been carried out to evaluate the performance of a stator/primary voltage oriented vector controller for the DFIM and the BDFRM. The simulation program and its main functions have been described in detail with the controller based on the conventional machine discrete d-q model.

Plots of the performance of the MSC employed by both the DFIM and the BDFRM in open loop and close loop speed control applying with a controllable load are shown and discussed. Performance of the vector controlled GSC is also displayed. In order to emulate the real system, the control frequency and current sampling rate are set to be exactly the same as in the real-time controller. The significant conclusions that can be drawn from the results are as follows.

(1) VC is working properly on the GSC with relation to control of the DC link voltage and q component of the line side current. V_{dc} could follow the reference value within 0.01s while i_{gq}'s tracking interval is negligible.

(2) The actual d-q components of the rotor/secondary side current accurately track the desired trajectories with small coupling effect on the stator/primary side power and stator/primary side current due to existence of stator/primary resistance in open loop speed control scheme.

(3) The controller has excellent speed performance in close loop speed control method with electromagnetic torque and q component of the rotor/secondary side current exactly following the load torque and the reference value respectively at steady state.

The general conclusion that can be made from the simulation studies is that the developed vector controller is very effective and has high performance and accuracy with stator/primary voltage oriented control scheme. This argues well for a real-time

implementation of the controller. Since they are the provisional results from the simulation models using parameters measured in the lab, further results achieved from the experiments will be shown in the next chapter.

6. Experimental Results

6.1 Introduction

The simulation results of the previous chapter have demonstrated the high 'theoretical' performance of the vector controller. This is certainly an important and necessary preliminary step before the control implementation on the machine itself.

However, some significant modifications have to be made to adapt the simulation programme for real-time use. Due to noise issues associated with the interface board of the eZdsp implementation of the controller and some Electro-Magnetic Interference (EMI) inside the control cabinet, the supply voltages on both the stator/primary and grid side have been narrowed down to 190V (line-to-line) during the whole testing procedure to prevent nuisance tripping of protection circuitry and avoid potential damage on the IGBT modules. Also, for the scope of this thesis, the IM drive has been only operated in speed mode with the primary objective to test the torque/power control performance of the DFIM/BDFRM. So, the experiments have been done at sub-synchronous (660 rpm), synchronous (750 rpm) and super-synchronous (840 rpm) speeds for performance comparison of the machines where the speed control has been achieved within the IM drive rather than the test machines themselves. The space vector PWM carrier frequency has been set to 5 kHz which is the same as simulation models, with a DC link referenced voltage as 300V.

In order to verify the results of the simulation studies of Chapter 5, the experiments have been carried out in the lab using TMS320F28335 DSP based eZdsp development board with C++ programming implemented to control two test rigs separately, one for a 6.75 kW DFIM, and the other with a 4 kW BDFRM, both driven by commercial 4-quadrant 11 kW IM drives (see Appendices A and B). All the codes are developed using the compiling software 'CCS' from Texas Instruments and loaded to the

Labview® control interface from National Instruments on the control PC. Some important codes have been listed in Appendix C. The control panel after initialisation is shown in Fig. 6.1. A detailed description of the test system hardware can be found in Appendices A and B.

The good performance of the controller simulators on both GSC and MSC demonstrated in Chapter 5 are partially experimentally verified by the results presented in Sections 6.2-6.4. The last section of the chapter is a summary of the relevant conclusions/observations that can be made from these experimental results.

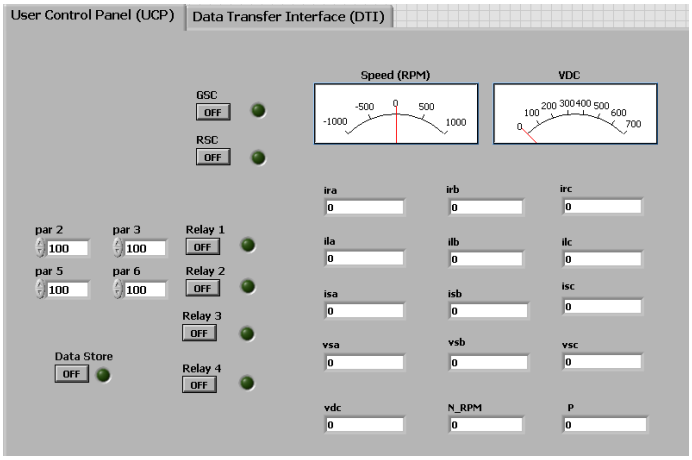

Figure 6.1: User Control Panel on Labview®

6.2 Performance of GSC Vector Control

As mentioned earlier, the function of the Grid Side Converter (GSC) is to control the DC link voltage to a desired value and q component of the grid side current to zero for unity power factor conditions on the grid side by applying stator/primary voltage oriented control. Dynamic performance of inner loop d-q control of grid side current will be displayed here. The performance of outer DC link voltage control loop will be depicted in the next section. Figs. 6.2 and 6.3 clearly show that both the d and q components of the grid side current are tracking the step changes from 0 to 2A accurately and without any overshoot or phase delays.

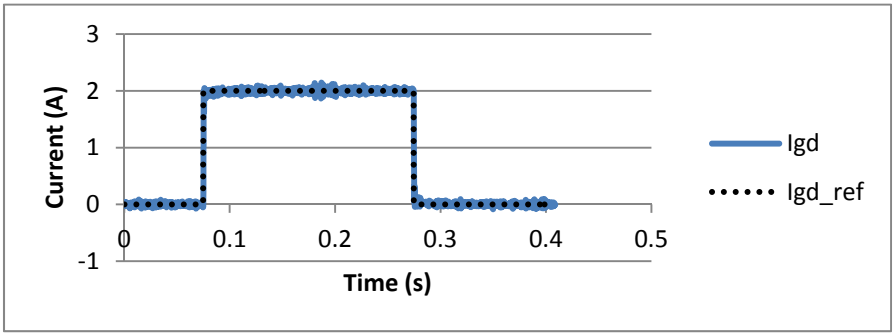

Figure 6.2: Vector Control Performance of Grid Side d-axis Current

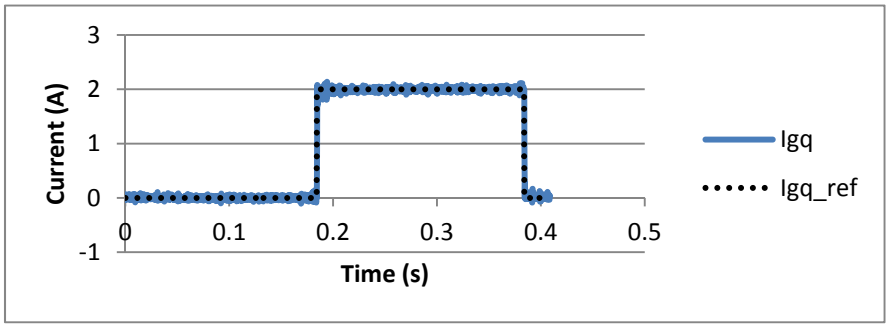

Figure 6.3: Vector Control Performance of Grid Side q-axis Current

6.3 Vector Control of MSC and GSC in Torque Mode

The MSC and GSC are controlled properly if good tracking of the reference trajectories for d-q rotor (DFIM) or secondary (BDFRM) currents, DC link voltage, and q-axis grid side current is achieved for the machine(s) operating with open-loop speed control (i.e. in torque mode). Since the supply voltages on both the machine sides have been set to 190V (line-to-line) during the experiment, the DC link voltage and q component of the grid side current are initially controlled at 300V and 0A respectively after enabling the GSC. Vector control of the MSC is then activated to make sure that the d-q rotor/secondary currents accurately follow their reference values.

6.3.1 Vector Control Performance of MSC

The reference values for the d and q components of the rotor (DFIM)/secondary (BDFRM) current have been set with a step change included to observe the dynamic

performance of the MSC controller on the DFIM and the BDFRM test rigs. Since the rotor/secondary side current, the consequent stator/primary side power and stator/primary side current do not change at different rotating speed, the figures (Figs. 6.4-6.7) will only demonstrate the dynamic performance at super-synchronous speed (840 rpm) of the DFIM (Figs. 6.4 and 6.5) and the BDFRM (Figs. 6.6 and 6.7) operating as generators as indicated by the active power flow to the grid on the stator/primary side (Figs. 6.4-6.7). Fig. 6.4 shows the DFIM response to a step change (from 0A to 3A) in i_{rd}^{*} applied at 0.1s for i_{rq}^{*} = 0A. It can be seen that i_{rd} follows well the reference values with i_{sd} and P_s varying in a similar manner as expected given the conclusions in Section 5.4. Similar observations can be made about the i_{sq} and Q_s waveforms. Fig. 6.5 proves that the rotor side q-axis current is controlled properly with a step change (from 0A to 3A) of the desired value occurring at 0.1 s. There are also notable coupling effects shown on the respective i_{sd}/P_s and i_{sq}/Q_s plots in the same figures. Although vector control of the secondary current of the BDFRM works well according to Figs. 6.6 and 6.7, the variation of the primary side current and power appears to be higher than in the DFIM's case.

The simulation results presented in Section 5.3 and 5.4 have been experimentally validated here having the same operation conditions in rotating speed, current references, grid voltage, space vector PWM frequency and parameters of the controller etc. Due to the different recording methods, the starting points of each group of figures accordingly are not the same, but with the same duration of period. After comparing the simulation with the according experimental results, controlled variables are tracking the referenced values in very fast response with no overshoot. Also, the variables accordingly are altering in the same trends but with some difference in magnitude due to the inaccuracy of off-line testing of machine parameters and some noise issues during the experiment.

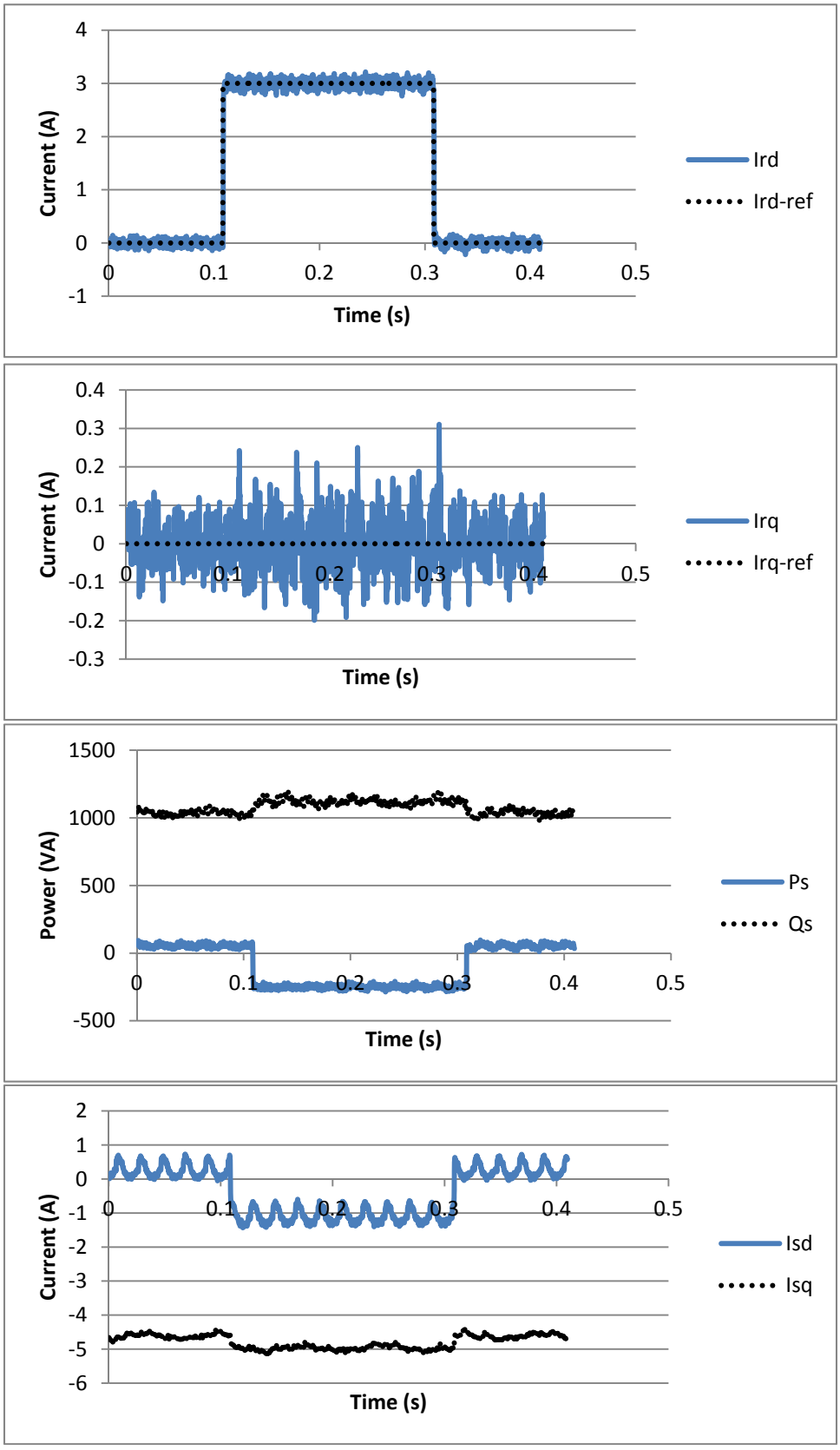

Figure 6.4: Dynamic Performance of Vector Controlled MSC on the DFIM with a Step Change on d Component of Rotor Current, and with Stator Power and Stator Current Responses

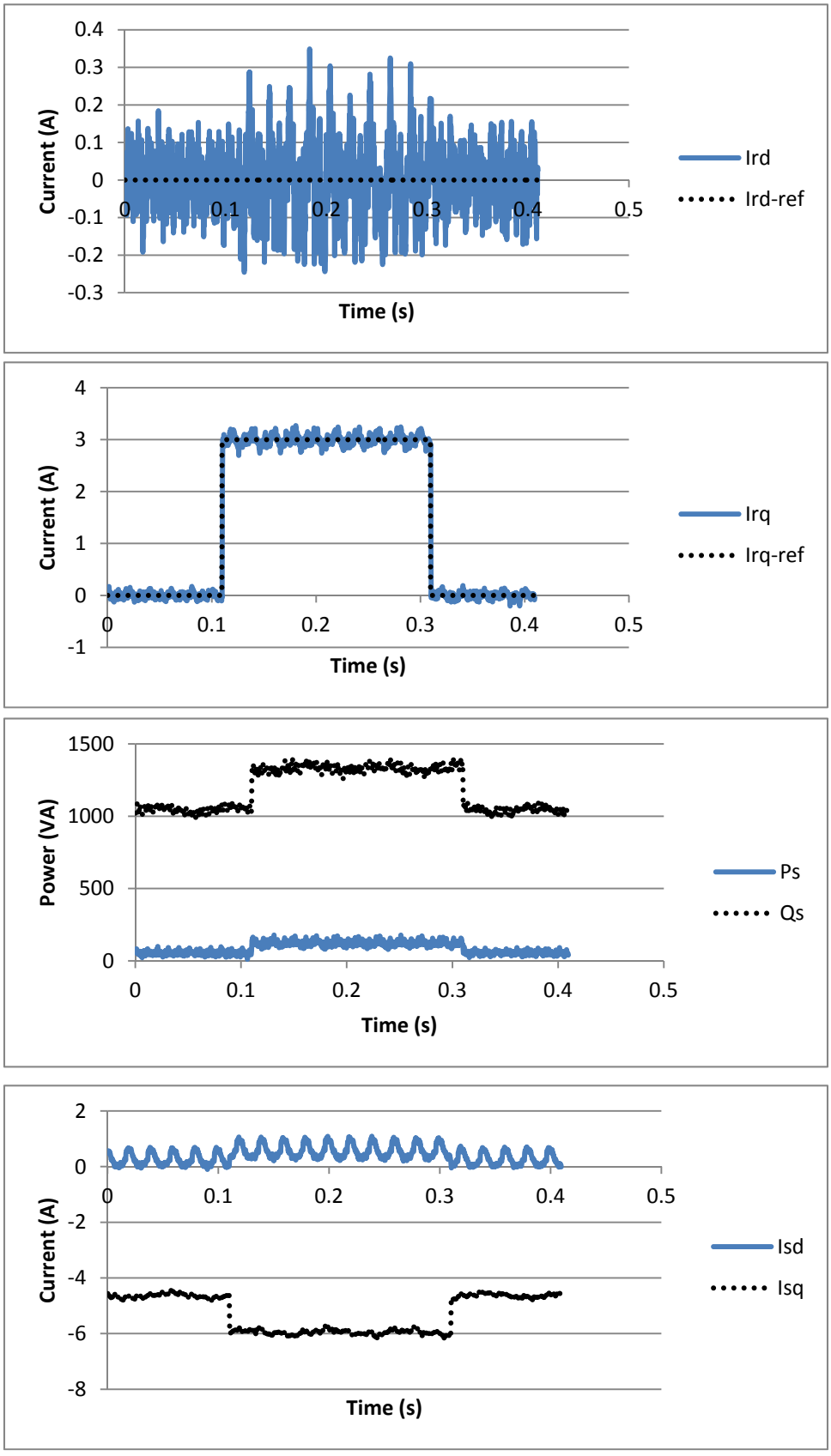

Figure 6.5: Dynamic Performance of Vector Controlled MSC on the DFIM with a Step Change on q Component of Rotor Current, and with Stator Power and Stator Current Responses

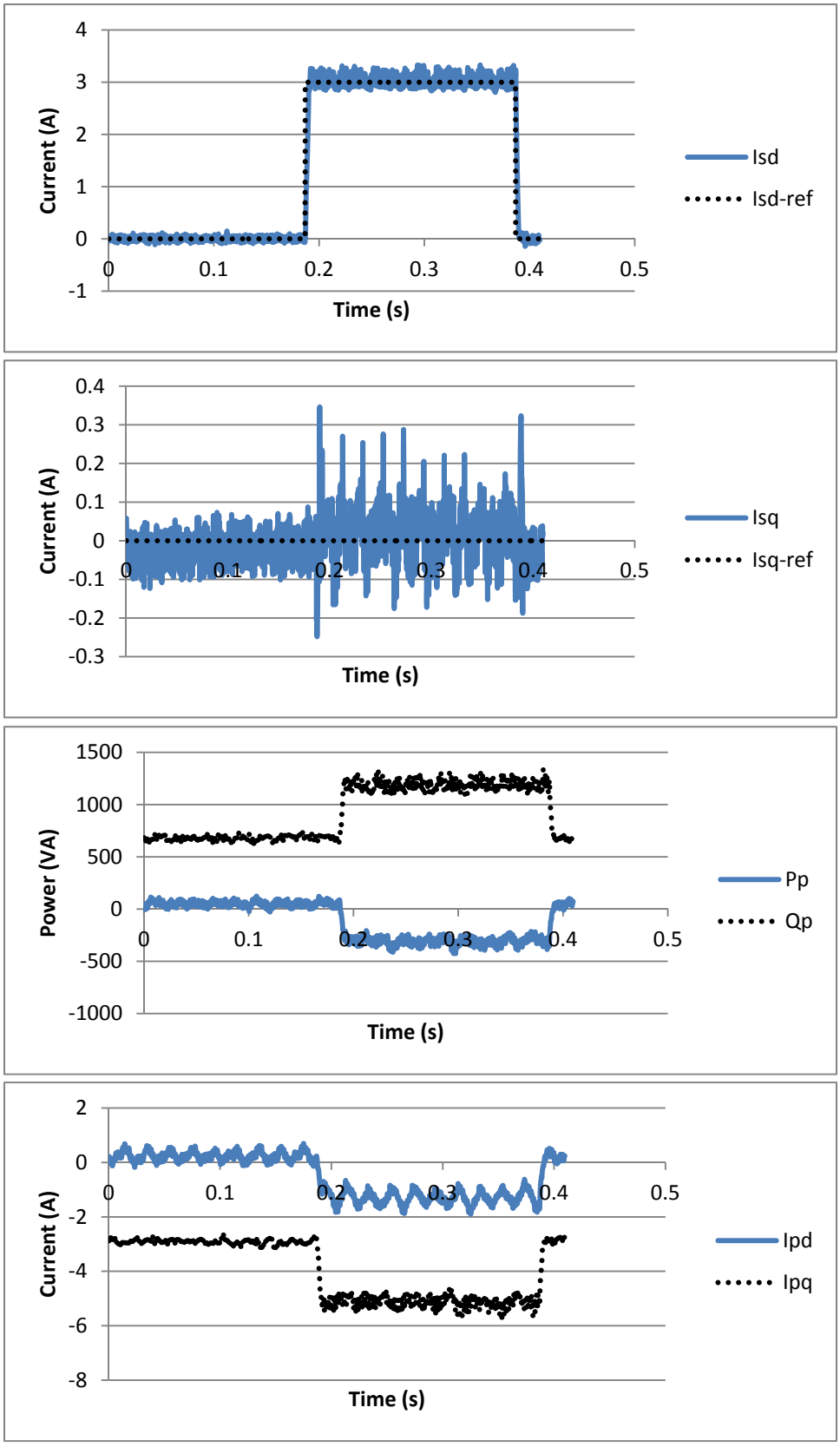

Figure 6.6: Dynamic Performance of Vector Controlled MSC on the BDFRM with a Step Change on d Component of Secondary Current, and with Primary Power and Primary Current Responses

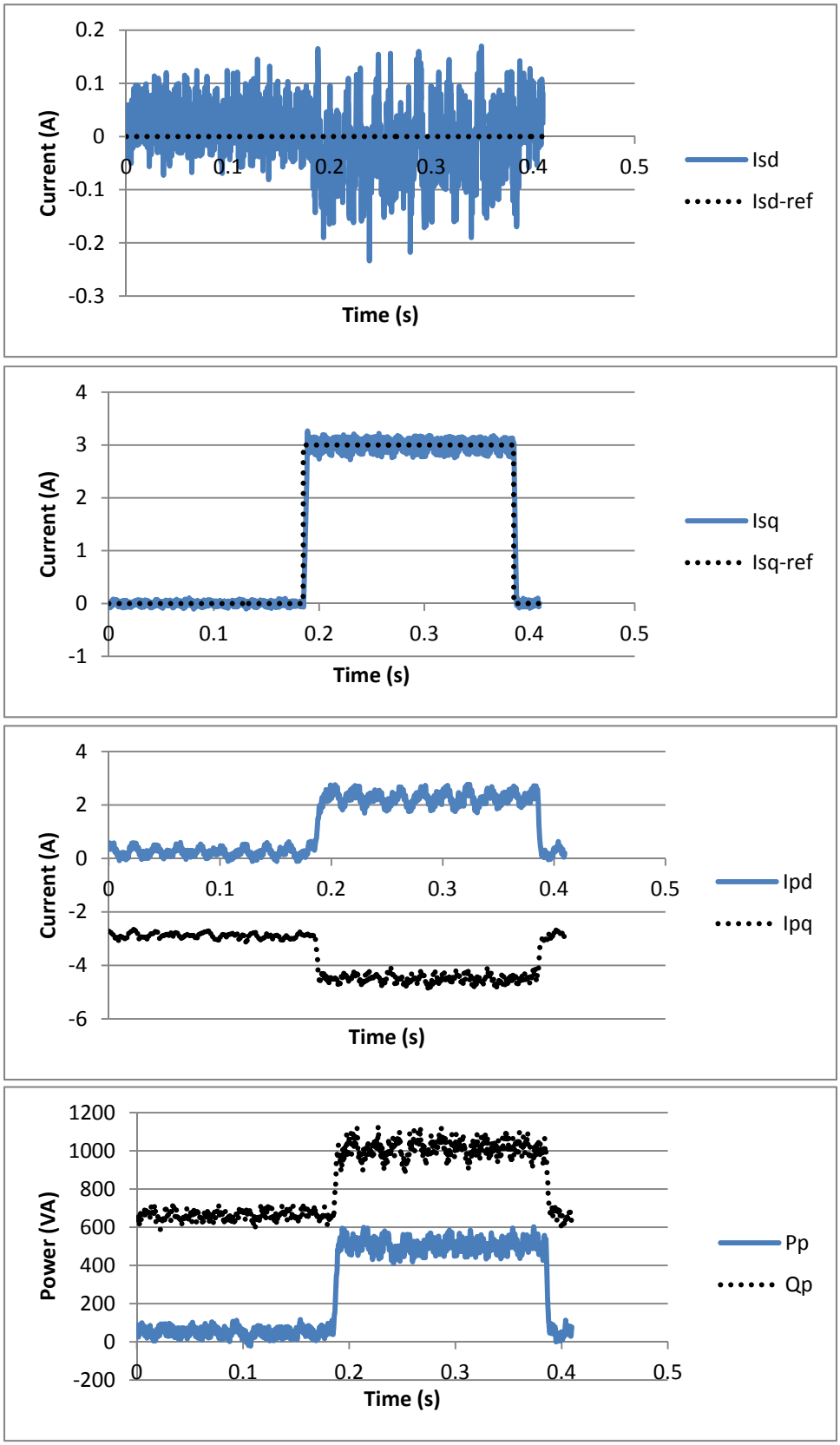

Figure 6.7: Dynamic Performance of Vector Controlled MSC on the BDFRM with a Step Change on q Component of Secondary Current, and with Primary Power and Primary Current Responses

6.3.2 Vector Control of MSC and GSC - Power Analysis

References for the rotor (DFIM)/secondary (BDFRM) d-q current components have been set as constant values to perform and evaluate torque control of the DFIM and the BDFRM (Fig. 6.8). These are appropriately chosen to prevent over current on both the rotor/secondary and stator (DFIM)/primary (BDFRM) side, and to make sure that the machines operate as generators in most cases. The shaft speed is controlled at desired values by the prime mover (i.e. IM drive) in either the sub-synchronous, synchronous or super-synchronous mode of the machines.

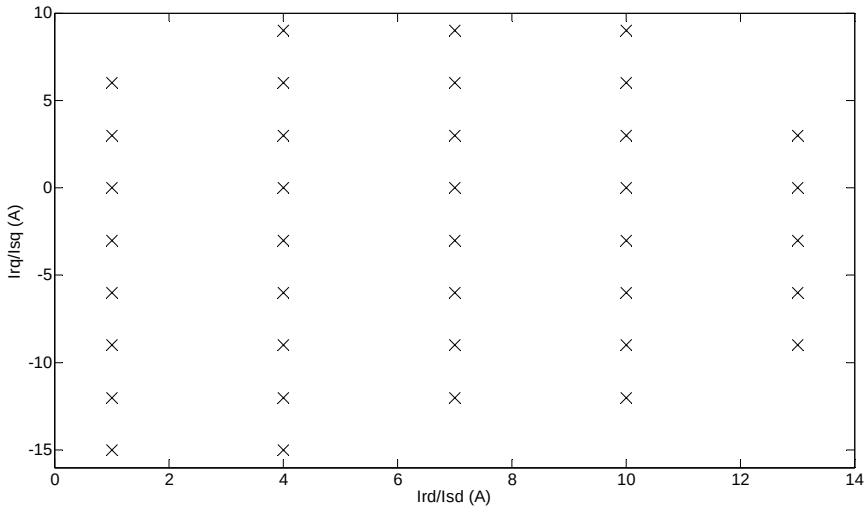

Figure 6.8: Reference d-q Rotor (DFIM)/Secondary (BDFRM) Currents

The control performance of the d-q rotor/secondary currents, q-axis grid side current and DC link voltage of the DFIM and the BDFRM is displayed in Figs. 6.9-6.12. The corresponding stator/primary side power and net power (after considering the power generated/absorbed on the grid side of the control windings) plots appear in Figs. 6.13 and 6.14. The experimental results have only been shown for the super-synchronous speed operation as they are very similar in the other two speed modes of the machines.

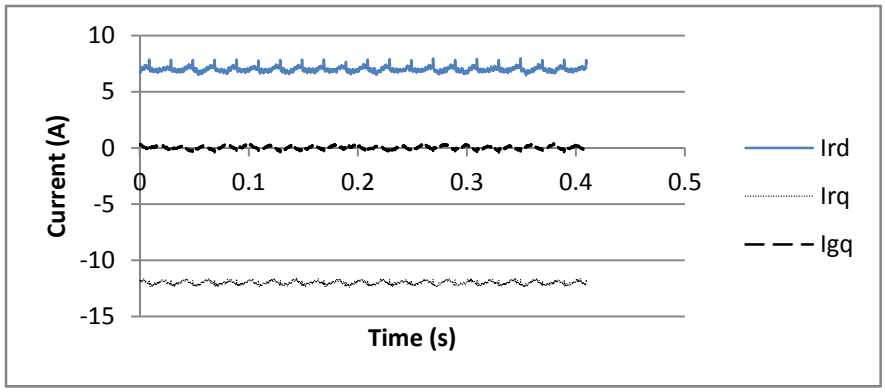

Figure 6.9: DFIM Vector Control Performance: The Rotor and Grid Currents

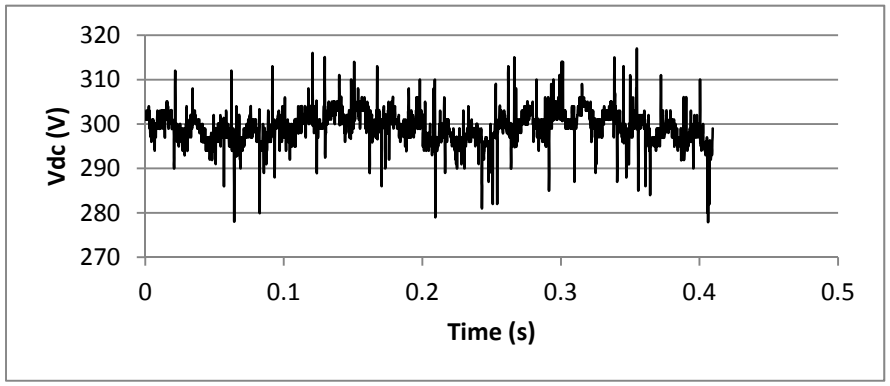

Figure 6.10: DC Link Voltage of the DFIM

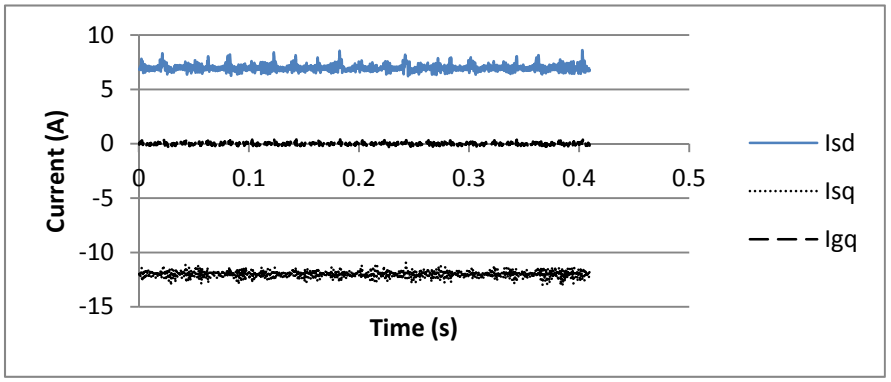

Figure 6.11: BDFRM Vector Control Performance: The Secondary and Grid Currents

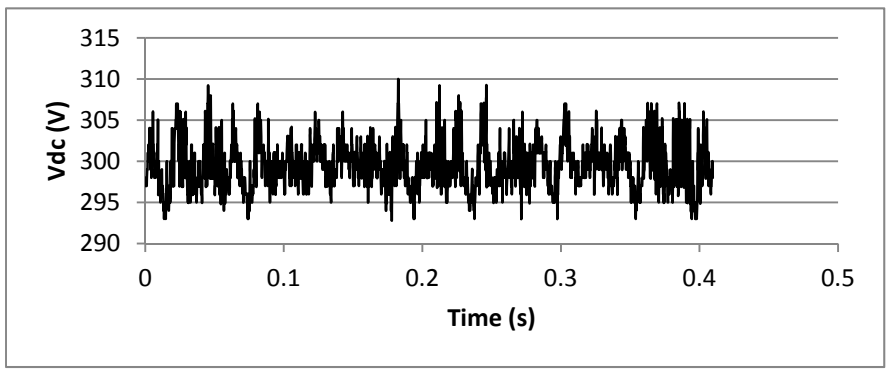

Figure 6.12: DC Link Voltage of the BDFRM

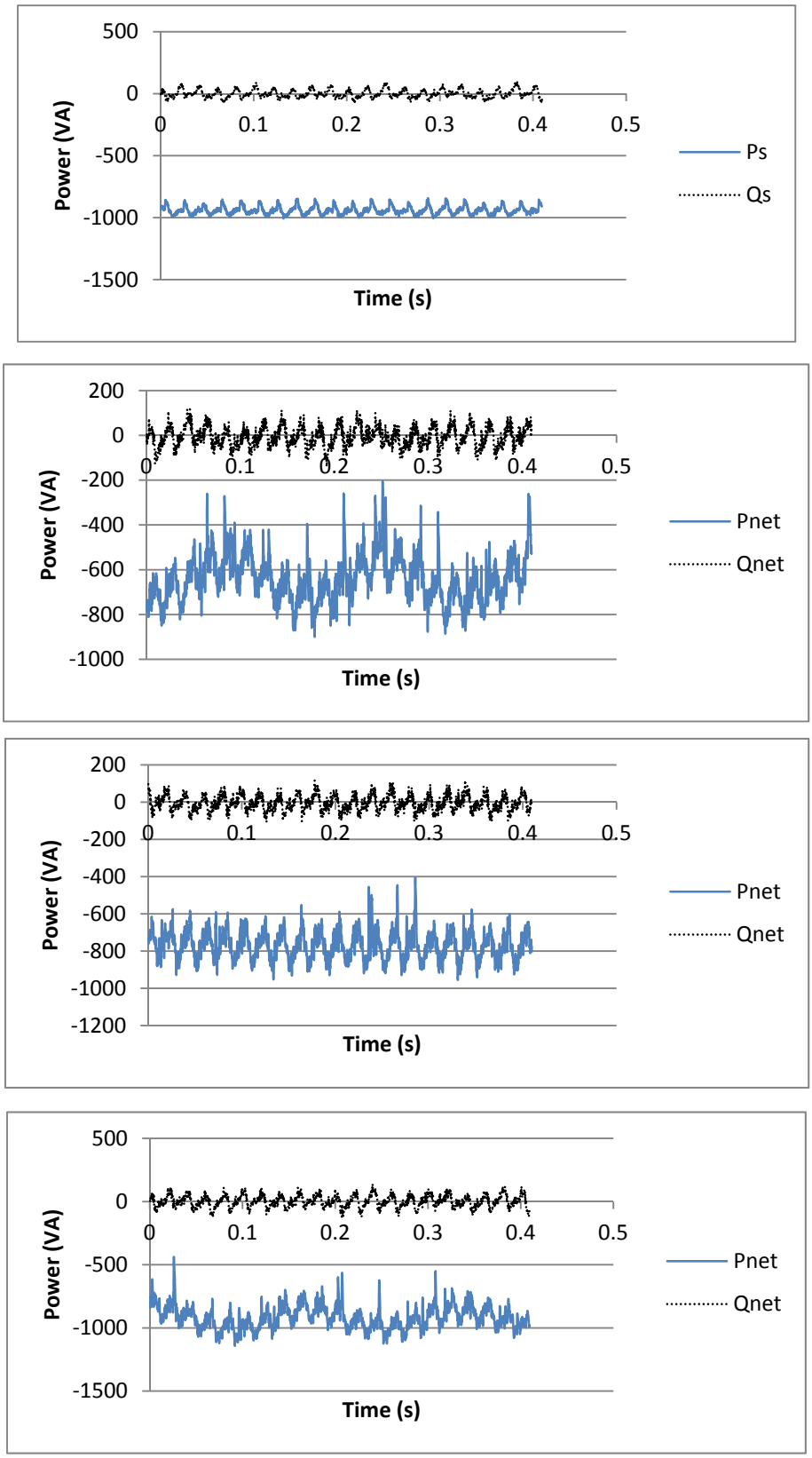

Figure 6.13: Stator Powers at Super-synchronous Speed and Net Powers at Sub-synchronous, Synchronous and Super-synchronous Modes of the DFIM

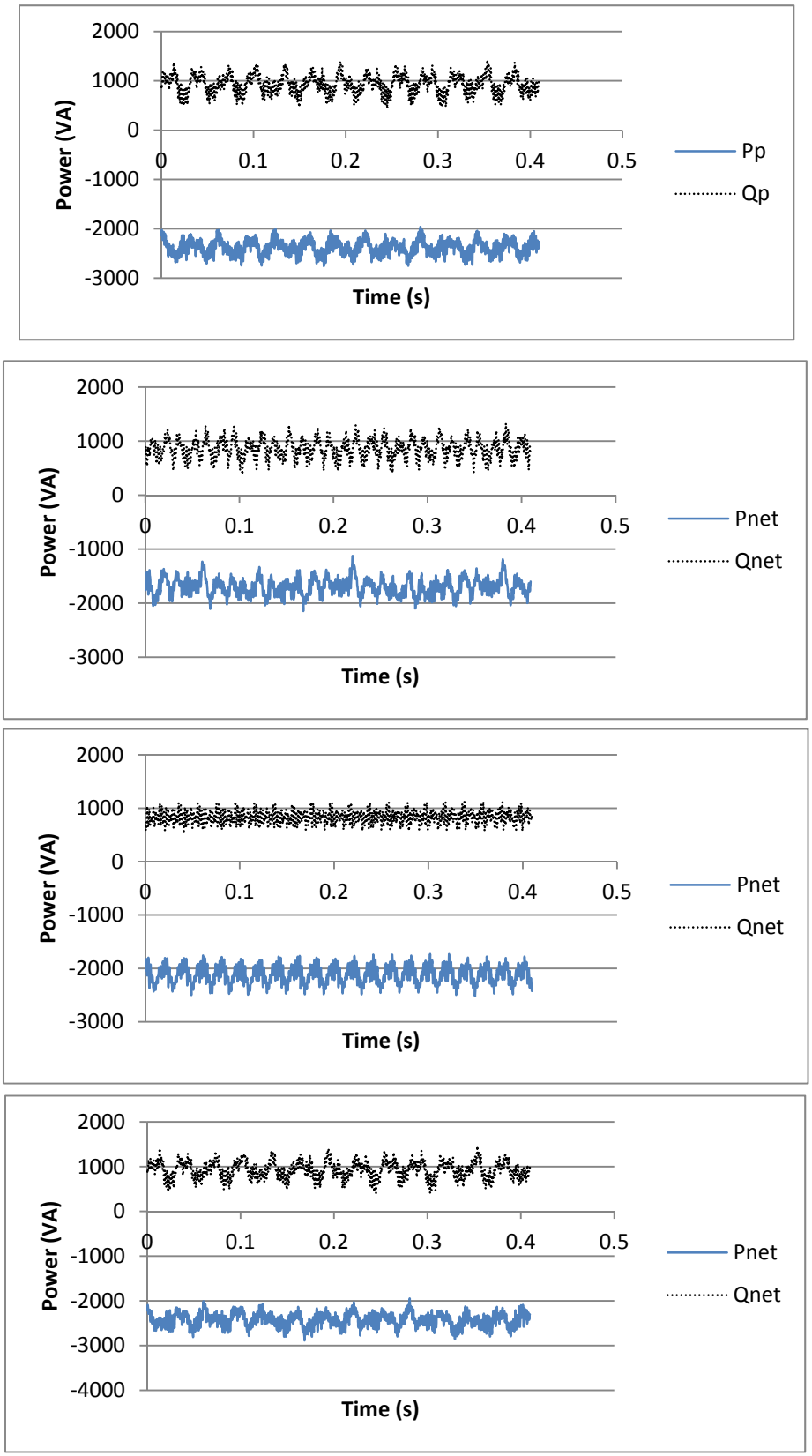

Figure 6.14: Primary Powers at Super-synchronous Speed and Net Powers at Sub-synchronous, Synchronous and Super-synchronous Modes of the BDFRM

In order to make a proper comparison of the machine performance, the results in Figs. 6.9 and 6.11 have been generated for the same current magnitudes of the control windings i.e. the same d-axis rotor (DFIM) and secondary (BDFRM) currents (both set to 7 A), and the same respective q components (both set to -12A). Similarly, the q component of the grid side current is set to 0 A for both the machines to achieve unity power factor. The machines have been supplied with the same terminal voltages, and the DC link voltage for the experiments was maintained at around 300 V by the vector controller, with acceptable variations within ± 5 V range and notable noisy measurements (Figs. 6.10 and 6.12). The noise is caused by lack of power consuming components (resistance/reactance) inside the DC link. The DFIM generates less active power than the BDFRM but is working at unity power factor on the stator side (Figs. 6.13 and 6.14). The reactive power of the grid-connected winding and its net amount are expectedly the same due to the accurate unity power factor control on the grid side of the control windings. Since both the machines can produce more net active power at super-synchronous speed due to power flow direction, the respective power factor can be optimised in this speed region, be as is conventional for the machine's operation in generating regime.

Therefore, a list of tables has been made based on the current settings in Fig. 6.8 to demonstrate the stator/primary side power and the net power of both the DFIM and the BDFRM at super-synchronous speeds in order to analyse and compare active power generation and power factor issues of the two machines. Within the tables, negative sign of the power represents the power generated by the machine, while the positive sign means the power absorbed from the grid.

The difference between the stator (DFIM)/primary (BDFRM) side reactive power and its net value is quite small (Table 6.2 and 6.4, Table 6.6 and 6.8) for either the machine due to the contribution of the controllable q component of grid side current. The maximum stator active power (1507 W) and net active power (1525 W)

generated to the grid, despite the reactive power consumption, occur at I_{rd}=13A, I_{rq}=-9A for the DFIM (Tables 6.1 and 6.3), and at I_{sd}=10A, I_{sq}=-12A for the BDFRM with the maximum primary winding power and net power being 2604 W (Table 6.5) and 2620 W (Table 6.7) respectively. The maximum net power factor for the DFIM occurs at I_{rd}=7A, I_{rq}=-12A (unity according to Table 6.4), and at I_{sd}=1A, I_{sq}=-12A for the BDFRM with a relatively small amount of reactive power being generated to the grid (i.e. at nearly unity power factor – see Tables 6.8 and 6.7).

Table 6.1: Average Active Power (W) Generation on Stator Side of the DFIM

Irq(A) / Ird(A)	-15	-12	-9	-6	-3	0	3	6	9
1	-396	-323	-253	-182	-114	-46	22	88	N/A
4	-719	-630	-555	-484	-412	-349	-277	-209	-142
7	N/A	-940	-864	-790	-714	-651	-577	-506	-438
10	N/A	-1272	-1175	-1097	-1020	-960	-886	-809	-739
13	N/A	N/A	-1507	-1405	-1324	-1270	-1188	N/A	N/A

Table 6.2: Average Reactive Power (VAr) Absorption on Stator Side of the DFIM

Irq(A) / Ird(A)	-15	-12	-9	-6	-3	0	3	6	9
1	-449	-152	145	436	725	1051	1335	1605	N/A
4	-360	-78	215	508	794	1121	1401	1691	1949
7	N/A	1	293	586	873	1187	1465	1745	2026
10	N/A	94	371	662	953	1272	1565	1836	2123
13	N/A	N/A	473	743	1029	1364	1638	N/A	N/A

Table 6.3: Average Net Active Power (W) Generation of the DFIM

Irq(A) / Ird(A)	-15	-12	-9	-6	-3	0	3	6	9
1	-283	-245	-215	-158	-109	-49	33	126	N/A
4	-661	-595	-535	-491	-426	-372	-286	-193	-102
7	N/A	-916	-862	-816	-747	-686	-599	-507	-415
10	N/A	-1273	-1179	-1125	-1062	-1002	-919	-811	-709
13	N/A	N/A	-1525	-1423	-1363	-1302	-1205	N/A	N/A

Table 6.4: Average Net Reactive Power (VAr) Absorption of the DFIM

Irq(A) / Ird(A)	-15	-12	-9	-6	-3	0	3	6	9
1	-449	-151	146	436	725	1050	1334	1605	N/A
4	-360	-78	215	508	794	1121	1401	1691	1948
7	N/A	0	294	586	873	1188	1465	1745	2026
10	N/A	94	372	661	952	1272	1565	1836	2123
13	N/A	N/A	474	744	1030	1365	1639	N/A	N/A

Table 6.5: Average Active Power (W) Generation on Primary Side of the BDFRM

Isq(A) / Isd(A)	-15	-12	-9	-6	-3	0	3	6	9
1	-2225	-1811	-1390	-942	-519	-75	385	780	N/A
4	-2493	-2108	-1694	-1266	-848	-411	39	457	836
7	N/A	-2368	-1792	-1556	-1151	-705	-267	145	545
10	N/A	-2604	-2216	-1811	-1418	-987	-550	-147	244
13	N/A	N/A	-2431	-2050	-1663	-1255	-822	N/A	N/A

Table 6.6: Average Reactive Power (VAr) Absorption on Primary Side of the BDFRM

Isq(A) / Isd(A)	-15	-12	-9	-6	-3	0	3	6	9
1	-112	-51	92	262	514	834	1152	1465	N/A
4	345	420	561	742	1001	1310	1580	1888	2166
7	N/A	925	1061	1239	1503	1777	2017	2306	2571
10	N/A	1426	1561	1745	1996	2253	2460	2752	2976
13	N/A	N/A	2055	2246	2482	2729	2897	N/A	N/A

Table 6.7: Average Net Active Power (W) Generation of the BDFRM

Isq(A) / Isd(A)	-15	-12	-9	-6	-3	0	3	6	9
1	-2197	-1836	-1445	-997	-556	-75	448	914	N/A
4	-2493	-2157	-1775	-1342	-908	-431	80	571	1028
7	N/A	-2419	-1861	-1633	-1207	-721	-231	248	729
10	N/A	-2620	-2270	-1861	-1454	-985	-496	-35	433
13	N/A	N/A	-2425	-2045	-1658	-1214	-733	N/A	N/A

Table 6.8: Average Net Reactive Power (VAr) Absorption of the BDFRM

Isq(A) / Isd(A)	-15	-12	-9	-6	-3	0	3	6	9
1	-113	-52	91	261	513	833	1152	1465	N/A
4	344	419	560	741	1000	1310	1580	1888	2166
7	N/A	923	1059	1238	1501	1776	2016	2305	2571
10	N/A	1424	1559	1743	1994	2251	2459	2752	2976
13	N/A	N/A	2054	2245	2481	2728	2896	N/A	N/A

Having examined the results tabulated in Table 6.3, it appears that the active power generation of the DFIM is largely affected by the d-axis rotor current and

proportionally little by the corresponding q component which is expected from the stator voltage oriented (vector) control theory. In the BDFRM case (Table 6.7), under primary voltage oriented control, however, the real power production is more evenly influenced by the d and q components of the secondary current which seems to indicate that the coupling effect is more significant with this machine for the adopted reference frame selection (i.e. d-axis alignment with the voltage vector).

In order to verify the previously made observations (conjectures) about the d-q control current influences on the net power production, and for comparison, of the machines, the relevant results from the above tables have been graphically presented in Figs. 6.15 and 6.16. From Fig. 6.15, which shows the real power variations with the d-axis rotor (DFIM) /secondary (BDFRM) winding current, one can see that there is nearly a linear power-current relationship with about 45º slope for the DFIM unlike the somewhat non-linear BDFRM curve. This fact seems to suggest that the real power of the DFIM is mainly determined by the d-axis current, this not being quite the case with the BDFRM as anticipated above. On the other hand, inspecting Fig. 6.16, which illustrates the opposite scenario, both the power characteristics look nearly linear, the BDFRM one having a much steeper slope (around 45º similarly to the DFIM power curve in Fig. 6.15) compared to the DFIM. This means that the q-axis current variations will cause proportionally little changes in the real power levels i.e. this current component has a less dominant effect on the DFIM power production than the d-axis counterpart.

Therefore, to optimise the power factor as well as both the stator/primary power and net power values, I_{rd} should be big enough and I_{rq} should be kept at small negative value for the DFIM, while I_{sq} should be as small as possible negative value and I_{sd} close to zero but with a positive value for the BDFRM. All reference current settings should be within the boundary shown in Fig. 6.8. This could also make both machines generate reasonably high active power.

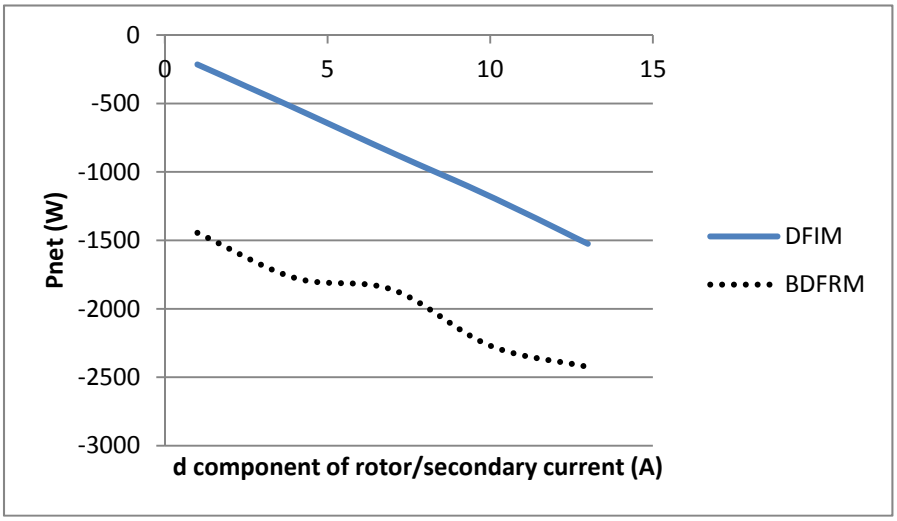

Figure 6.15: Generated Net Active Power of the DFIM and the BDFRM for q-axis Control Winding Current Magnitude of -9 A

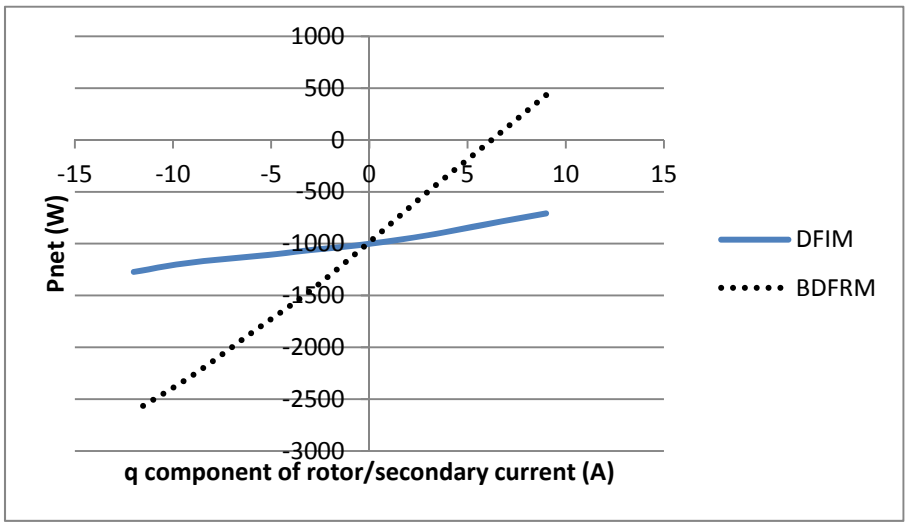

Figure 6.16: Generated Net Active Power of the DFIM and the BDFRM for d-axis Control Winding Current Magnitude of 10 A

6.4 Vector Control of MSC in Speed Mode

Since certain torque is not controllable from the drive side, the results presented in this section refer to the DFIM and the BDFRM both operating as unloaded motors. Speed control, discussed in Chapter 5 as the outer loop to generate reference signals for the d-axis rotor (DFIM)/secondary (BDFRM) current, was implemented in

real-time to achieve variable speed operation of the machine, and to evaluate the controller performance, under no-load conditions.

During the experiment, after powering up the supply voltage, the GSC has been enabled to make sure the DC link voltage is controlled at 300 V and power factor in unity on the grid side. The MSC is then activated to speed up the DFIM/BDFRM to track the desired speed. The speed control performance and the corresponding current and power plots of the DFIM and the BDFRM obtained by executing the stator/primary voltage oriented torque control are demonstrated by the experimental results in Figs. 6.17 - 6.20.

It can be seen from Fig. 6.17 that the DFIM can speed up from sub-synchronous speed (660 rpm) to synchronous speed (750 rpm), and further to super-synchronous speed (840 rpm) within 0.5s for each speed transition, and vice-versa while sequentially slowing down in the same steps to the initial speed. The corresponding d-axis rotor current and stator real/reactive power waveforms have been generated for the q-axis rotor current being controlled at 0 A. Since this speed control is for no-load situation, there is no need for active power from the stator side (except a little amount to cover losses). However, reasonable reactive power is required from the grid for magnetisation purposes as the machine operates at a very low stator power factor under unloaded conditions, and there is a marginal contribution by the rotor winding for the considered q current component setting. Characteristic transients in the d rotor current and the stator real power in response to the reference speed variations are notable in the respective waveforms which are similar in shape reinforcing again the pre-dominant effect of the rotor d current on the stator power mentioned earlier. Finally, as the d-q current (torque) control is not decoupled, the uncompensated coupling effects between the d and q control loops manifest themselves as disturbance in the reactive power profile in particular as clearly indicated by the dotted line on the last plot in the same figure.

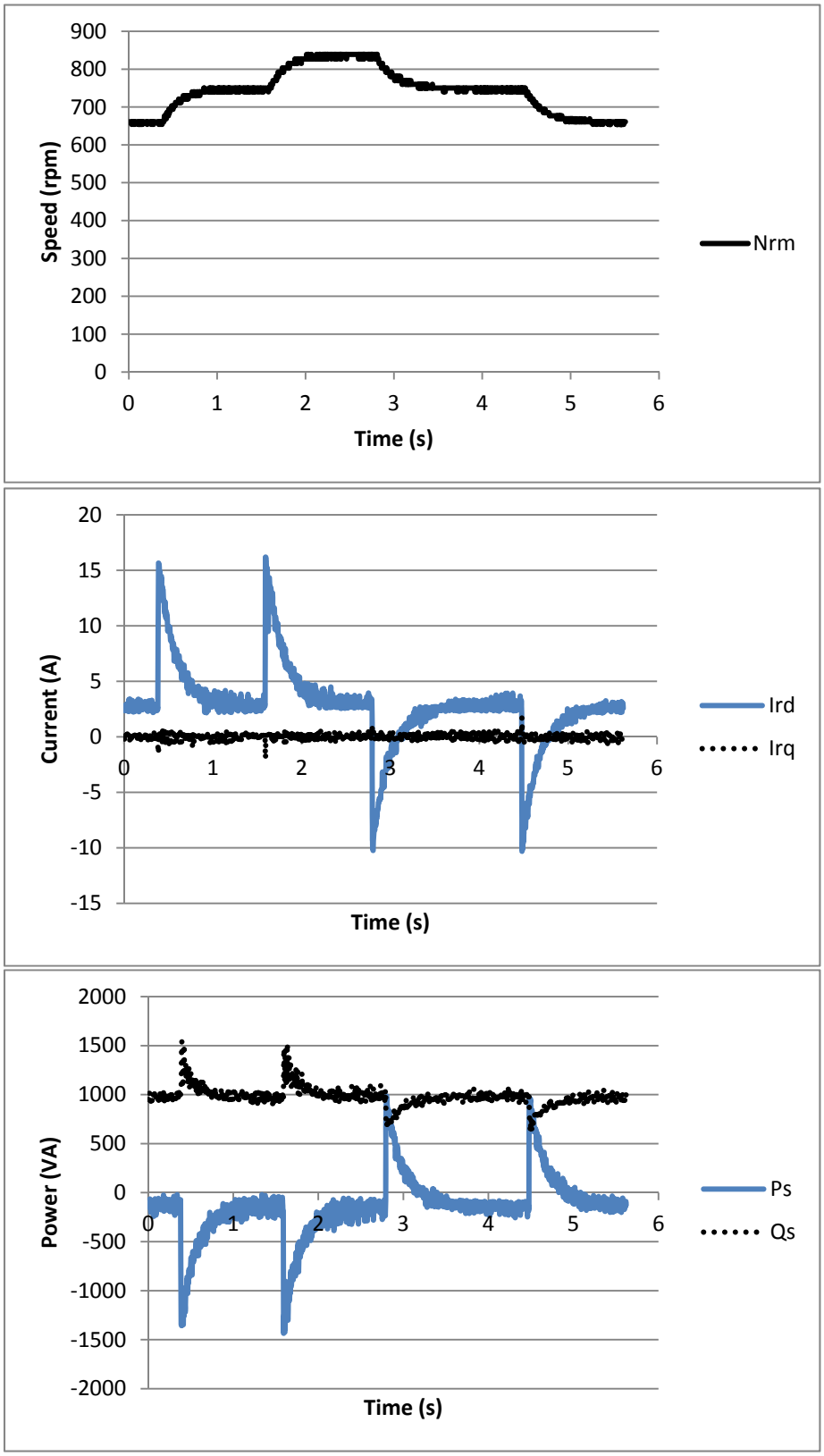

Figure 6.17: Unloaded DFIM Response to Step-changes of Reference Speed in Sub-synchronous, Synchronous and Super-synchronous Modes: Speed (top); Rotor Current (middle); Stator Real and Reactive Power (bottom)

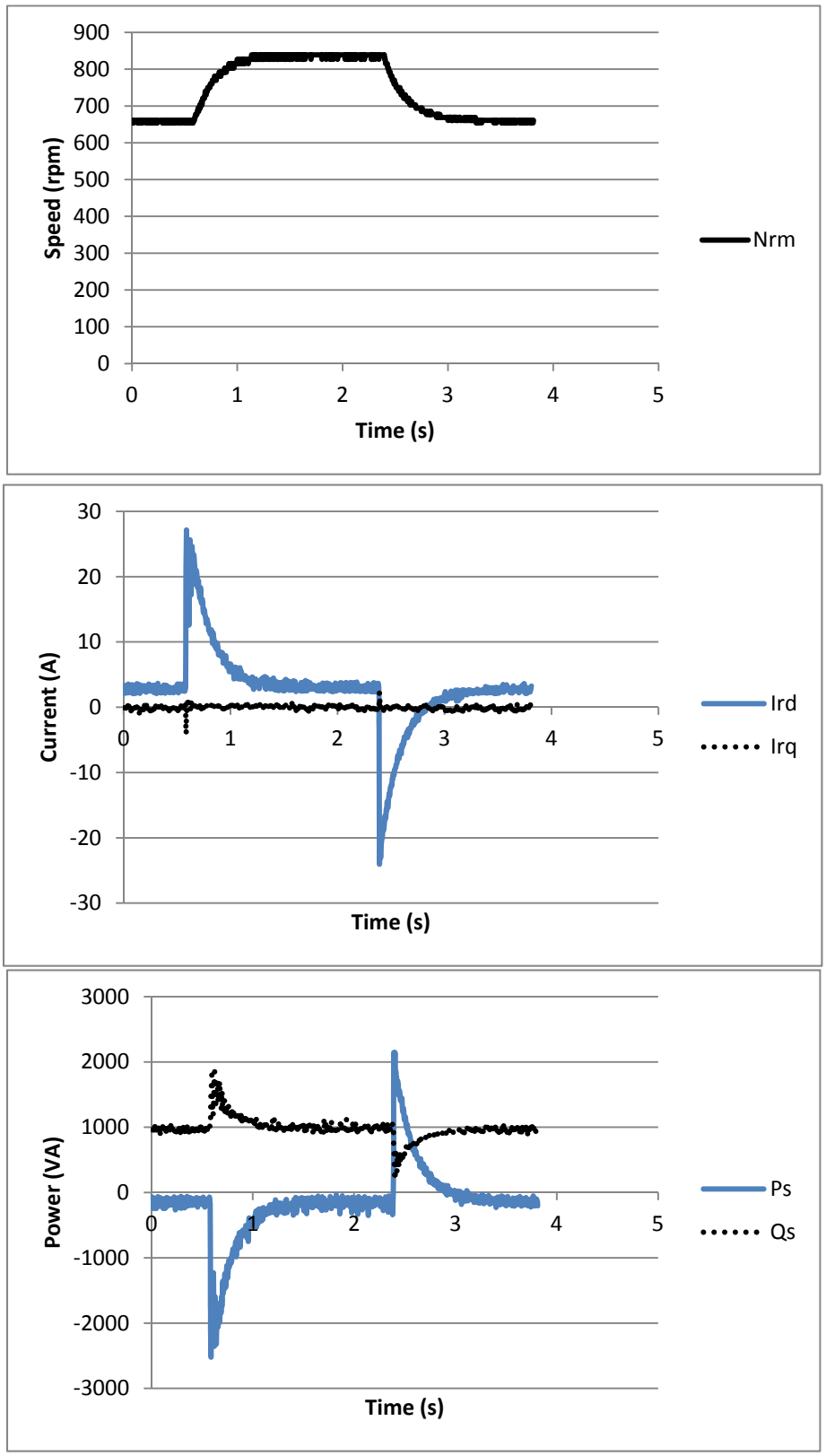

Figure 6.18: Unloaded DFIM Response to Varying Speed References in a Limited Range around Synchronous Speed: Speed (top); Rotor Current (middle) and Stator Powers (bottom)

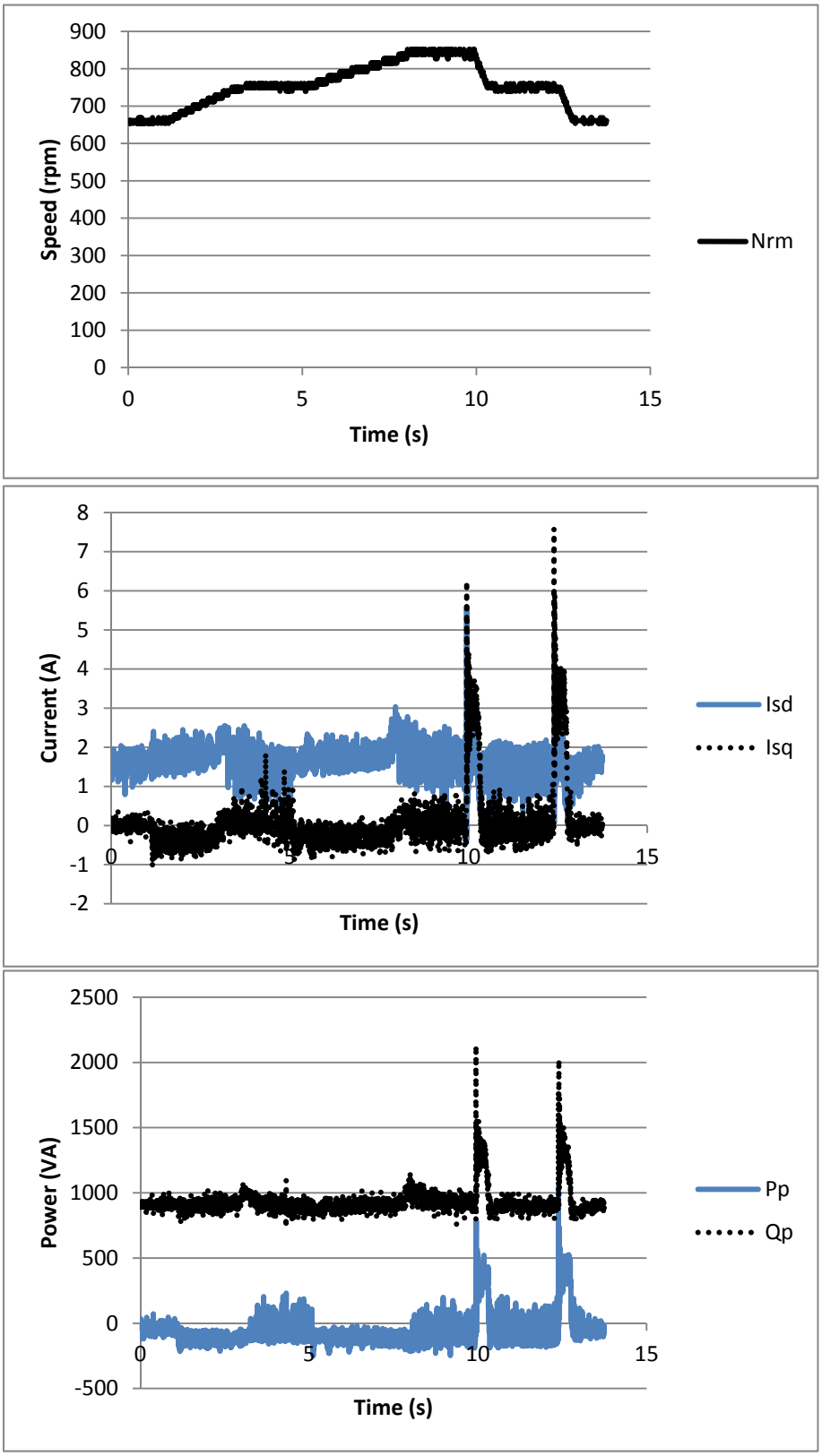

Figure 6.19: Unloaded BDFRM Response to Step-changes of Reference Speed in Sub-synchronous, Synchronous and Super-synchronous Modes: Speed (top); Rotor Current (middle); Stator Real and Reactive Power (bottom)

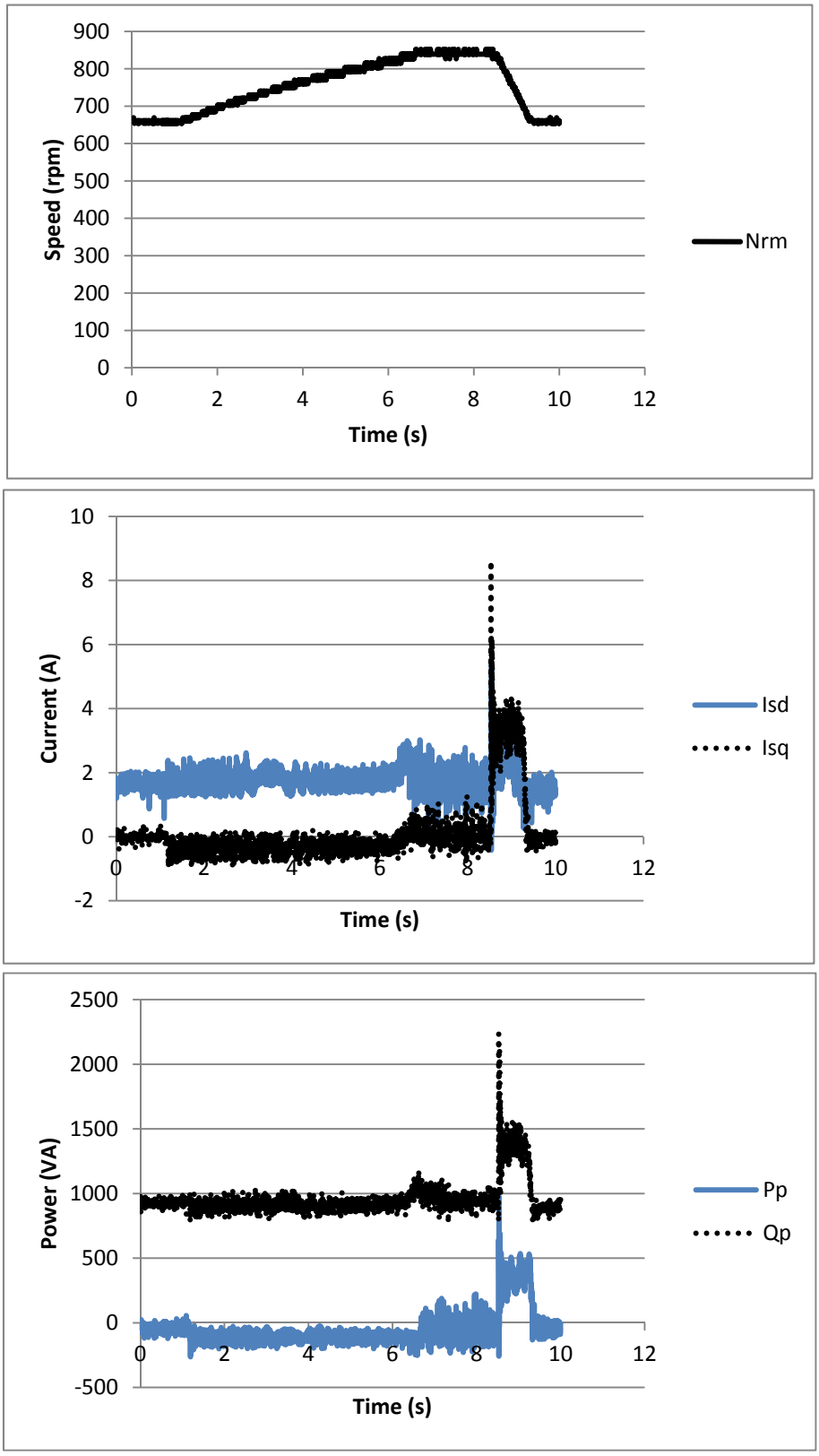

Figure 6.20: Unloaded BDFRM Response to Varying Speed References in a Limited Range around Synchronous Speed: Speed (top); Secondary Current (middle) and Primary Powers (bottom)

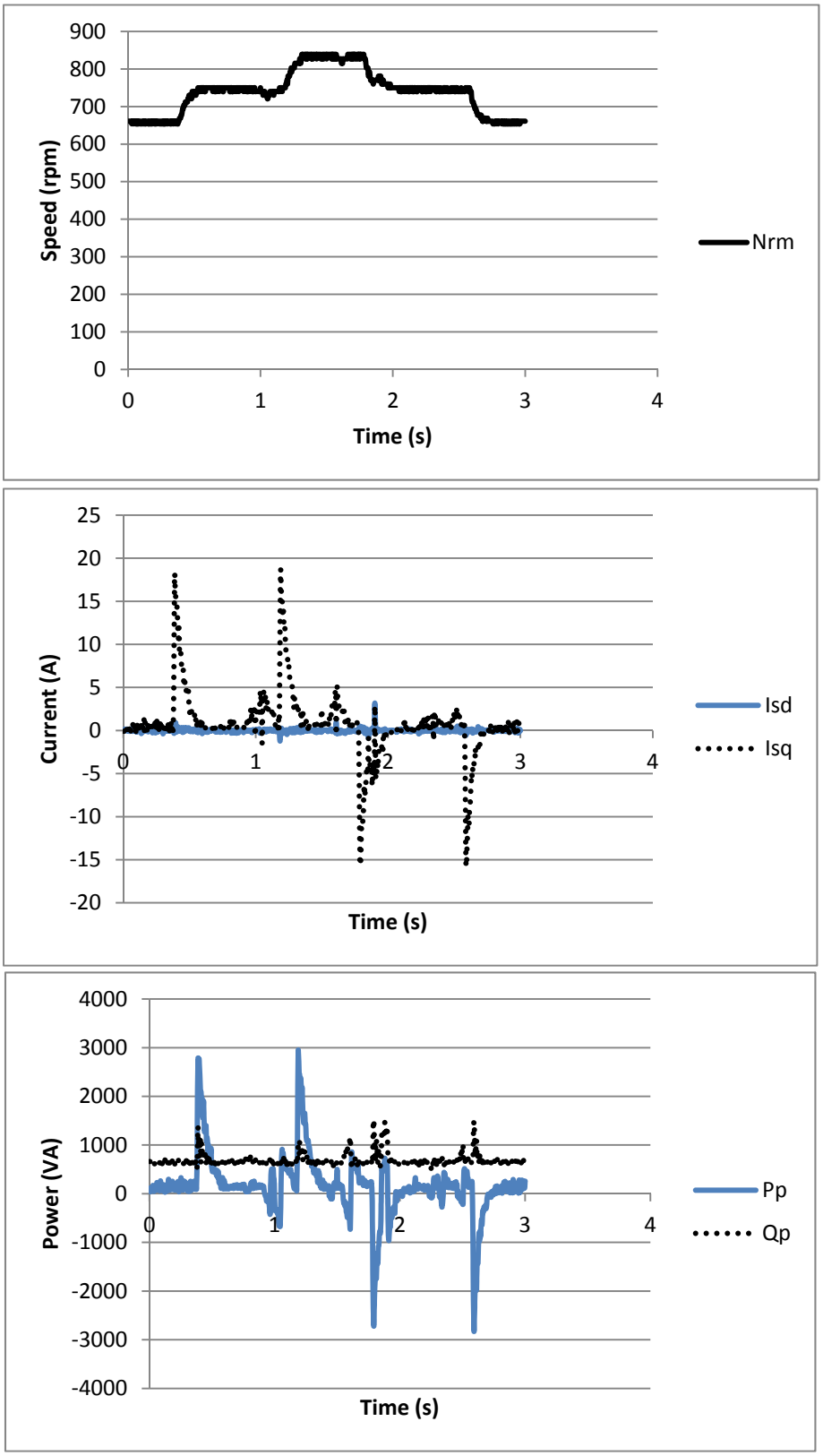

Figure 6.21: Improved Speed Control Performance of the BDFRM in a Limited Speed Range around and at Synchronous Speed

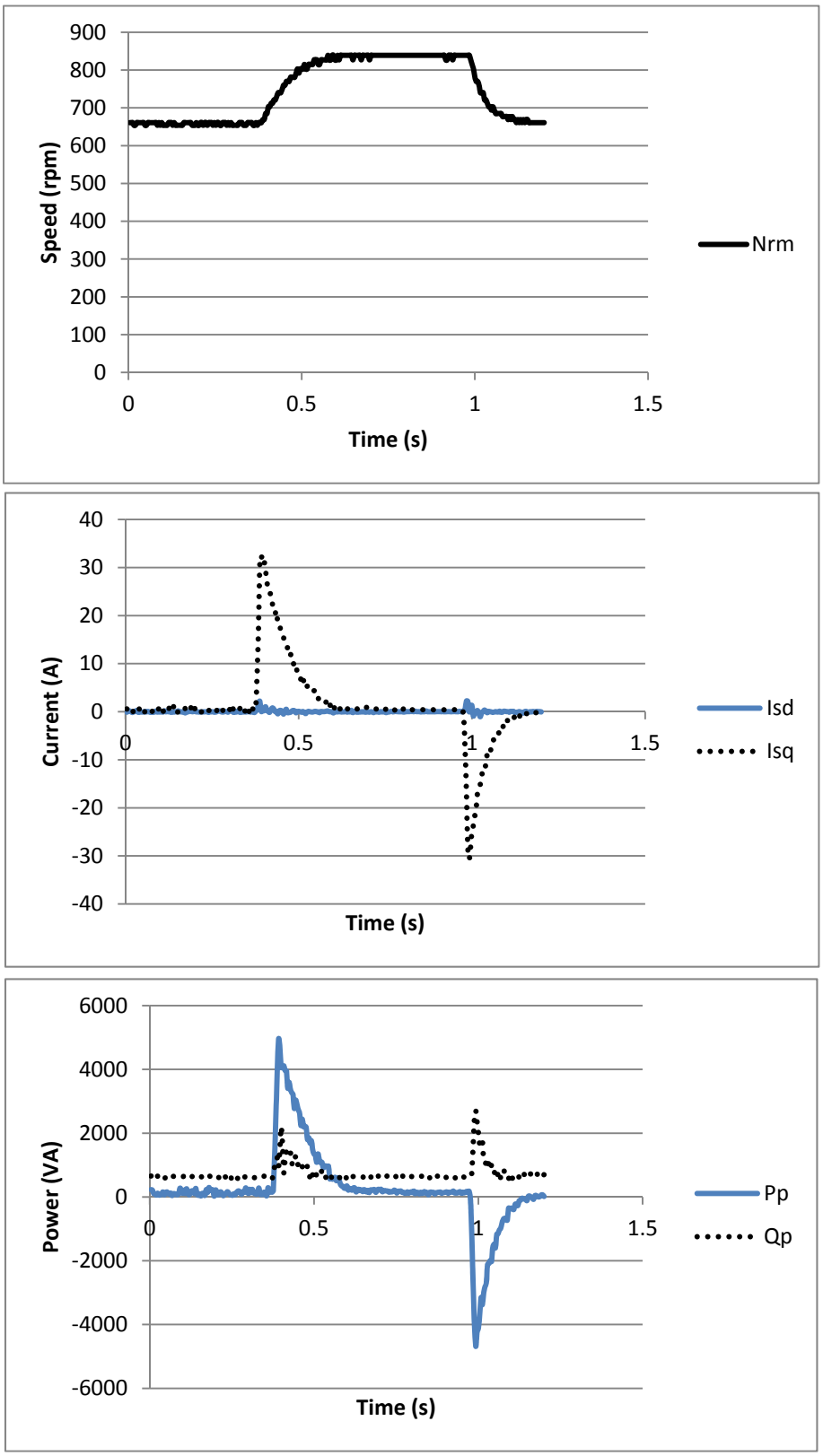

Figure 6.22: Improved Speed Control Performance of the BDFRM in Sub-synchronous and Super-synchronous Modes

Similar test results to Fig. 6.17 were obtained for another case study in which the DFIM/controller response to speed changes from sub-synchronous (660 rpm) to super-synchronous speed (840 rpm), and vice-versa, was investigated. These are illustrated in Fig. 6.18.

The speed control performance of the BDFRM with primary voltage oriented control is represented by the plots in Figs. 6.19 and 6.20. These results have been generated under the same test and operating conditions as those for the DFIM equivalent shown in the corresponding Figs. 6.17 and 6.18 for comparison. Benchmarking the respective waveforms, one can notice a generally slower transient response and inferior dynamic performance of the BDFRM overall relative to the DFIM which can be partly attributed to the implications of the unusual operating principle of the former such as the much higher leakage reactance and richer harmonic content. Foremost, with the d-axis (rather than q-axis) reference frame alignment with the primary voltage vector being adopted for control purposes by analogy to the DFIM case, the coupling effects between the d-q secondary current control loops and associated control inaccuracies appear to be much more pronounced in the BDFRM which contributes to a great extent to its further performance degradation. It is interesting to note, however, that despite this poor dynamic performance, the BDFRM seems to require slightly less primary reactive power for magnetisation with real power consumption similar to DFIM in steady-state, which implies its somewhat better power factor under unloaded operating conditions no matter the little practical interest of this apparent BDFRM advantage.

In order to minimise the detrimental coupling effects and to improve dynamic performance of the BDFRM, a reference frame q-axis has been aligned with the primary voltage vector to achieve conditions very close to the primary-flux (field) oriented control (and especially with larger machines where the winding resistances are smaller) where the frame d-axis is normally aligned with the primary flux which,

more importantly, is well-known to allow the inherently decoupled d-q current (i.e. torque and reactive power) control unlike the classical voltage oriented (vector) control [5]. This alternative reference frame choice has indeed provided a considerable BDFRM performance improvement (Figs. 6.21 and 6.22) relative to that in Figs. 6.19 and 6.20, and even superior to the DFIM in Figs. 6.17 and 6.18. Although the machine transient response is not that much of importance for the considered target applications, it is worth mentioning that it is now much faster (it only takes about 0.2s for the BDFRM to speed up from 660 rpm to 840 rpm according to Fig. 6.22) which is more than obvious from Figs. 6.21 and 6.22. The coupling effects have not been eliminated (as can be seen from the power plots in Fig. 6.22) but the resulting waveforms are much cleaner, noise free and current control accuracy substantially better compared to that in Figs. 6.19 and 6.20 and similar in quality to the DFIM ones in Figs. 6.17 and 6.18. It should be noted that had the same reference frame selection been implemented in the vector controller of the DFIM rig, the resulting transient response would, most likely, have been faster than that achievable with the BDFRM in Figs. 6.21 and 6.22, and d-q coupling effects would have been further reduced compared to those in Figs. 6.17 and 6.18.

6.5 Conclusions

This chapter has presented the experimental results using stator (DFIM)/primary (BDFRM) voltage oriented vector controller implemented on a DSP development platform for both the DFIM and the BDFRM on two separate, identical, test rigs. The example machines, driven by a commercial cage induction machine drive, are controlled with both the open-loop (torque mode) and closed-loop speed control over a limited speed range of interest to the main target applications (e.g. wind turbines and large pump drives) using a shaft position encoder and a bi-directional (back-to-back) power electronic converter.

The simulation results presented in Section 5.3 and 5.4 are experimentally validated in Section 6.2 and 6.3 respectively having the same operation conditions in rotating speed, current references, grid voltage, space vector PWM frequency and parameters of the controller etc. By comparing the simulation and experimental results in the sections stated above, controlled variables (grid current or rotor/secondary current) are tracking the referenced values in very fast response with no overshoot. Also, the variables accordingly (stator/primary current and stator/primary power) are altering in the same trends but with some difference in magnitude due to the inaccuracy of off-line testing of machine parameters and some noise issues during the experiment.

Whenever possible, the performance of the controller/machine has been examined under the same transient and steady state operating conditions for comparison purposes. The following important conclusions/observations can be drawn from this comparative analysis and the results obtained:

(1) Vector control algorithms are working properly on both the GSC and MSC of the DFIM and the BDFRM. Good dynamic performance of the rotor (DFIM) /secondary (BDFRM) winding current and grid side current controllers has been achieved both with very fast response.
(2) Stator power and net power have been analysed in generating operating mode of the machines for various rotor/secondary side current settings, carefully selected to avoid over currents in the windings, and to allow a proper evaluation of the torque control performance. The current set-points for unity power factor and the maximum net and stator/primary active power regions have been identified, and approaches for performance optimisations have been proposed, for both the DFIM and the BDFRM. The BDFRM could generate more active power than the DFIM in the current set-point of unity power factor.
(3) Variable speed operation has been achieved applying the stator/primary voltage oriented control algorithms for the unloaded machines operating as motors. Due to

the poor dynamic performance of the speed control loop of the BDFRM, a modified vector control scheme offering performance competitive to primary flux oriented control has been employed for the performance improvement. After the modification, the BDFRM could track the desired speed faster than the DFIM.

The most significant contribution of this chapter is the successful experimental verification of the stator/primary voltage oriented control algorithm developed in Chapter 4, and subsequently simulated in Chapter 5, for both the BDFRM and the DFIM. This chapter concentrated on the real-time implementation issues and presentation and discussion of the scheme's performance as well as comparative analysis of the machine operation in terms of the grid side power factor and real/reactive power production. The BDFRM has as good or even better performance than the DFIM when applied with vector control algorithm.

7. Conclusions and Extensions

Throughout the entire research work, a number of primary and secondary objectives have been accomplished in line with the project plan including:

1. Literature review on dynamic modelling, control (e.g. methods and DSP implementation aspects) and applications (e.g. wind power generation, grid integration etc.) of doubly-fed machines focusing on traditional wound rotor (DFIM) and emerging brushless reluctance types (BDFRM).
2. Critical evaluation of various control schemes reported in the referenced literature and assessment of their suitability for the considered target applications with limited speed ranges (e.g. wind turbines) where robustness and machine parameter independence are the main selection criteria.
3. Development and simulations of a grid-connected winding voltage oriented (vector) control algorithm for both the machine side and grid side (back-to-back) conventional IGBT converter using the parameters obtained by off-line testing from the existing DFIM and BDFRM test rigs in the power laboratory.
4. Active participation and involvement in the design, manufacture and testing of the 6.75 kW DFIM and 4 kW BDFRM test rigs under normal operating conditions.
5. Real-time implementation and experimental verification of the simulation studies of the developed vector control scheme on both the DFIM and the BDFRM test rigs; comparisons of the machines performance based on the experimental results in terms of power production and/or power factor.

The experiments conducted on the two machines built in the same stator frame have indicated that the BDFRM (if optimally designed) may take more than a competitive position relative to the DFIM in small scale variable speed applications. However, before making any definite conclusions whether the BDFRM can be indeed treated as

a viable DFIM alternative, further research work should be undertaken in either of, but not limited to, the following directions:

1. Advanced performance comparison between the DFIM and the BDFRM in terms of parameters not considered in this thesis (such as efficiency) using field-oriented control (preferably without a shaft position sensor to avoid reliability issues associated with the DFIM) where the torque/real power and reactive power control is inherently decoupled for both the machines.
2. Improve the stability of the interface board of the eZdsp and resolve EMI problems inside the control cabinet to avoid noise issues and make sure the test rigs could work at full voltage rating (380V line-to-line) to achieve more significant results.
3. Integration and test of crowbar and fault emulator with DFIM/BDFRM test rigs to assess fault-ride-through (FRT) capabilities of the machines where the BDFRM may have a potential advantage over the DFIM due to the lower fault current levels afforded by the higher leakage reactance.
4. Multi-pole BDFRM designs for direct gearless drives or geared wind turbines with a low-level gearbox.
5. Building larger BDFRM prototypes and comparisons with DFIM counterparts to establish to what extent the small-scale conclusions can be carried over to large scale systems.

8. References

[1] "The 2020 UK Renewable Energy Roadmap," Department of Energy and Climate Change, 2011.

[2] P. J. Tavner, “Review of Condition Monitoring of Rotating Electrical Machines,” *IET Electric Power Applications,* vol. 2, no. 4, pp. 215-247, 2008.

[3] O. Ojo and Z. Wu, "Synchronous Operation of a Dual-Winding Reluctance Generator," *IEEE Transactions on Energy Conversion,* vol. 12, pp. 357-362, 1997.

[4] S. Williamson, A. C. Ferreira, and A. K. Wallace, "Generalised Theory of the Brushless Doubly-Fed Machine. I. Analysis," *IEE Proceedings - Electric Power Applications,* vol. 144, pp. 111-122, 1997.

[5] S. Williamson and A. C. Ferreira, "Generalised Theory of the Brushless Doubly-Fed Machine. 2. Model Verification and Performance," *IEE Proceedings - Electric Power Applications,* vol. 144, pp. 123-129, 1997.

[6] P. C. Roberts, R. A. McMahon, P. J. Tavner, J. M. Maciejowski, and T. J. Flack, "Equivalent Circuit for the Brushless Doubly Fed Machine (BDFM) Including Parameter Estimation and Experimental Verification," *IEE Proceedings Electric Power Applications,* vol. 152, pp. 933-942, 2005.

[7] R. A. McMahon, P. C. Roberts, X. Wang, and P. J. Tavner, "Performance of BDFM as Generator and Motor," *IEE Proceedings Electric Power Applications,* vol. 153, pp. 289-299, 2006.

[8] J. Poza, E. Oyarbide, D. Roye, and M. Rodriguez, "Unified Reference Frame dq Model of the Brushless Doubly Fed Machine," *IEE Proceedings Electric Power Applications,* vol. 153, pp. 726-734, 2006.

[9] K. Protsenko and D. Xu, "Modeling and Control of Brushless Doubly-Fed Induction Generators in Wind Energy Applications," *IEEE Transactions on Power Electronics,* vol. 23, pp. 1191-1197, 2008.

[10] R. Pena, J. C. Clare, and G. M. Asher, "A Doubly Fed Induction Generator Using Back-To-Back PWM Converters Supplying an Isolated Load From a Variable Speed Wind Turbine," *IEE Proceedings-Electric Power Applications,* vol. 143, pp. 380-387, 1996.

[11] I. Boldea, *Variable Speed Generators: The Electric Generators Handbook*: CRC PressINC, 2006, ISBN 0-84-935715-2.

[12] Y. Liao, L. Ran, G. A. Putrus, and K. S. Smith, "Evaluation of the Effects of Rotor Harmonics in a Doubly-Fed Induction Generator with Harmonic Induced Speed Ripple," *IEEE Transactions on Energy Conversion,* vol. 18, pp. 508-515, 2003.

[13] D. Zhi and L. Xu, "Direct Power Control of DFIG with Constant Switching Frequency and Improved Transient Performance," *IEEE Transactions on Energy Conversion,* vol. 22, pp. 110-118, 2007.

[14] L. Xu and P. Cartwright, "Direct Active and Reactive Power Control of DFIG for Wind Energy Generation," *IEEE Transactions on Energy Conversion,* vol. 21, pp. 750-758, 2006.

[15] S. V. Bozhko, R. Blasco-Gimenez, L. Risheng, J. C. Clare, and G. M. Asher, "Control of Offshore DFIG-Based Wind Farm Grid with Line-Commutated HVDC Connection," *IEEE Transactions on Energy Conversion,* vol. 22, pp. 71-78, 2007.

[16] R. Pena, R. Cardenas, E. Escobar, J. Clare, and P. Wheeler, "Control System for Unbalanced Operation of Stand-Alone Doubly Fed Induction Generators," *IEEE Transactions on Energy Conversion,* vol. 22, pp. 544-545, 2007.

[17] S. Heier, *Grid Integration of Wind Energy Conversion Systems*: John Wiley & Sons, 1998, ISBN 0-47-086899-6.

[18] W. Leonhard, *Control of Electrical Drives*, 3rd ed. Berlin: Springer, 2001, ISBN 3-54-041820-2.

[19] R. Pena, J. C. Clare, and G. M. Asher, "Doubly Fed Induction Generator Using Back-to-Back PWM Converters and Its Application to Variable-Speed Wind-Energy Generation," *IEE Proceedings Electric Power Applications,* vol. 143, pp. 231-241, 1996.

[20] L. Morel, H. Godfroid, A. Mirzaian, and J. M. Kauffmann, "Double-Fed Induction Machine: Converter Optimisation and Field Oriented Control Without Position Sensor," *IEE Proceedings-Electric Power Applications,* vol. 145, pp. 360-368, 1998.

[21] P. Ledesma and J. Usaola, "Doubly Fed Induction Generator Model for Transient Stability Analysis," *IEEE Transactions on Energy Conversion,* vol. 20, pp. 388-397, 2005.

[22] S. Muller, M. Deicke, and R. W. De Doncker, "Doubly Fed Induction Generator Systems for Wind Turbines," *IEEE Industry Applications Magazine,* vol. 8, pp. 26-33, May-Jun 2002.

[23] L. Holdsworth, X. G. Wu, J. B. Ekanayake, and N. Jenkins, "Direct Solution Method for Initialising Doubly-Fed Induction Wind Turbines in Power System Dynamic Models," *IEE Proceedings Generation, Transmission and Distribution,* vol. 150, pp. 334-342, 2003.

[24] L. Holdsworth, X. G. Wu, J. B. Ekanayake, and N. Jenkins, "Comparison of Fixed Speed and Doubly-Fed Induction Wind Turbines During Power System Disturbances," *IEE Proceedings Generation, Transmission and Distribution,* vol. 150, pp. 343-352, 2003.

[25] F. M. Hughes, O. Anaya-Lara, N. Jenkins, and G. Strbac, "A Power System Stabilizer for DFIG-Based Wind Generation," *IEEE Transactions on Power Systems,* vol. 21, pp. 763-772, 2006.

[26] B. H. Chowdhury and S. Chellapilla, "Double-Fed Induction Generator Control for Variable Speed Wind Power Generation," *Electric Power Systems Research,* vol. 76, pp. 786-800, 2006.

[27] A. D. Hansen, P. Sørensen, F. Iov, and F. Blaabjerg, "Centralised Power Control of Wind Farm with Doubly Fed Induction Generators," *Renewable Energy,* vol. 31, pp. 935-951, 2006.

[28] F. M. Hughes, O. Anaya-Lara, N. Jenkins, and G. Strbac, "Control of DFIG-Based Wind Generation for Power Network Support," *IEEE Transactions on Power Systems,* vol. 20, pp. 1958-1966, 2005.

[29] D. W. Xiang, L. Ran, J. R. Bumby, P. J. Tavner, and S. C. Yang, "Coordinated Control of an HVDC Link and Doubly Fed Induction Generators in a Large Offshore Wind Farm," *IEEE Transactions on Power Delivery,* vol. 21, pp. 463-471, 2006.

[30] N. P. Quang, A. Dittrich, and A. Thieme, "Doubly-Fed Induction Machine as Generator: Control Algorithms with Decoupling of Torque and Power Factor," *Electrical Engineering,* vol. 80, pp. 325-335, 1997.

[31] R. Spée, S. Bhowmik, and J. H. R. Enslin, "Novel Control Strategies for Variable-Speed Doubly Fed Wind Power Generation Systems," *Renewable Energy,* vol. 6, pp. 907-915, 1995.

[32] F. Wu, X. Zhang, P. Ju, and M. J. H. Sterling, "Decentralized Nonlinear Control of Wind Turbine with Doubly Fed Induction Generator," *IEEE Transactions on Power Systems,* vol. 23, pp. 613-621, 2008.

[33] F. A. Bhuiyan and A. Yazdani, "Multimode Control of a DFIG-Based Wind-Power Unit for Remote Applications," *IEEE Transactions on Power Delivery,* vol. 24, pp. 2079-2089, 2009.

[34] L. Xu, D. Zhi, and B. W. Williams, "Predictive Current Control of Doubly Fed Induction Generators," *IEEE Transactions on Industrial Electronics,* vol. 56, pp. 4143-4153, 2009.

[35] E. Tremblay, S. Atayde, and A. Chandra, "Comparative Study of Control Strategies for the Doubly Fed Induction Generator in Wind Energy Conversion Systems: A DSP-Based Implementation Approach," *IEEE Transactions on Sustainable Energy,* vol. 2, pp. 288-299, 2011.

[36] S. E. Ben Elghali, M. E. H. Benbouzid, and J. F. Charpentier, "Modelling and Control of a Marine Current Turbine-Driven Doubly Fed Induction Generator," *IET Renewable Power Generation,* vol. 4, pp. 1-11, 2010.

[37] J. M. Rodriguez, J. L. Fernandez, D. Beato, R. Iturbe, J. Usaola, P. Ledesma, *et al.*, "Incidence on Power System Dynamics of High Penetration of Fixed Speed and Doubly Fed Wind Energy Systems: Study of the Spanish Case," *IEEE Transactions on Power Systems,* vol. 17, pp. 1089-1095, 2002.

[38] T. Burton, D. Sharpe, N. Jenkins, and E. Bossanyi, *Wind Energy Handbook*: John Wiley & Sons, 2001, ISBN 0-47-148997-2.

[39] I. Cadirci and M. Ermis, "Double-Output Induction Generator Operating at Subsynchronous and Supersynchronous Speeds: Steady-State Performance Optimisation and Wind-Energy Recovery," *IEE Proceedings Electric Power Applications,* vol. 139, pp. 429-442, 1992.

[40] S. Drid, M.-S. Nait-Said, A. Makouf, and M. Tadjine, "Doubly Fed Induction Generator Modeling and Scalar Controlled for Supplying an Isolated Site," *Journal of Electrical Systems,* vol. 2, pp. 103-115, 2006.

[41] Z. Wang, Y. Sun, G. Li, and B. T. Ooi, "Magnitude and Frequency Control of Grid-Connected Doubly Fed Induction Generator Based on Synchronised Model for Wind Power Generation," *IET Renewable Power Generation,* vol. 4, pp. 232-241, 2010.

[42] G. S. Buja and M. P. Kazmierkowski, "Direct Torque Control of PWM Inverter-Fed AC Motors - A Survey," *IEEE Transactions on Industrial Electronics,* vol. 51, pp. 744-757, 2004.

[43] A. Tapia, G. Tapia, J. X. Ostolaza, and J. R. Saenz, "Modeling and Control of a Wind Turbine Driven Doubly Fed Induction Generator," *IEEE Transactions on Energy Conversion,* vol. 18, pp. 194-204, 2003.

[44] P. Ledesma and J. Usaola, "Effect of Neglecting Stator Transients in Doubly Fed Induction Generators Models," *IEEE Transactions on Energy Conversion,* vol. 19, pp. 459-461, 2004.

[45] H. Huang, Y. Fan, R.-C. Qiu, and X.-D. Jiang, "Quasi-Steady-State Rotor EMF-Oriented Vector Control of Doubly Fed Winding Induction Generators for Wind-Energy Generation," *Electric Power Components and Systems,* vol. 34, pp. 1201-1211, 2006.

[46] Z. X. Miao, L. L. Fan, D. Osborn, and S. Yuvarajan, "Control of DFIG-Based Wind Generation to Improve Interarea Oscillation Damping," *IEEE Transactions on Energy Conversion,* vol. 24, pp. 415-422, 2009.

[47] W. Zhong, L. Guo-Jie, S. Yuanzhang, and B. T. Ooi, "Effect of Erroneous Position Measurements in Vector-Controlled Doubly Fed Induction Generator," *IEEE Transactions on Energy Conversion,* vol. 25, pp. 59-69, 2010.

[48] M. Mohseni, S. M. Islam, and M. A. Masoum, "Enhanced Hysteresis-Based Current Regulators in Vector Control of DFIG Wind Turbines," *IEEE Transactions on Power Electronics,* vol. 26, pp. 223-234, 2011.

[49] S. Li, T. A. Haskew, K. A. Williams, and R. P. Swatloski, "Control of DFIG Wind Turbine with Direct-Current Vector Control Configuration," *IEEE Transactions on Sustainable Energy,* vol. 3, pp. 1-11, 2012.

[50] X. Yuan, J. Chai, and Y. Li, "A Converter-Based Starting Method and Speed Control of Doubly Fed Induction Machine with Centrifugal Loads," *IEEE Transactions on Industry Applications,* vol. 47, pp. 1409-1418, 2011.

[51] L. Y. Xu and W. Cheng, "Torque and Reactive Power Control of a Doubly Fed Induction Machine by Position Sensorless Scheme," *IEEE Transactions on Industry Applications,* vol. 31, pp. 636-642, 1995.

[52] M. Yamamoto and O. Motoyoshi, "Active and Reactive Power Control for Doubly-Fed Wound Rotor Induction Generator," *IEEE Transactions on Power Electronics,* vol. 6, pp. 624-629, 1991.

[53] E. Rezaei, A. Tabesh, and M. Ebrahimi, "Dynamic Model and Control of DFIG Wind Energy Systems Based on Power Transfer Matrix," *IEEE Transactions on Power Delivery,* vol. 27, pp. 1485-1493, 2012.

[54] T. J. E. Miller, *Reactive power control in electric systems*. New York: Wiley, 1982, ISBN 0-47-186933-3.

[55] R. C. Bansal, A. F. Zobaa, and R. K. Saket, "Some Issues Related to Power Generation Using Wind Energy Conversion Systems: An Overview," *International Journal of Emerging Electric Power Systems,* vol. 3, pp. 1-19, 2005.

[56] S. Foster, L. Xu, and B. Fox, "Coordinated Reactive Power Control for Facilitating Fault Ride Through of Doubly Fed Induction Generator- and Fixed Speed Induction Generator-Based Wind Farms," *IET Renewable Power Generation,* vol. 4, pp. 128-138, 2010.

[57] W. Qiao, R. G. Harley, and G. K. Venayagamoorthy, "Coordinated Reactive Power Control of a Large Wind Farm and a STATCOM Using Heuristic Dynamic Programming," *IEEE Transactions on Energy Conversion,* vol. 24, pp. 493-503, 2009.

[58] R. J. Konopinski, P. Vijayan, and V. Ajjarapu, "Extended Reactive Capability of DFIG Wind Parks for Enhanced System Performance," *IEEE Transactions on Power Systems,* vol. 24, pp. 1346-1355, 2009.

[59] B. C. Rabelo, W. Hofmann, J. L. da Silva, R. G. de Oliveira, and S. R. Silva, "Reactive Power Control Design in Doubly Fed Induction Generators for Wind Turbines," *IEEE Transactions on Industrial Electronics,* vol. 56, pp. 4154-4162, 2009.

[60] S. Engelhardt, I. Erlich, C. Feltes, J. Kretschmann, and F. Shewarega, "Reactive Power Capability of Wind Turbines Based on Doubly Fed Induction Generators," *IEEE Transactions on Energy Conversion,* vol. 26, pp. 364-372, 2011.

[61] R. Aghatehrani and R. Kavasseri, "Reactive Power Management of a DFIG Wind System in Microgrids Based on Voltage Sensitivity Analysis," *IEEE Transactions on Sustainable Energy,* vol. 2, pp. 451-458, 2011.

[62] S. Arnalte, J. C. Burgos, and J. L. Rodríguez-Amenedo, "Direct Torque Control of a Doubly-Fed Induction Generator for Variable Speed Wind Turbines," *Electric Power Components and Systems,* vol. 30, pp. 199-216, 2002.

[63] K. C. Wong, S. L. Ho, and K. W. E. Cheng, "Direct Control Algorithm for Doubly Fed Induction Generators in Weak Grids," *IET Electric Power Applications,* vol. 3, pp. 371-380, 2009.

[64] S. Z. Chen, N. C. Cheung, K. C. Wong, and J. Wu, "Integral Variable Structure Direct Torque Control of Doubly Fed Induction Generator," *IET Renewable Power Generation,* vol. 5, pp. 18-25, 2011.

[65] J. Arbi, M. J. B. Ghorbal, I. Slama-Belkhodja, and L. Charaabi, "Direct Virtual Torque Control for Doubly Fed Induction Generator Grid Connection," *IEEE Transactions on Industrial Electronics,* vol. 56, pp. 4163-4173, 2009.

[66] G. Abad, M. A. Rodriguez, J. Poza, and J. M. Canales, "Direct Torque Control for Doubly Fed Induction Machine-Based Wind Turbines under Voltage Dips and Without Crowbar Protection," *IEEE Transactions on Energy Conversion,* vol. 25, pp. 586-588, 2010.

[67] C. Si Zhe, N. C. Cheung, W. Ka Chung, and W. Jie, "Integral Sliding-Mode Direct Torque Control of Doubly-Fed Induction Generators under Unbalanced Grid Voltage," *IEEE Transactions on Energy Conversion,* vol. 25, pp. 356-368, 2010.

[68] M. Verij Kazemi, A. Sadeghi Yazdankhah, and H. Madadi Kojabadi, "Direct Power Control of DFIG Based on Discrete Space Vector Modulation," *Renewable Energy,* vol. 35, pp. 1033-1042, 2010.

[69] R. Datta and V. T. Ranganathan, "Direct Power Control of Grid-Connected Wound Rotor Induction Machine Without Rotor Position Sensors," *IEEE Transactions on Power Electronics,* vol. 16, pp. 390-399, 2001.

[70] T. Noguchi, H. Tomiki, S. Kondo, and I. Takahashi, "Direct Power Control of PWM Converter Without Power-Source Voltage Sensors," *IEEE Transactions on Industry Applications,* vol. 34, pp. 473-479, 1998.

[71] A. J. Sguarezi Filho and E. R. Filho, "Model-Based Predictive Control Applied to the Doubly-Fed Induction Generator Direct Power Control," *IEEE Transactions on Sustainable Energy,* vol. 3, pp. 398-406, 2012.

[72] Z. Dawei, X. Lie, and B. W. Williams, "Model-Based Predictive Direct Power Control of Doubly Fed Induction Generators," *IEEE Transactions on Power Electronics,* vol. 25, pp. 341-351, 2010.

[73] A. Bouafia, J. P. Gaubert, and F. Krim, "Predictive Direct Power Control of Three-Phase Pulsewidth Modulation (PWM) Rectifier Using Space-Vector Modulation (SVM)," *IEEE Transactions on Power Electronics,* vol. 25, pp. 228-236, 2010.

[74] M. Malinowski, M. P. Kazmierkowski, S. Hansen, F. Blaabjerg, and G. D. Marques, "Virtual-Flux-Based Direct Power Control of Three-Phase PWM Rectifiers," *IEEE Transactions on Industry Applications,* vol. 37, pp. 1019-1027, 2001.

[75] D. Santos-Martin, J. L. Rodriguez-Amenedo, and S. Arnalte, "Direct Power Control Applied to Doubly Fed Induction Generator under Unbalanced Grid Voltage Conditions," *IEEE Transactions on Energy Conversion,* vol. 23, pp. 2328-2336, 2008.

[76] G. Abad, M. A. Rodriguez, G. Iwanski, and J. Poza, "Direct Power Control of Doubly-Fed-Induction-Generator-Based Wind Turbines under Unbalanced Grid Voltage," *IEEE Transactions on Power Electronics,* vol. 25, pp. 442-452, 2010.

[77] P. Zhou, Y. K. He, and D. Sun, "Improved Direct Power Control of a DFIG-Based Wind Turbine During Network Unbalance," *IEEE Transactions on Power Electronics,* vol. 24, pp. 2465-2474, 2009.

[78] H. Nian, Y. Song, P. Zhou, and Y. K. He, "Improved Direct Power Control of a Wind Turbine Driven Doubly Fed Induction Generator During Transient Grid Voltage Unbalance," *IEEE Transactions on Energy Conversion,* vol. 26, pp. 976-986, 2011.

[79] R. Datta and V. T. Ranganathan, "A Simple Position-Sensorless Algorithm for Rotor-Side Field-Oriented Control of Wound-Rotor Induction Machine," *IEEE Transactions on Industrial Electronics,* vol. 48, pp. 786-793, 2001.

[80] R. Cardenas, R. Pena, J. Clare, G. Asher, and J. Proboste, "MRAS Observers for Sensorless Control of Doubly-Fed Induction Generators," *IEEE Transactions on Power Electronics,* vol. 23, pp. 1075-1084, 2008.

[81] R. Pena, R. Cardenas, J. Proboste, G. Asher, and J. Clare, "Sensorless Control of Doubly-Fed Induction Generators Using a Rotor-Current-Based MRAS Observer," *IEEE Transactions on Industrial Electronics,* vol. 55, pp. 330-339, 2008.

[82] D. G. Forchetti, G. O. Garcia, and M. I. Valla, "Adaptive Observer for Sensorless Control of Stand-Alone Doubly Fed Induction Generator," *IEEE Transactions on Industrial Electronics,* vol. 56, pp. 4174-4180, 2009.

[83] M. S. Carmeli, F. Castelli-Dezza, M. Iacchetti, and R. Perini, "Effects of Mismatched Parameters in MRAS Sensorless Doubly Fed Induction Machine Drives," *IEEE Transactions on Power Electronics,* vol. 25, pp. 2842-2851, 2010.

[84] F. C. Dezza, G. Foglia, M. F. Iacchetti, and R. Perini, "An MRAS Observer for Sensorless DFIM Drives with Direct Estimation of the Torque and Flux Rotor Current Components," *IEEE Transactions on Power Electronics,* vol. 27, pp. 2576-2584, 2012.

[85] G. D. Marques, V. F. Pires, S. Sousa, and D. M. Sousa, "A DFIG Sensorless Rotor-Position Detector Based on a Hysteresis Controller," *IEEE Transactions on Energy Conversion,* vol. 26, pp. 9-17, 2011.

[86] G. D. Marques and D. M. Sousa, "New Sensorless Rotor Position Estimator of a DFIG Based on Torque Calculations - Stability Study," *IEEE Transactions on Energy Conversion,* vol. 27, pp. 196-203, 2012.

[87] B. Mwinyiwiwa, Y. Z. Zhang, B. K. Shen, and B. T. Ooi, "Rotor Position Phase-Locked Loop for Decoupled P-Q Control of DFIG for Wind Power Generation," *IEEE Transactions on Energy Conversion,* vol. 24, pp. 758-765, 2009.

[88] B. Shen, B. Mwinyiwiwa, Y. Z. Zhang, and B. T. Ooii, "Sensorless Maximum Power Point Tracking of Wind by DFIG Using Rotor Position Phase Lock Loop (PLL)," *IEEE Transactions on Power Electronics,* vol. 24, pp. 942-951, 2009.

[89] S. Yang and V. Ajjarapu, "A Speed-Adaptive Reduced-Order Observer for Sensorless Vector Control of Doubly Fed Induction Generator-Based Variable-Speed Wind Turbines," *IEEE Transactions on Energy Conversion,* vol. 25, pp. 891-900, 2010.

[90] G. D. Marques and D. M. Sousa, "Air-Gap-Power-Vector-Based Sensorless Method for DFIG Control Without Flux Estimator," *IEEE Transactions on Industrial Electronics,* vol. 58, pp. 4717-4726, 2011.

[91] L. Xu, E. Inoa, Y. Liu, and B. Guan, "A New High-Frequency Injection Method for Sensorless Control of Doubly Fed Induction Machines," *IEEE Transactions on Industry Applications,* vol. 48, pp. 1556-1564, 2012.

[92] A. Karthikeyan, C. Nagamani, and G. S. Ilango, "A Versatile Rotor Position Computation Algorithm for the Power Control of a Grid-Connected Doubly Fed Induction Generator," *IEEE Transactions on Energy Conversion,* vol. 27, pp. 697-706, 2012.

[93] R. E. Betz and M. G. Jovanovic, "The Brushless Doubly Fed Reluctance Machine and the Synchronous Reluctance Machine-a Comparison," *IEEE Transactions on Industry Applications,* vol. 36, pp. 1103-1110, 2000.

[94] L. Xu and Y. Tang, "A Novel Wind-Power Generating System Using Field Orientation Controlled Doubly-Excited Brushless Reluctance Machine," in *Conference Record of the 1992 IEEE Industry Applications Society Annual Meeting*, 1992, pp. 408-413 vol.1.

[95] M. G. Jovanovic, R. E. Betz, and J. Yu, "The Use of Doubly Fed Reluctance Machines for Large Pumps and Wind Turbines," *IEEE Transactions on Industry Applications,* vol. 38, pp. 1508-1516, 2002.

[96] D. G. Dorrell and M. Jovanovic, "On the Possibilities of Using a Brushless Doubly-Fed Reluctance Generator in a 2 MW Wind Turbine," in *IAS '08. IEEE Industry Applications Society Annual Meeting*, 2008, pp. 1-8.

[97] M. G. Jovanovic and R. E. Betz, "Slip Power Recovery Systems Based on Brushless Doubly Fed Reluctance Machines," in *PCC Osaka 2002. Proceedings of the Power Conversion Conference*, 2002, pp. 987-992 vol.3.

[98] R. E. Betz and M. G. Jovanovic, "Introduction to the Space Vector Modeling of the Brushless Doubly Fed Reluctance Machine," *Electric Power Components and Systems,* vol. 31, pp. 729-755, 2003.

[99] R. E. Betz and M. G. Jovanovic, "Theoretical Analysis of Control Properties for the Brushless Doubly Fed Reluctance Machine," *IEEE Transactions on Energy Conversion,* vol. 17, pp. 332-339, 2002.

[100] Y. Liao, L. Xu, and L. Zhen, "Design of a Doubly Fed Reluctance Motor for Adjustable-Speed Drives," *IEEE Transactions on Industry Applications,* vol. 32, pp. 1195-1203, 1996.

[101] R. E. Betz and M. G. Jovanovic, "The Brushless Doubly Fed Reluctance Machine and The Synchronous Reluctance Machine-A Comparison," in *Thirty-Fourth IAS Annual Meeting. Conference Record of the 1999 IEEE Industry Applications Conference*, 1999, pp. 854-861 vol.2.

[102] M. Jovanovic and R. E. Betz, "Optimal Performance of Brushless Doubly Fed Reluctance Machines," in *Ninth International Conference on (Conf. Publ. No. 468) Electrical Machines and Drives*, 1999, pp. 386-390.

[103] O. Ojo and Z. Wu, "Synchronous Operation of a Dual-Winding Reluctance Generator," *IEEE Transactions on Energy Conversion,* vol. 12, pp. 357-362, 1997.

[104] F. Saifkhani and A. K. Wallace, "A Linear Brushless Doubly-Fed Machine Drive for Traction Applications," in *Fifth European Conference on Power Electronics and Applications*, 1993, pp. 344-348 vol.5.

[105] M. G. Jovanovic, "Power Factor and Inverter Rating - A Compromise in Doubly Fed Reluctance Machine Drives," in *Eighth International Conference on (IEE Conf. Publ. No. 475) Power Electronics and Variable Speed Drives*, 2000, pp. 311-316.

[106] M. G. Jovanovic and R. E. Betz, "Power Factor Control Using Brushless Doubly Fed Reluctance Machines," in *Conference Record of the 2000 IEEE Industry Applications Conference*, 2000, pp. 523-530 vol.1.

[107] M. G. Jovanovic and M. M. R. Ahmed, "Sensorless Speed Control Strategy for Brushless Doubly-Fed Reluctance Machines," in *IEMDC '07. IEEE International Electric Machines & Drives Conference*, 2007, pp. 1514-1519.

[108] M. G. Jovanovic and D. G. Dorrell, "Sensorless Control of Brushless Doubly-Fed Reluctance Machines Using an Angular Velocity Observer," in *PEDS '07. 7th International Conference on Power Electronics and Drive Systems*, 2007, pp. 717-724.

[109] F. Wang, F. Zhang, and L. Xu, "Parameter and Performance Comparison of Doubly Fed Brushless Machine with Cage and Reluctance Rotors," *IEEE Transactions on Industry Applications,* vol. 38, pp. 1237-1243, 2002.

[110] E. M. Schulz and R. E. Betz, "Optimal Torque Per Amp for Brushless Doubly Fed Reluctance Machines," in *Fourtieth IAS Annual Meeting. Conference Record of the 2005 Industry Applications Conference*, 2005, pp. 1749-1753 Vol. 3.

[111] M. G. Jovanovic, R. E. Betz, Y. Jian, and E. Levi, "Aspects of Vector and Scalar Control of Brushless Doubly Fed Reluctance Machines," in *4th IEEE International Conference on Power Electronics and Drive Systems, 2001*, 2001, pp. 461-467 vol.2.

[112] M. G. Jovanovic, J. Yu, and E. Levi, "Direct Torque Control of Brushless Doubly Fed Reluctance Machines," *Electric Power Components and Systems,* vol. 32, pp. 941-958, 2004.

[113] M. Jovanovic, "Control of Brushless Doubly-Fed Reluctance Motors," in *ISIE 2005. Proceedings of the IEEE International Symposium on Industrial Electronics*, 2005, pp. 1667-1672.

[114] M. G. Jovanovic, J. Yu, and E. Levi, "Encoderless Direct Torque Controller for Limited Speed Range Applications of Brushless Doubly Fed Reluctance Motors," *IEEE Transactions on Industry Applications,* vol. 42, pp. 712-722, 2006.

[115] M. Hassan and M. Jovanovic, "Improved Scalar Control Using Flexible DC-Link Voltage in Brushless Doubly-Fed Reluctance Machines for Wind Applications," in *2nd International Symposium on Environment Friendly Energies and Applications (EFEA)*, 2012, pp. 482-487.

[116] L. Y. Xu, L. Zhen, and E.-H. Kim, "Field-Orientation Control of a Doubly Excited Brushless Reluctance Machine," *IEEE Transactions on Industry Applications,* vol. 34, pp. 148-155, 1998.

[117] Y. Liao and C. Sun, "A Novel Position Sensorless Control Scheme for Doubly Fed Reluctance Motor Drives," *IEEE Transactions on Industry Applications,* vol. 30, pp. 1210-1218, 1994.

[118] M. G. Jovanovic, J. Yu, and E. Levi, "A Doubly-Fed Reluctance Motor Drive with Sensorless Direct Torque Control," in *IEMDC'03. IEEE International Electric Machines and Drives Conference*, 2003, pp. 1518-1524 vol.3.

[119] H. Chaal and M. Jovanovic, "Flux Observer Algorithms for Direct Torque Control of Brushless Doubly-Fed Reluctance Machines," in *IECON '09. 35th Annual Conference of IEEE Industrial Electronics*, 2009, pp. 4440-4445.

[120] H. Chaal, M. Jovanovic, and K. Busawon, "Sliding Mode Observer Based Direct Torque Control of a Brushless Doubly-Fed Reluctance Machine," in *ISIEA 2009. IEEE Symposium on Industrial Electronics & Applications*, 2009, pp. 866-871.

[121] H. Chaal and M. Jovanovic, "Direct Power Control of Brushless Doubly-Fed Reluctance Machines," in *5th IET International Conference on Power Electronics, Machines and Drives (PEMD 2010)*, 2010, pp. 1-6.

[122] H. Chaal and M. Jovanovic, "A New Sensorless Torque and Reactive Power Controller for Doubly-Fed Machines," in *International Conference on Electrical Machines (ICEM)*, 2010, pp. 1-6.

[123] H. Chaal and M. Jovanovic, "Power Control of Brushless Doubly-Fed Reluctance Drive and Generator Systems," *Renewable Energy,* vol. 37, pp. 419-425, 2012.

[124] H. Chaal and M. Jovanovic, "Practical Implementation of Sensorless Torque and Reactive Power Control of Doubly Fed Machines," *IEEE Transactions on Industrial Electronics,* vol. 59, pp. 2645-2653, 2012.

[125] H. Chaal and M. Jovanovic, "Toward a Generic Torque and Reactive Power Controller for Doubly Fed Machines," *IEEE Transactions on Power Electronics,* vol. 27, pp. 113-121, 2012.

[126] G. Abad, E. Institute of, and E. Electronics, *Doubly Fed Induction Machine : Modeling and Control for Wind Energy Generation*. New Jersey: John Wiley & Sons, Inc., 2011, ISBN 0-47-076865-7.

[127] N. Mohan, T. M. Undeland, and W. P. Robbins, *Power Electronics : Converters, Applications, and Design*, 3rd ed., New Jersey: John Wiley & Sons, Inc., 2003, ISBN 0-47-122693-9.

[128] "IEEE Standard Test Procedure for Polyphase Induction Motors and Generators," in *IEEE Std 112-2004 (Revision of IEEE Std 112-1996)*, ed, 2004, pp. 1-79.

[129] M. Bohllnder, "MIPAQserve Application Note - Technical Report AN2009-07," Infineon Technologies AG, Warstein, Germany, 2010.

[130] "TMS320F28335 Digital Signal Controller Data Manual - Technical Report SPRS439I," Texas Instruments2011.

[131] "eZdsp F28335 Technical Reference - Technical Report 510195-0001 Rev. C," Spectrum Digital Inc., 2007.

[132] D. Atkinson, "General Purpose Power Interface Board - Design Report," School of Electrical, Electronic and Computing Engineering, Newcastle University, Newcastle upon Tyne, UK, 2010.

[133] F. Wang, "Design and Experimental Test of a New BDFRG - Technical Report," Electrical Control Technology Institute, Shenyang University of Technology, Shenyang, China, 2010.

Appendix A. DFIM Test Rig

The DFIM test rig has been designed to be as flexible as possible to allow control prototyping in both motoring and generating modes of the machine for emulation of various industrial applications in a laboratory environment. Many hardware components have been deliberately overrated (e.g. power electronics converters) for safety reasons. It also has multiple current and voltage transducers, as well as an incremental shaft position encoder fitted, for control purposes together with other measuring equipment for performance monitoring (e.g. a torque transducer, voltage/current probes, digital oscilloscopes etc.). The custom build hardware has been assembled in a control panel shown in Fig. A.1.

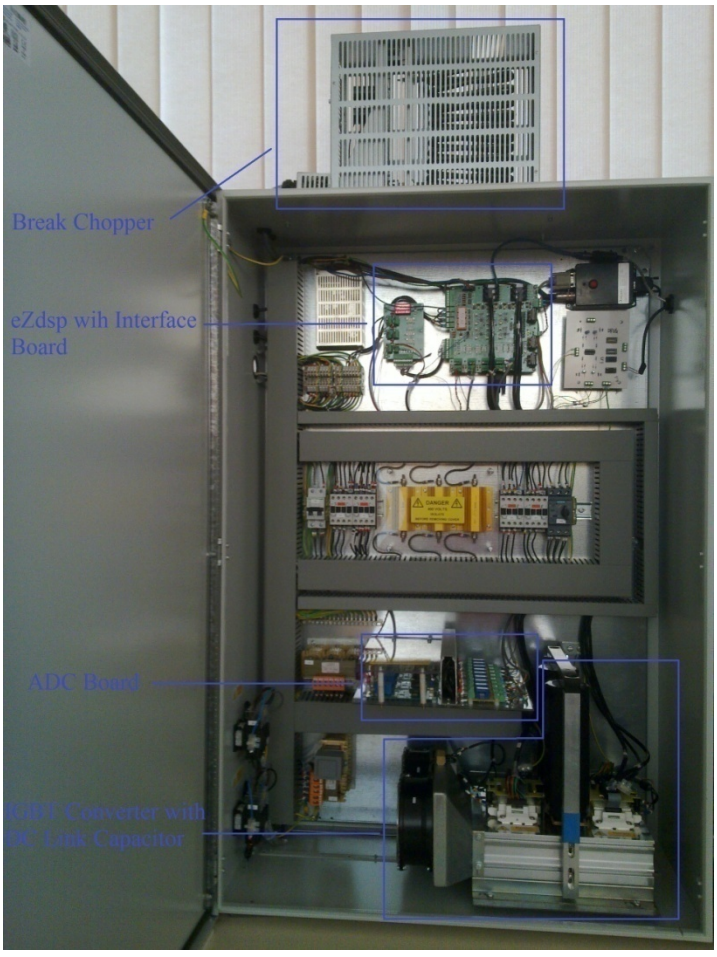

Figure A.1: Assembled DFIM Control Panel

A.1 Off-line Testing of the DFIM

In order to identify the winding parameters of the DFIM, a set of off-line testing procedures has been carried out as described in [128]. The machine ratings can be found on its nameplate, which could be summarized in Table A.1 as,

Table A.1: Ratings of the DFIM

Power Rating	6.75 kW
Rated Rotating Speed (Motor)	710 rpm
Voltage Rating (Stator)	415 V
Current Rating (Stator)	16.3 A
Voltage Rating (Rotor)	175 V
Current Rating (Rotor)	24 A

Stator and rotor resistance have been measured directly from rotor and stator winding terminals when the machine is standstill. And a series of tests such as open circuit test, no-load test and locked-rotor test have been carried out to achieve turns ratio between the stator and the rotor, leakage inductance on both the stator and the rotor, and magnetising inductance. A set of DFIM parameters has been obtained as,

Table A.2: Parameters of the DFIM

Stator Resistance	0.423 Ω
Rotor Resistance	0.198 Ω
Stator Leakage Inductance	2.149 mH
Rotor Leakage Inductance	2.149 mH
Magnetising Inductance	75.751 mH
Turns Ratio	2.14
Estimated Inertia	0.25 kgm^2

A.2 DFIM Specifications

A refurbished, off-the-shelf, 8-pole, 710 rpm and 6.75 kW slip-ring induction motor (Fig. A.2) from Brook Crompton Parkinson Motors®, has been used for doubly-fed operation mostly as a generator (DFIG) for the scope of this project. The ratings are listed in Table A.1. The remaining machine parameters have been identified by off-line testing as described in Section A.1.

Figure A.2: The DFIG (left) – Prime Mover (right) Set

A.3 Prime Mover

The prime mover is a 6-pole, 415 V, 22.7 A, 11 kW squirrel cage induction motor from Brook Crompton® (Fig. A.2) with a commercial 11 kW, 4-quadrant, drive (ATV71HD11N4) from Schneider Electric®. A photo of the drive panel is shown in Fig. A.3. The drive features an integrated EMC filter and implements sensorless flux vector (V/f) control at 4 kHz switching frequency.

Figure A.3: The Control Panel of the Prime Mover

A.4 Voltage Source Converter

A bi-directional power electronics converter (Fig. A.4) on the rotor side consists of two conventional back-to-back 3-phase IGBT bridges with a capacitor and a brake chopper in the DC link. Each of the two custom-made IGBT converters consists of an intelligent power module with adapted driver electronics and temperature measurement circuitry which belongs to the MIPAQ™ serve family from Infineon® (Fig. A.5). The IFS100V12PT4 MIPAQ™ serve provides a full set of six isolated IGBT drivers. The module could operate at 100 A nominal current at 1200 V blocking voltage. Further details can be found in [129].

Two identical electrolytic capacitors rated at 8200 μF, 450 V from FELSIC CAPAX are connected in series to provide a DC link for the IGBT converters. The equivalent capacitance is 4100 μF with a maximum voltage of 900 V.

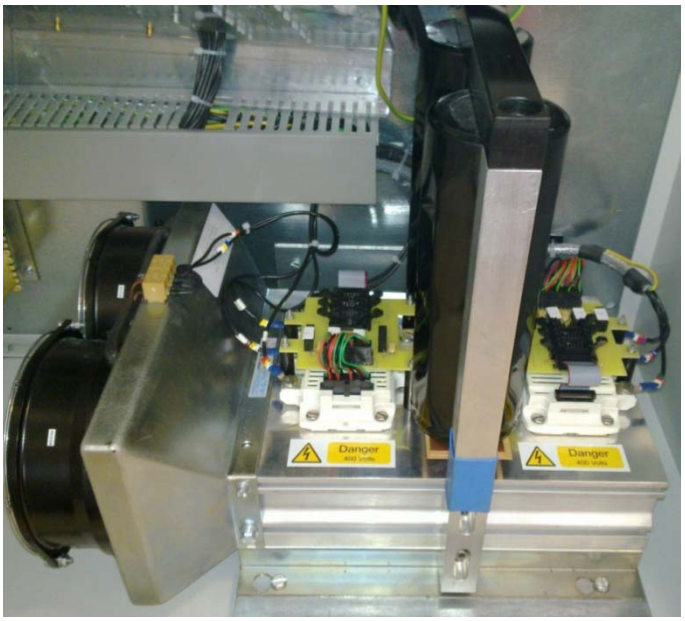

Figure A.4: Custom Built AC/DC/AC Converter

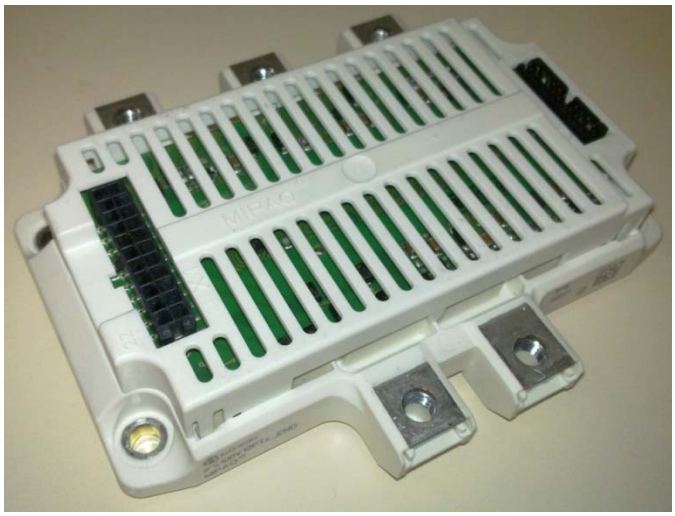

Figure A.5: IFS100V12PT4 MIPAQ™ Serve Power Module

Although one of the main roles of the active rectifier on the grid side is to ensure voltage control in the DC link for bi-directional power flow, an extra level of overvoltage protection for the DC link capacitors and IGBTs was provided by an ABB® universal brake unit consisting of a power resistor (32 Ω, 2 kW) and control electronics. The ACS-BRK-C (Fig. A.6) is rated at 12 kW with a maximum pre-set threshold value of 700 V to limit the DC link voltage.

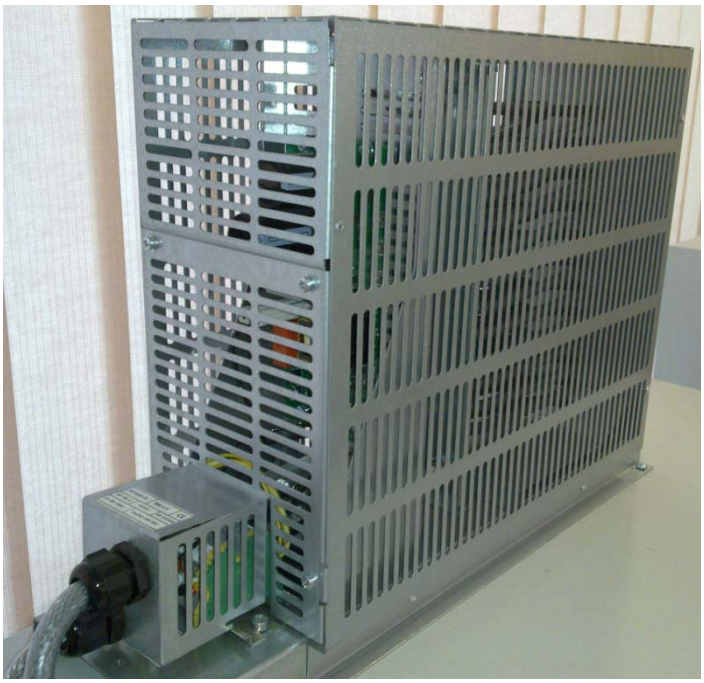

Figure A.6: ABB ACS-BRK-C Brake Chopper

A.5 Control Hardware

A.5.1 Digital Signal Controller

An eZdsp™ F28335, 32-bit floating-point digital signal controller (DSC) from Texas Instruments® (TI) has been chosen to be the heart of the control system. This module has a powerful TMS320F28335 processor of TI C2000 family offering excellent performance in various industrial applications and especially for machine drive control. The eZdsp™ can be debugged by assembly and C languages through its own software Code Composer Studio™. The F28335 processor operates at 150 MHz and has enhanced control peripherals such as 18 PWM outputs, two quadrature encoder interface, three 32-bit CPU timers, and a 12-bit AD converter with 16 input channels. The eZdsp™ includes the following on-chip memory: 256K * 16 Flash, 8 blocks of 4K * 16 single access RAM (SARAM), 2 blocks of 8K * 16 SARAM, and 2 blocks of 1K * 16 SARAM. In addition, 128K * 16 off-chip SRAM is provided. Further details can be found in [130,131].

A.5.2 Interface Board

General purpose of designing a power interface board for converter control has been described in [132]. The board (Fig. A.7) has been designed by Newcastle University (through research collaboration on a related EPSRC project) to provide an interface between eZdsp^{TM} and the power converter hardware. A functional block diagram of the board is shown in Fig. A.8 and a photo of its front view in Fig. A.9 with a photo of the expansion analogue interface board being presented in Fig. A.10. The interface has been designed to fit a range of different external transducers and gate drivers. Thus, the current and voltage transducers can be wired directly to the sensor interface connectors without the need for any additional circuitry. But, in some interface sections on the board, links are included for the optional microcontroller signal use. Four small relays on the board can be used to energize the contactors coils. For EMI and common ground problems, the interface board has one of the internal layers dedicated to be a common ground plane and the shape of which being designed to prevent interference on sensitive analogue signals due to a digital signal return path.

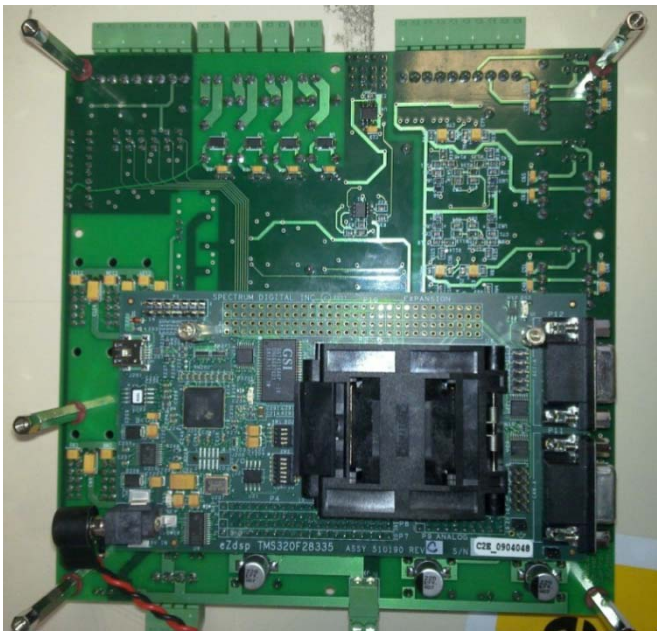

Figure A.7: Back View of the Interface Board with eZdsp^{TM} Mounted

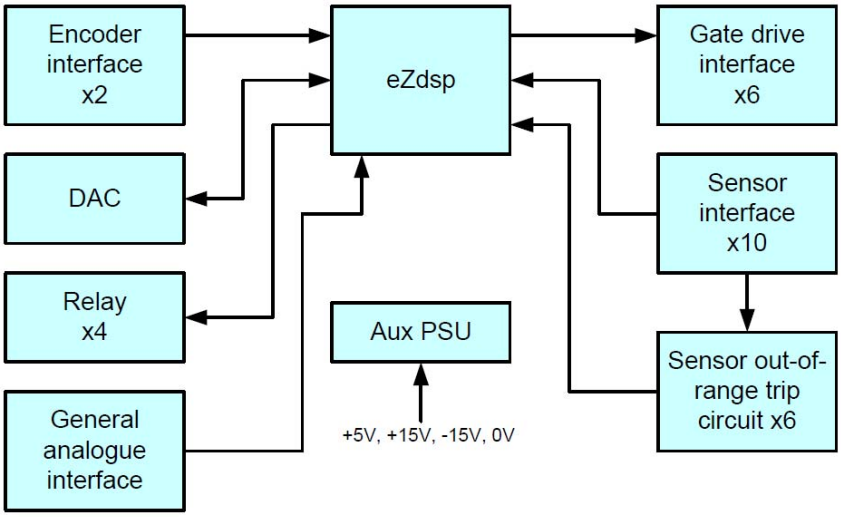

Figure A.8: Schematic Diagram of the Interface Board [143]

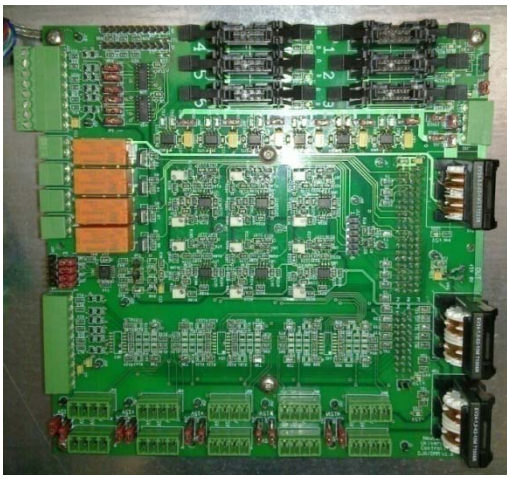

Figure A.9: Front View of the Interface Board

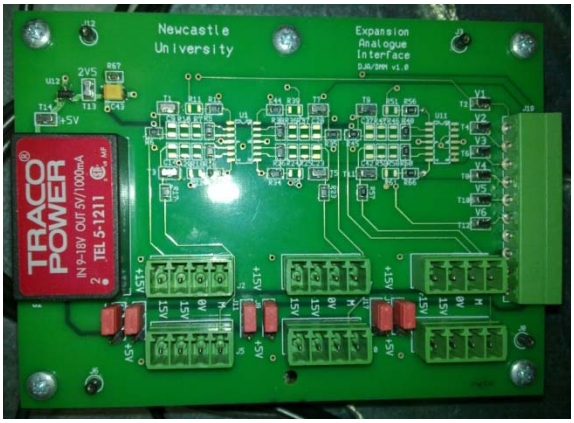

Figure A.10: Expansion Analogue Interface Board

A.6 Other Hardware

A.6.1 Filters

A 0.346 mH, 17 A choke of L type from Schaffner® (RWK305-17-KL) has been placed in series between the power converter and the machine rotor winding (Fig. A.11). The converter switching frequency should be in the range of 2 - 16 kHz. A 3-phase, 13 mH, 2.2 μF, 4.5 A line reactor filter from Schaffner® (FN5040-4.5-82) of LC type has been chosen to help reducing a higher harmonic content in the line side current induced by the converter switching (Fig. A.12).

Figure A.11: Generator Side Choke

Figure A.12: Line Reactor (LC Filter)

A.6.2 Current and Voltage Transducers

A number of transducers have been fitted in the main control cabinet for measurement and condition monitoring (Fig. A.13). 9 transducers (3/phase) have been used for measuring line side currents, stator currents and rotor currents. The current transducers (LEM CAS 15-NP) have been modified to allow measurement of up to ±50 A. 3 transducers (LEM LV 25-200) have been employed to measure 3-phase stator voltages, and the 4th transducer (LEM LV 25-600) to measure the DC link voltage.

Figure A.13: Current and Voltage Transducers

A.6.3 Isolation Amplifier PCB

A control channel between the cage induction motor drive (prime mover) and the interface board has been created to directly control the shaft speed from the Labview™ interface on a PC. In order to amplify the output signal from the DAC port on the interface board (0 – 2 V) to suit the analogue signal input range (0 – 12V), two isolation amplifiers have been mounted inside the main control panel (Fig. A.14); one has been used for the prime mover speed control and the other one is a back-up or can be used for torque control in the future. A 4-channel amplifier (LF 347) and an isolation amplifier (ISO 122) have individual amplification coefficients of 6 and 1 i.e. 6 in total.

A.7 Overview of the DFIM Test Rig

The entire DFIM test rig has been built based on the schematic diagram presented in Fig. A.16 with the outcome in Fig. A.15.

Figure A.14: Isolation Amplifier PCB

Figure A.15: DFIM Test Rig

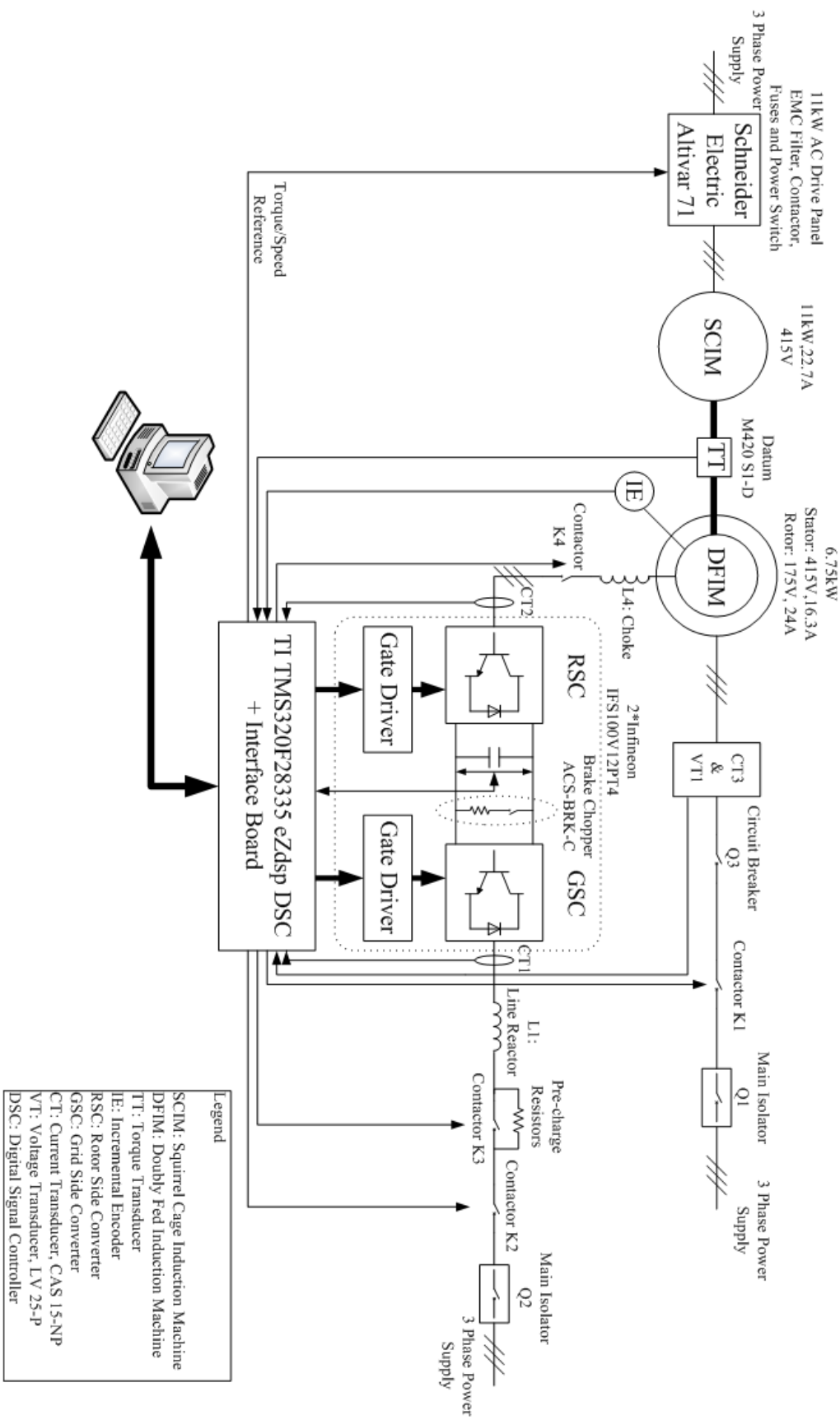

Figure A.16: Schematic Diagram of the DFIM Test Rig

Appendix B. BDFRM Test Rig

The BDFRM test rig is a replica design of the DFIM counterpart to allow a fair comparison of the machines/controller performance. The custom build hardware has been assembled in a control panel identical to DFIM's (Fig. A.1) and appears in Fig. B.1.

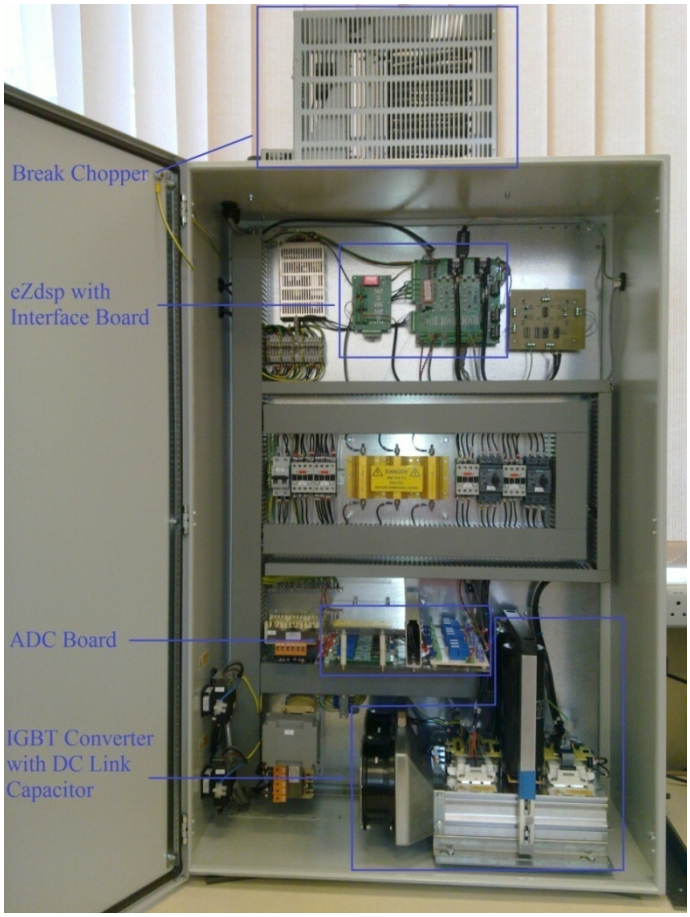

Figure B.1: Assembled BDFRM Control Panel

B.1 Off-line Testing of the BDFRM

In order to find the winding parameters of the BDFRM, a set of testing procedures has been carried out as described in [109]. The machine nameplate with the two stator winding ratings is shown in Fig. B.2.

Figure B.2: BDFRM Nameplate

Primary and secondary resistance have been measured directly from primary and secondary winding terminals when the machine is standstill. Primary, secondary and mutual inductance have been calculated out by applying the methods in [109] with the expressions shown as follow,

$$L_p = \frac{\sqrt{\left(\frac{V_p}{I_p}\right)^2 - R_p^2}}{\omega_p} \tag{B.1}$$

$$L_{ps} = \frac{V_{s0}}{I_p * \omega_p} \tag{B.2}$$

$$L_s = \frac{\sqrt{\left(\frac{V_s}{I_s}\right)^2 - R_s^2}}{\omega_s} \tag{B.3}$$

$$L_{sp} = \frac{V_{p0}}{I_s * \omega_s} \tag{B.4}$$

where V_{s0} and V_{p0} are the measured open-circuit phase voltage of the secondary and primary winding respectively. A set of BDFRM parameters has been obtained as,

Table B.1: Parameters of the BDFRM

Primary Resistance	1.011 Ω
Secondary Resistance	0.547 Ω
Primary Inductance	149.96 mH
Secondary Inductance	286.70 mH
Primary to Secondary Mutual Inductance	121.37 mH
Secondary to Primary Mutual Inductance	158.03 mH
Estimated Inertia	0.1 kgm^2

B.2 BDFRM Test Facility

A BDFRM prototype (Fig. B.3) has been custom designed and built by Shenyang University of Technology, a partner on the collaborative EPSRC project. The machine has conventional 6/2 pole power (primary)/control (secondary) windings rated at 7.5 A and 11.5 A respectively, and a 4 pole radially-laminated reluctance rotor [133]. Thus, the synchronous speed at 50 Hz is the same as of the 8-pole DFIM (750 rpm), and a speed range considered is 2:1 (500 – 1000 rpm) which is typical for wind turbines and similar applications with limited variable speed requirements.

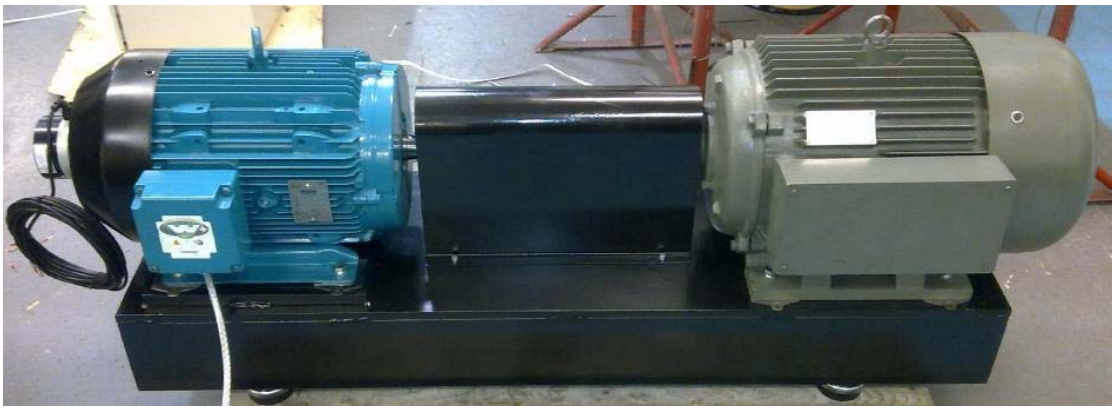

Figure B.3: The Prime Mover (left) – Generator (right) Set

B.3 Complementary Hardware to DFIM Test Rig

The BDFRM test rig is largely identical to the DFIM equivalent for comparison purposes. Thus, most of the structural components and instrumentation/control circuitries are the same including the prime mover and its drive, power electronic converter, control processing hardware, voltage transducers, isolation amplifier PCBs, etc. But still, some of the BDFRM hardware, such as filters and current transducers, are not the same due to differences in machine parameters.

B.3.1 Filters

A 0.42 mH, 14 A choke of L type from Schaffner® (RWK305-14-KL) has been inserted between the power converter and the secondary winding (Fig. B.4). The converter switching frequency should be in the range of 2 - 16 kHz. A 3-phase, 3.1 mH, 10 μF, 17 A line reactor from Schaffner® (FN5040-17-83) of LC type has been chosen to filter out the higher order harmonics in the line side current caused by the switching frequency of the converter (Fig. B.5).

Figure B.4: Generator Side Choke

Figure B.5: Line Reactor (LC Filter)

B.3.2 Current Transducers

A set of current and voltage transducers in the main control panel have been used for measurement and/or condition monitoring (Fig. B.6): 9 (3/phase) for measuring line currents, primary currents and secondary currents, and the same 4 voltage transducers as in the DFIM test rig. The 45 A current transducers (LEM HY 15-P), however, are of different rating to DFIM's.

B.4 Overview of the BDFRM Test Rig

The entire BDFRM test rig has been built based on the schematic diagram presented in Fig. B.8 with the outcome in Fig. B.7.

Figure B.6: Current and Voltage Transducers

Figure B.7: BDFRM Test Rig

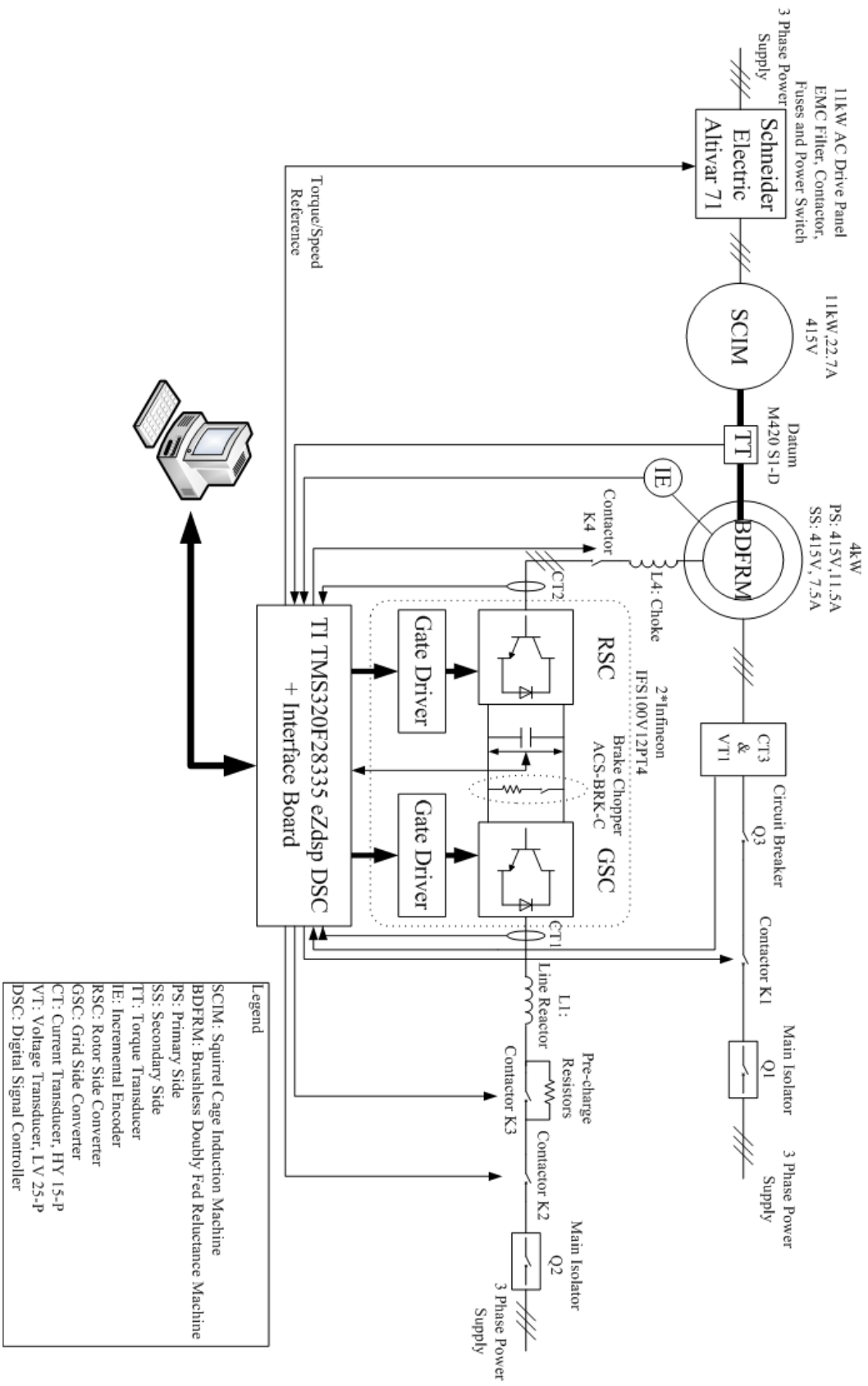

Figure B.8: Schematic Diagram of the BDFRM Test Rig

Appendix C. Coding in CCS

Some of the codes being used in Code Composer Studio (CCS), such as Space Vector Modulation (SVM), sensor calibration, angle conversion and vector control algorithm are listed in the following sections for convenience, and for entity of the presentation of the research work being undertaken.

C.1 SVM

The coding is to obtain a SVM scheme as a subroutine in the entire programming part with the note after double slash.

```
#define INTERCEPT 24681 // Intercept with q-axis of SVM hexagon reference space (95% mod index limit)
#define ROOT3 1.7320508
#define MAX_MOD_INDEX 15000    // Set max mod index (=EPWM_TIMER_TBPRD defined in F28335_drive_functions.c)
#include "DSP2833x_Device.h"     // DSP2833x Headerfile Include File
#include "svm.h"                   // header file
void svm(float vds, float vqs, Uint16 *mia, Uint16 *mib, Uint16 *mic)
{
    Uint16 flag;                        // SVM sector indicator
    float ua,ub,uc;                         // SVM basis vectors
    float v1,v2;                        // SVM temp d and q reference voltage
    Uint16 ma,mb,mc;
    extern Uint16 T0_count;
// Determine which sextant contains the reference vector - flag contains 3-bit code to indicate sextant
    flag = 0;
    if(vqs >= 0) flag = flag|4;
    if(vqs >= ROOT3*vds) flag = flag|2;
    if(vqs >= -ROOT3*vds) flag = flag|1;
// The reference vector (vds+jvqs) is rotated to occupy a position in sextant 1
// Sextant 1 basis vectors ua, ub and uc are then calculated
// The phase modulation index ma, mb and mc are determined in accordance with the original sextant
    switch(flag)
    {
```

```
case 0: /* sextant 5, rotate reference vector 240 deg clockwise */
     v1 = -0.5*vds - 0.8660254*vqs;
     v2 = 0.8660254*vds - 0.5*vqs;
     if(v2 > (INTERCEPT - ROOT3*v1))
          {
          v1 = INTERCEPT*v1/(v2 + ROOT3*v1);
          v2 = INTERCEPT - ROOT3*v1;
          }
     ua = v1 - 0.5773502*v2;
     ub = 1.1547005*v2;
     uc = MAX_MOD_INDEX - ua - ub;
     ma = (int)(ub + 0.5*uc);
     mb = (int)(0.5*uc);
     mc = (int)(ua + ub + 0.5*uc);
     break;
case 1: /* sextant 6, do not rotate reference vector */
    v1 = vds;
     v2 = -vqs;
     if(v2 > (INTERCEPT - ROOT3*v1))
          {
          v1 = INTERCEPT*v1/(v2 + ROOT3*v1);
          v2 = INTERCEPT - ROOT3*v1;
          }
     ua = v1 - 0.5773502*v2;
     ub = 1.1547005*v2;
     uc = MAX_MOD_INDEX - ua - ub;
     ma = (int)(ua + ub + 0.5*uc);
     mb = (int)(0.5*uc);
     mc = (int)(ub + 0.5*uc);
     break;
case 2: /* sextant 4, rotate reference vector 240 deg clockwise and flip horizontal */
     v1 =  -0.5*vds - 0.8660254*vqs;
     v2 =  -0.8660254*vds + 0.5*vqs;
     if(v2 > (INTERCEPT - ROOT3*v1))
          {
          v1 = INTERCEPT*v1/(v2 + ROOT3*v1);
          v2 = INTERCEPT - ROOT3*v1;
          }
     ua = v1 - 0.5773502*v2;
     ub = 1.1547005*v2;
     uc = MAX_MOD_INDEX - ua - ub;
     ma = (int)(0.5*uc);
     mb = (int)(ub + 0.5*uc);
     mc = (int)(ua + ub + 0.5*uc);
```

```
        break;
    case 3:  break;
    case 4:  break;
    case 5: /* sextant 1 do not rotate reference vector */
        v1 = vds;
        v2 = vqs;
        if(v2 > (INTERCEPT - ROOT3*v1))
            {
            v1 = INTERCEPT*v1/(v2 + ROOT3*v1);
            v2 = INTERCEPT - ROOT3*v1;
            }
        ua = v1 - 0.5773502*v2;
        ub = 1.1547005*v2;
        uc = MAX_MOD_INDEX - ua - ub;
        ma = (int)(ua + ub + 0.5*uc);
        mb = (int)(ub + 0.5*uc);
        mc = (int)(0.5*uc);
        break;
    case 6: /* sextant 3, rotate reference vector 120 deg clockwise */
        v1 = -0.5*vds + 0.8660254*vqs;
        v2 = -0.8660254*vds - 0.5*vqs;
        if(v2 > (INTERCEPT - ROOT3*v1))
            {
            v1 = INTERCEPT*v1/(v2 + ROOT3*v1);
            v2 = INTERCEPT - ROOT3*v1;
            }
        ua = v1 - 0.5773502*v2;
        ub = 1.1547005*v2;
        uc = MAX_MOD_INDEX - ua - ub;
        ma = (int)(0.5*uc);
        mb = (int)(ua + ub + 0.5*uc);
        mc = (int)(ub + 0.5*uc);
        break;
    case 7: /* sextant 2, rotate reference vector 120 deg clockwise and flip horizontal */
        v1 = -0.5*vds + 0.8660254*vqs;
        v2 = 0.8660254*vds + 0.5*vqs;
        if(v2 > (INTERCEPT - ROOT3*v1))
            {
            v1 = INTERCEPT*v1/(v2 + ROOT3*v1);
            v2 = INTERCEPT - ROOT3*v1;
            }
        ua = v1 - 0.5773502*v2;
        ub = 1.1547005*v2;
        uc = MAX_MOD_INDEX - ua - ub;
```

```
            ma = (int)(ub + 0.5*uc);
            mb = (int)(ua + ub + 0.5*uc);
            mc = (int)(0.5*uc);
            break;
        default: break;
           }
// invert mod index - this is because the PWM hardware works upside down
    *mia = MAX_MOD_INDEX - ma;
    *mib = MAX_MOD_INDEX - mb;
    *mic = MAX_MOD_INDEX - mc;
}
```

C.2 Sensor Calibration

All the ADCs used in the experiments should be pre-calibrated. Since 9 current and 4 voltage transducers are employed on each test rig, the total of 13 ADCs of 16 ADCs available on each TMS320F28335 chip are calibrated as follows for both the DFIM and the BDFRM test rigs.

C.2.1 DFIM Test Rig

```
    vsa = (float)0.18634*((int)(AdcRegs.ADCRESULT10 >>4)-2280);
    vsb = (float)0.18735*((int)(AdcRegs.ADCRESULT11 >>4)-2285);
    vsc = (float)0.18465*((int)(AdcRegs.ADCRESULT12 >>4)-2277);
    vdc = (float)0.55906*((int)(AdcRegs.ADCRESULT13 >>4)-2288);
    isa = (float)0.02975*((int)(AdcRegs.ADCRESULT6 >>4)-2016);
    isb = (float)0.02969*((int)(AdcRegs.ADCRESULT7 >>4)-2020);
    isc = (float)0.02959*((int)(AdcRegs.ADCRESULT8 >>4)-2017);
    ira = (float)0.02964*((int)(AdcRegs.ADCRESULT3 >>4)-2017);
    irb = (float)0.02981*((int)(AdcRegs.ADCRESULT4 >>4)-2013);
    irc = (float)0.02964*((int)(AdcRegs.ADCRESULT5 >>4)-2020);
    ila = (float)0.02968*((int)(AdcRegs.ADCRESULT0 >>4)-2032);
    ilb = (float)0.02968*((int)(AdcRegs.ADCRESULT1 >>4)-2037);
    ilc = (float)0.02977*((int)(AdcRegs.ADCRESULT2 >>4)-2017);
```

C.2.2 BDFRM Test Rig

```
vsa = (float)0.187914508*((int)(AdcRegs.ADCRESULT11 >>4)-2260);
vsb = (float)0.186050153*((int)(AdcRegs.ADCRESULT12 >>4)-2254);
vsc = (float)0.18401629*((int)(AdcRegs.ADCRESULT13 >>4)-2259);
vdc = (float)0.561932007*((int)(AdcRegs.ADCRESULT10 >>4)-2255);
isa = (float)0.020417468*((int)(AdcRegs.ADCRESULT6 >>4)-2260);
isb = (float)0.020207703*((int)(AdcRegs.ADCRESULT7 >>4)-2268);
isc = (float)0.020513231*((int)(AdcRegs.ADCRESULT8 >>4)-2267);
ira = (float)0.020311068*((int)(AdcRegs.ADCRESULT3 >>4)-2256);
irb = (float)0.019986812*((int)(AdcRegs.ADCRESULT4 >>4)-2259);
irc = (float)0.019787656*((int)(AdcRegs.ADCRESULT5 >>4)-2254);
ila = (float)0.019922254*((int)(AdcRegs.ADCRESULT0 >>4)-2268);
ilb = (float)0.019907289*((int)(AdcRegs.ADCRESULT1 >>4)-2275);
ilc = (float)0.020570538*((int)(AdcRegs.ADCRESULT2 >>4)-2261);
```

C.3 Angle Conversions

The control of the DFIM and the BDFRM is executed in a rotating reference frame and as such requires angle conversions of stationary frame vectors as demonstrated in the previous chapters. ‘theta_e’ inside the code represents the angle of the stator/primary voltage oriented frame, ‘theta_m’ indicates the rotor frame angle, and ‘theta_t’ stands for the slip angle. ‘pos_count’ is the value recorded from the 5000 lines incremental encoder and 720 is equivalent to 2*pi within the entire coding.

```
if((pos_count >= 0) & (pos_count < 5000))
     theta_m = (int)(720-0.144*pos_count);            //720/5000=0.144,
    else if((pos_count >=5000) & (pos_count < 10000))
            theta_m = (int)(720-0.144*(pos_count - 5000));
    else if((pos_count >=10000) & (pos_count < 15000))
            theta_m = (int)(720-0.144*(pos_count - 10000));
else
     theta_m = (int)(720-0.144*(pos_count - 15000));
     theta_t = (int)(theta_e-theta_m);
     if(theta_t >= 720)
            theta_t = theta_t-720;
     if(theta_t < 0)
            theta_t = theta_t+720;
```

C.4 Example of Vector Control (VC) Algorithm

PI based controllers of either the DFIM or BDFRM need reasonably optimal tuning of proportional and integral gains (kp and ki) to control the MSC and GSC successfully under various operating conditions. The coding listed is an example of the VC algorithm for the rotor d-q current components on the DFIM test rig. The 'ird_demand' and 'irq_demand' in the code are reference values of the d-q components of the rotor side current respectively which are adjustable in Labview, while the 'irde' and 'irqe' are the d-q components of the same current but after applying Park's Transformation. 'CURRENT_LOOP_INT_CLAMP' is the limiter to avoid the rotor current saturation.

```
    ird_demand = par3;
    irq_demand = par6;
    ird_error = (ird_demand - irde);
    irq_error = (irq_demand - irqe);
    kp = kp1;
    ki = ki1;
// d-axis PI
    vde1 = kp1*ird_error + zd1;
    if(release)
        zd1 = zd1 + ki1*ird_error;
// d-axis integrator clamp (+/- 95% mod index range)
    if(zd1 > CURRENT_LOOP_INT_CLAMP)
        zd1 = CURRENT_LOOP_INT_CLAMP;
    if(zd1 < -CURRENT_LOOP_INT_CLAMP)
        zd1 = -CURRENT_LOOP_INT_CLAMP;
// q-axis PI
    vqe1 = kp1*irq_error + zq1;
    if(release)
        zq1 = zq1 + ki1*irq_error;
// q-axis integrator clamp (+/- 95% mod index range)
    if(zq1 > CURRENT_LOOP_INT_CLAMP)
        zq1 = CURRENT_LOOP_INT_CLAMP;
    if(zq1 < -CURRENT_LOOP_INT_CLAMP)
        zq1 = -CURRENT_LOOP_INT_CLAMP;
```